NORTHWESTERN UNIVERSITY

Modulating the Nanomechanical Properties of Graphene Oxide via Chemical Structure and Interfacial Interactions

A DISSERTATION

SUBMITTED TO THE GRADUATE SCHOOL IN PARTIAL FULFILLMENT OF THE REQUIREMENTS

for the degree

DOCTOR OF PHILOSOPHY

Field of Chemistry

By

Lily Mao

EVANSTON ILLINOIS

August 2022

ABSTRACT

Modulating the Nanomechanical Properties of Graphene Oxide via Chemical Structure and Interfacial Interactions

Lily Mao

Carbon nanomaterials, such as graphene and graphene oxide, have outstanding mechanical strength, stiffness, and toughness that surpass those of materials currently used to build structures. However, these properties are limited to the nanoscale and have not yet been attained in macroscopic composites containing carbon nanomaterials. To integrate the mechanical properties of nanocarbons into their macroscopic composites, it is important to understand how the mechanical properties of the composite at each length scale are influenced by the structure and surface chemistry of the nanocarbon filler and its interfacial interactions with the constituents. Using graphene oxide (GO) as a model carbon nanomaterial, this thesis investigates how the nanoscale mechanical properties of GO-based nanocomposites can be modulated through its structure and interfacial interactions within the composite.

The effect of chemical structure on the stiffness and plasticity of single-layer GO was investigated through nanomechanical experiments. While stiffness decreases as the functionalization level of GO increases, this can be mitigated by tailoring the functional group distribution of GO to increase its plasticity. Under nanomechanical load, epoxide groups can transform into ether groups, providing an intrinsic toughening mechanism that imparts local ductility and damage-tolerance to single-layer GO at the atomic level. An extrinsic toughening mechanism was introduced by modifying single-layer GO with an ultrathin layer of polyvinyl alcohol, which can enable microscale crack bridging. Due to extensive hydrogen-bonding interfacial interactions between the oxidized domains of GO and the polymer, a toughness

comparable to single-layer graphene was achieved, and a three-fold increase in the load-bearing ability of GO was observed.

These nanoscale studies prompted the exploration of how GO structure at the single-layer level affects the mechanical properties of its bulk structures. While porosity, an inherent structural aspect of GO, dramatically lowers stiffness and strength at the single-layer level, these mechanical properties are much less sensitive in multilayer films assembled from porous GO sheets. The co-assembly of porous and pristine GO sheets surprisingly enhances the stiffness of multilayer GO films, as porous sheets can achieve more compliant packing within the film and effectively serve as a binder to strengthen interlayer interactions.

ACKNOWLEDGEMENTS

I would like to thank my thesis advisors, Profs. Jiaxing Huang and SonBinh T. Nguyen, for their support and mentorship throughout my time in graduate school. Without both of your guidance, this thesis would not have been possible, and I will always be grateful for having the opportunity to work with two mentors who have constantly pushed me to strive for excellence. Jiaxing, you taught me the importance of presenting research confidently, and that there will always be opportunities available if you seek them out. Your advice over the years has been honest, yet encouraging. SonBinh, you showed me the importance of being mindful in all things, from writing to conducting research, and that there is always room for personal growth and improvement. Your commitment to helping me become a better scientist and writer is amazing. Thank you both for all the time and energy you invested in me. I feel very fortunate to have learned from the experiences and perspectives of two advisors, and will take the lessons both of you taught me through the next stage of my life.

This thesis was also made possible by the contributions of many people who provided mentorship, collaborations, and support. I would like to thank my committee members, Profs. Horacio D. Espinosa, Mercouri G. Kanatzidis, and George C. Schatz, for their advice and helpful discussions over the years. I am also grateful for having the opportunity to learn from and collaborate with many talented and brilliant researchers during my time at Northwestern: Prof. Horacio D. Espinosa, Prof. Tae Hee Han, Prof. Xiaoding Wei, Prof. Wei Gao, Dr. Jeffrey T. Paci, Dr. Jianguo Wen, Dr. Dean Miller, Dr. Rafael A. Soler-Crespo, Mr. Hoang T. Nguyen, Mr. Xu Zhang, and Mr. Hun Park. Thank you all for teaching me about topics outside my field, and for your support over the years. I am especially thankful to my mentor, Dr. Zhi An, who offered guidance and helped me learn about graphene oxide research when I first started out.

I would also like to thank my parents for the sacrifices they made to ensure that I had opportunities for success. Thank you for raising me with a strong foundation of overcoming challenges, a mentality that has helped me throughout graduate school.

Lastly, my time in graduate school would not have been the same without my labmates and friends. You know who you are and I will always remember the experiences we shared together. Thank you for being there when I was struggling and encouraging me to believe in myself, for the long talks about life and research, and for teaching me more about myself.

TABLE OF CONTENTS

LIST OF TABLES

LIST OF FIGURES

Chapter 1

Introduction

1.1 Carbon Nanomaterial-Based Composites

To build structures such as automobiles, aircraft, and body armor with mechanical performance beyond what is currently possible, a key requirement is the development of novel lightweight materials that have high strength and toughness. To achieve this goal, carbon nanomaterials such as graphene, graphene oxide (GO), and carbon nanotubes (CNTs) are ideal candidates, given their low density and outstanding mechanical strength and stiffness that surpass those of materials typically used for structural applications (Figure 1.1).[1-4] Carbon nanomaterials must be assembled into a nanocomposite, due to their nanometer size, before they can be used to build macroscopic (centimeter to meter length) structures. However, attempts to construct bulk carbon nanomaterial-based composites have met with limited success to date, as the mechanical properties of these materials are orders of magnitude lower than those of the parent carbon nanostructures (Figure 1.1).[1,5,6]

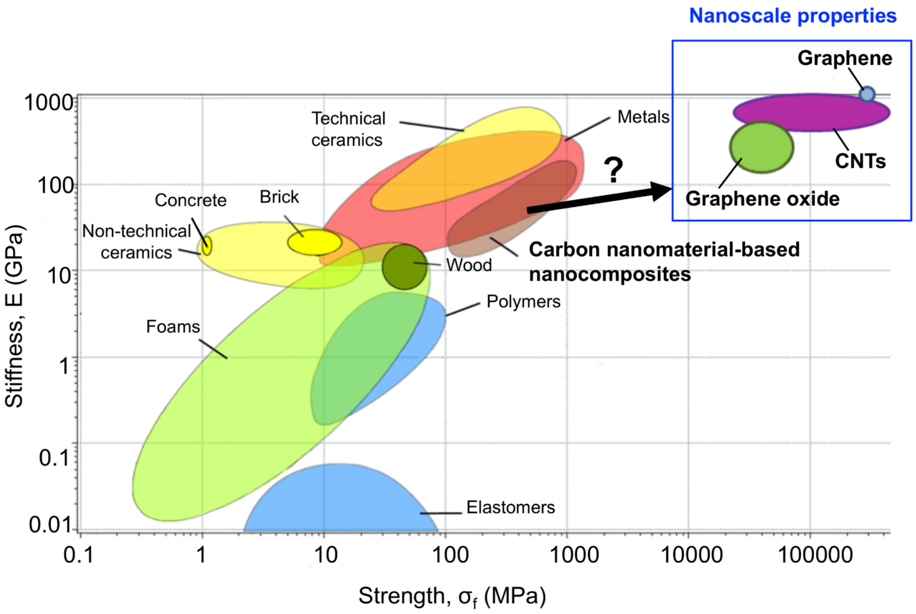

Figure 1.1 Ashby plot[7] of the strength and stiffness of different types of materials (adapted from Reference 8). The strength and stiffness of carbon nanomaterials (graphene, graphene oxide, and carbon nanotubes) significantly surpass those of other materials. However, carbon nanomaterial-based composites exhibit drastically reduced strength and stiffness.

In an attempt to bridge the gap between the mechanical performances of carbon nanomaterials and their macroscopic composites, researchers have fabricated synthetic composites using design principles derived from the structure of natural nanocomposites such as bone and nacre.[9-11] Such biological nanocomposites comprise hard inorganic and soft organic components that are assembled into complex hierarchical structures spanning the nano-, micro-, and macroscale (Figure 1.2).[12-14] The resulting macroscopic composite maintains most of the strength and stiffness of the mineral nanoparticles and simultaneously enhances their toughness.[9,13] It is this combination of nanomechanical property improvement and extension across all length scales that has made natural nanocomposites particularly attractive models to guide the design of carbon nanomaterial-based composites.

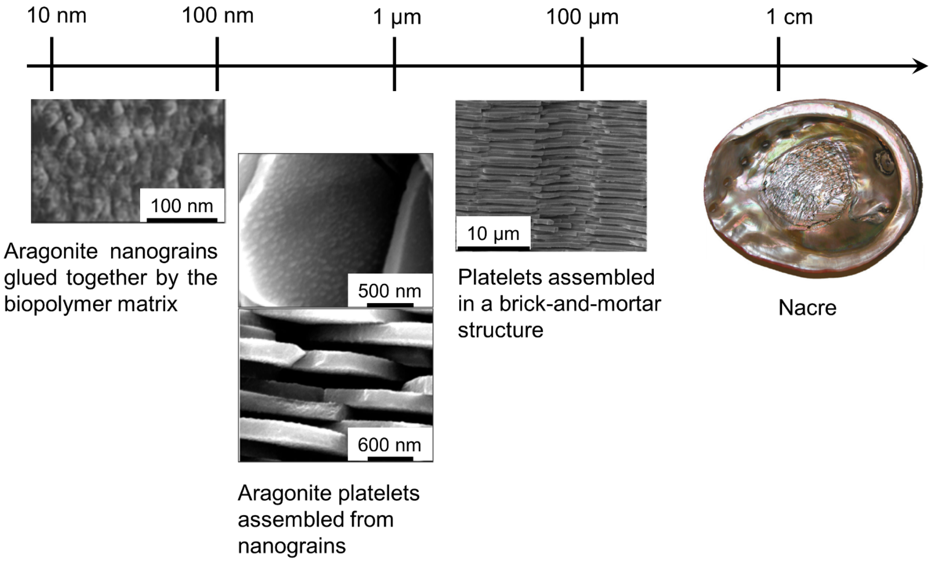

Figure 1.2 The hierarchical structure of nacre, showing the assembly of aragonite nanograins into complex structures that span across the nano-, meso-, and macroscale. Images obtained from the work of Barthelat et al.,[11] Luz et al.,[12] and Li et al.[15]

The hierarchical structure of nacre has often been used to guide the assembly of carbon nanomaterial-based composites.[16] Previous studies of nacre have revealed that one of the key design principles that enables its mechanical properties to span across the entire range of length scales is a hierarchical architecture based on nanometer-sized building blocks. Nacre comprises individual hard aragonite nanograins glued together by a soft biopolymer matrix,[17] then assembled into platelets that are held together by thin layers of the biopolymer matrix in a layered brick-and-mortar structure (Figure 1.2). This hierarchical architecture enables extensive interfacial interactions between the hard and soft components, another key design principle that enables the length-scale extension of mechanical properties in nacre. By assembling carbon nanomaterials with a soft matrix material following these design principles, it should be possible to similarly extend their mechanical properties to the resulting macroscopic composites.

To date, efforts to apply nacre design motifs to the fabrication of carbon nanomaterial-based composites have mainly focused on: 1) mimicking the layered nacre structure and 2) varying the components within a macroscopic composite,[16,19] without analyzing nanoscale composite systems to directly probe how the *nanoscale* structure and interfacial interactions of the constituents contribute to the overall mechanical properties. *i.e.,i.e.,*An example of the importance of studying nanoscale systems is highlighted in Chapter 3, where we demonstrate that only a nanometer-thick layer of polymer is needed to dramatically enhance the toughness of a nanoscale composite, a phenomenon that cannot be observed in the bulk counterpart. Extensive studies of nacre further confirm the importance of understanding nanoscale effects in materials by showing that nanoscale structure and interfacial interactions influence the mechanical properties of the composite at longer length scales (*i.e.,i.e.,* the macroscale).[15,22]

Without such a comprehensive understanding of structure and interfacial interactions at the nanoscale, the macroscopic approach of designing composites from the top-down has produced materials with high stiffness and strength, but with mechanical performance still well below that of their parent carbon nanomaterials.[20,21] This suggests that the successful design of macroscopic carbon nanomaterial-based composites must be guided by a comprehensive understanding of the mechanisms by which *nanoscale* structure and interfacial interactions of the constituents contribute to the *macroscale* mechanical properties of the resulting composite. *i.e.,i.e.,*As such, this thesis focuses on elucidating the mechanisms by which carbon nanomaterial structure and interfacial interactions affect the mechanical properties of nanoscale model systems that can function as nanometer-sized building blocks within a layered, nacre-like structure. This knowledge can then be extrapolated to the future design of macroscopic carbon nanomaterial-based composites with mechanical properties that more closely approach those of the parent carbon nanostructures.

1.2 Graphene oxide (GO) as a Model Carbon Nanomaterial

To fabricate nanoscale model systems with a nacre-like structure, we envision substituting the aragonite platelets of nacre with the carbon nanomaterial of choice, while the biopolymer matrix can be replaced with any soft material capable of extensive interactions with the carbon nanomaterial. The model carbon nanomaterial in such a scheme should: 1) have a two-dimensional structure (to construct a layered composite capable of serving as a nanoscale building block within a nacre-like assembly), and 2) be capable of diverse binding interactions with a variety of soft materials (to allow for tunable interfacial interactions). Graphene oxide (GO) fulfills these criteria due to its two-dimensional sheet structure and numerous oxygenated functional groups, and was therefore selected as the model carbon nanomaterial.

GO is a functionalized derivative of graphene that is synthesized by the oxidation and exfoliation of graphite,[23,24] with the distribution of GO functional groups and oxygen content easily tuned by varying the synthesis conditions.[25,26] Modifying the reaction parameters can also serve to vary the size and density of pores that are formed in the basal plane of GO sheets during the oxidation, providing another tunable structural feature. While the oxidation process lowers the stiffness and strength of GO (~250 GPa and ~40 GPa, respectively)[3,27,28] in comparison to graphene (1 TPa and 130 GPa, respectively),[2] the oxygenated functional groups impart GO with solubility in polar solvents and the ability to interact with a variety of soft materials,[24,29] unique properties that are unattainable in graphene. The solubility of GO allows for ease of processability and access to a wide range of composite assembly methods,[5,30,31] while the functional groups provide another avenue for the structure of GO to be tuned through covalent and non-covalent functionalization.[24] The aforementioned qualities allow GO structure and interfacial interactions to be readily tuned, and enable it to be easily assembled into nacre-like, layered composites.

1.3 Thesis Overview

The research described in this thesis focuses on the fabrication of nanoscale model systems that can serve as building blocks within a macroscopic nacre-like composite, and combines chemical characterization, nanomechanical testing, and computational studies to correlate nanoscale structure and interfacial interactions with the mechanical properties of these nanoscale model systems. Chapter 4 applies this knowledge to examine how nanoscale structure modulates macroscale mechanical properties in a bulk system. In Chapter 2, we employ the Langmuir-Blodgett technique to establish a method of fabricating single-layer GO systems with high reproducibility and fine control over sample morphology. Through nanomechanical testing of GO at the single-layer level, we discovered that the C-C bond in the epoxide groups of GO can be cleaved first under nanomechanical load, forming in-plane ether groups that impart local ductility and a unique damage-tolerance mechanism to single-layer GO sheets. Our results show that tuning the functional group distribution of GO provides a pathway to optimizing its nanomechanical properties, and suggest that GO is a promising two-dimensional building block with tailorable mechanical properties for the design of high-performance nanocomposites.

In Chapter 3, we extend the Langmuir-Blodgett fabrication method developed in Chapter 2 to produce GO-polymer composites, and discuss how an ultra-thin layer of polyvinyl alcohol on single-layer GO greatly enhances the toughness of the resulting GO-PVA nanolaminate through hydrogen-bonding interfacial interactions. As a proof of concept, the high toughness and two-dimensional elastic modulus of a single GO-PVA nanolaminate were successfully maintained when the thickness was doubled to a bilayer GO-PVA nanolaminate. Our results demonstrate the viability of using ultrathin polymer layers to enhance the toughness of two-dimensional nanomaterials, and imply that when designing carbon nanomaterial-based composites, only small amounts of polymer are necessary to achieve large enhancements in mechanical properties.

In Chapter 4, we modify the GO synthesis to tailor another aspect of its nanoscale structure, the in-plane porosity. The effect of porosity on the mechanical properties of GO single-layers is examined, and GO nanostructure and nanomechanical properties are correlated with the macroscopic mechanical performance of the corresponding multilayer films. While the stiffness and strength of GO at the single-layer level is greatly reduced as the porosity increases, we find that these mechanical properties in bulk multilayer GO films are much less sensitive to porosity. Co-assembly of soft and compliant porous GO sheets with near-zero stiffness can surprisingly improve the interlayer packing of multilayer GO films, thereby enhancing interlayer interactions and leading to a stiffening effect. These results establish that tailoring the in-plane porosity of GO at the single-layer level is a viable method to modulate its stiffness at the bulk level, and reinforce the importance of studying how nanoscale mechanical properties translate to the macroscopic materials. Finally, Chapter 5 summarizes the main findings of this thesis and presents a personal outlook on the field of carbon nanomaterial-based composites.

Chapter 2

The Effect of Chemical Structure on the Nanomechanical Properties of Single-Layer GO

Portions of this chapter appear in the following manuscript:

Wei, X.;[†] Mao, L.;[†] Soler-Crespo, R. A.;[†] Paci, J. T.; Huang, J.; Nguyen, S. T.; Espinosa, H. D., Plasticity and ductility in graphene oxide through a mechanochemically induced damage tolerance mechanism. *Nat. Commun.*, **2015**, *6*, 8029.

[†] Equal contribution

2.1 Introduction

As mentioned in Chapter 1, a fundamental understanding of nanoscale structure-mechanical property relationships in carbon nanomaterials is critical to elucidating how these nano-sized building blocks influence the mechanical properties of their macroscopic composites. The structure of carbon nanomaterials can be tuned by varying their method of preparation,[1,2] making it especially important to correlate structural differences with the resulting mechanical properties. In the case of an individual graphene oxide (GO) sheet, its local structure comprises graphitic domains (1-6 nm^2) interdispersed within a continuous network of oxidized domains, as well as intrinsic voids or pores (< 5 nm^2) within the basal plane of the sheet (Figure 2.1a).[3] Although several models have been proposed for the chemical structure of GO, the Lerf-Klinowski model is the most widely accepted.[1] According to this model, the oxidized domains within the basal plane of the GO sheet contain epoxide and hydroxyl groups, while the sheet edges are functionalized with carbonyl and carboxylic acid groups (Figure 2.1b).[4-6]

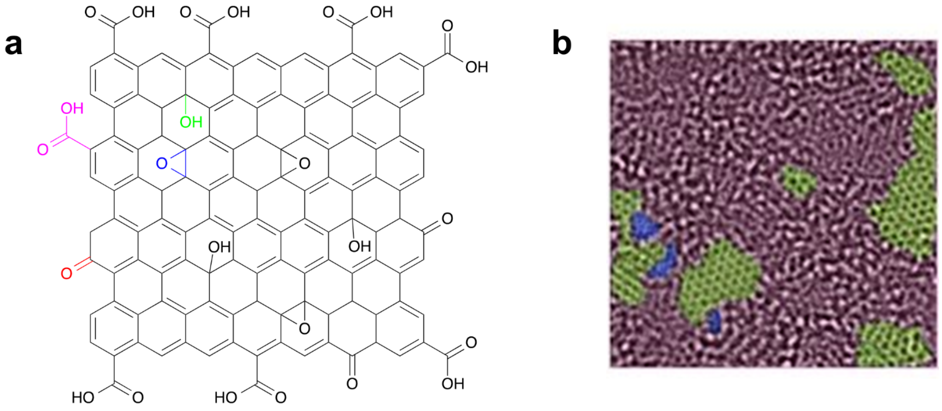

Figure 2.1 (a) Structure of GO based on the Lerf-Klinowski model. (b) Aberration-corrected high-resolution transmission electron microscopy (HRTEM) image of suspended single-layer GO, adapted from Reference 3. Oxidized domains are highlighted in purple, graphitic domains in green, and pores in blue. Scale bar is 2 nm.

Both the overall number and relative quantities of these functional groups can vary significantly based on the synthesis method used to produce GO.[7-9] Together, the functionalization level (the total number of functionalized carbon atoms), and the functional group distribution (the relative amount of each functional group present) describe the chemical structure of GO. This chapter focuses on correlating the chemical structure of GO with its nanomechanical properties and elucidating the mechanisms that give rise to the observed nanomechanical behaviors.

Numerous variations in the synthesis of GO have resulted in materials with significantly different functionalization levels (C/O ratio of 1.3-2.3) and functional group distributions (~0-60% of epoxides).[1,10,16] Previous studies have found that the mechanical performance of multilayer GO films is dependent on the functionalization level of the constituent sheets,[11] suggesting that the chemical structure of GO is one factor that can modulate the macroscopic mechanical properties of its bulk structures. Such differences presumably arise from variations in mechanical properties at the nanoscale level. Indeed, computational studies have shown that the functionalization level can play a role in determining the stiffness and strength of single-layer GO.[12] However, these results were not verified experimentally due to the challenges of fabricating and testing single-layer GO specimens. Only a few studies were able to measure the elastic modulus of single-layer GO prior to this thesis work, and although the reported values varied significantly,[13,14] differences in functionalization level were not explored as an origin of the discrepancy in measured mechanical properties. In addition, the possibility that the identity of the functional groups can also influence the mechanical properties of single-layer GO had not been considered at the start of this thesis work. Thus, it is critical to obtain a comprehensive and fundamental understanding of how the chemical structure of GO modulates its nanomechanical properties.

In this chapter, we correlate the functional group distribution and functionalization level of single-layer GO with its nanomechanical properties, using values that we obtained experimentally and those previously reported in the literature. To achieve this, X-ray photoelectron spectroscopy (XPS) was used to characterize the chemical structure of the GO used in this study (which revealed an epoxide-rich composition), and a precise and reproducible method of fabricating high-quality single-layer GO samples for nanomechanical measurements was developed. Based on these nanomechanical experiments and computational studies, we discovered that the epoxide-rich GO monolayers deviate from elastic mechanical behavior, exhibiting unique plasticity and damage-tolerance as a result of epoxide-to-ether transitions. This mechanism was verified through nanomechanical experiments on GO monolayers that were modified to remove epoxide groups. Importantly, the measured nanomechanical properties and extent of the observed plasticity were correlated with GO functional group distribution and functionalization level through our computational studies. These studies suggest that tuning the chemical structure of GO is a powerful way to optimize its mechanical behavior at the single-layer level.

2.2 Results and Discussion

2.2.1 Mechanical Characterization

The GO nanosheets used in this work were synthesized using a modified Hummers method,[15] and are extensively functionalized with epoxide groups based on X-ray photoelectron spectroscopy (XPS) analysis (Figure 2.6a, Section 2.4.5, and Table 2.1). To further confirm the epoxide-rich composition, we compared the C1s XPS spectrum of our GO to two other previously reported materials with well-characterized composition: highly oxidized GO with predominantly epoxide groups,[15] and less-oxidized GO with predominantly hydroxyl groups[16] (Sections 2.4.5-2.47). We found the composition and C1s XPS spectrum of our GO to be very similar to those of the epoxide-rich material, and markedly different from those of the epoxide-poor material (Table 2.1, Table 2.2, and Figure 2.8). To investigate how changes in the chemical structure of GO affect its nanomechanical properties, the epoxide groups were removed via ring-opening by *n*-butylamine to yield amine-modified GO (Section 2.2.3 and 2.4.3). By Langmuir–Blodgett deposition,[17] GO sheets were first deposited over an array of circular microwells that were prefabricated on a silicon substrate (Figures 2.7 and 2.8). The center of each individual circular membrane was then deflected with an atomic force microscopy (AFM) diamond probe to measure mechanical properties (Figure 2.11). Figure 2.2a,b show the two types of force versus deflection responses for suspended GO membranes that correspond to ductile and brittle failure modes, respectively. In the ductile failure mode, the force-versus-deflection response can only be fit to a linear elastic membrane solution (cf. Equation 2.2) during the initial stage of deflection, beyond which (~40 nm) the suspended GO monolayer deformed inelastically until rupture. In contrast, the linear elastic behavior is observed throughout the deflection in the brittle failure mode. At the peak force, an abrupt increase in deflection occurred, indicating sudden film rupture.

Notably, only 1 suspended GO monolayer among the 19 that we tested showed brittle failure, most likely due to the occasional large (*i.e.,*, >10 nm) defects in the basal plane of the GO nanosheet, which comprises relatively uniform, randomly distributed graphitic domains (3-5 nm^2) within a continuous network of oxygenated carbon atoms.[1,3,6] A typical AFM image of the ruptured ductile GO monolayer (Figure 2.2c) clearly shows a localized puncture at the center, which is in remarkable contrast to the catastrophic rupture of pristine graphene or less-oxidized GO containing mainly hydroxyl groups (Figure 2.2e,d).[16,18] The radius of the tear was ~150 nm, which is consistent with the dimension of the tip cross-section at maximum penetration, suggesting the presence of a unique crack-arresting mechanism in GO. This is confirmed in a second set of experiments, where the AFM tip was retracted quickly after reaching the maximum load but before membrane rupture. AFM images of these GO membranes before and after deflection clearly show a ‘damage’ zone at the membrane center (Figure 2.2f,g), ~100 nm in diameter and 1–2 nm higher than the undamaged region, where the material underwent a severe plastic deformation.

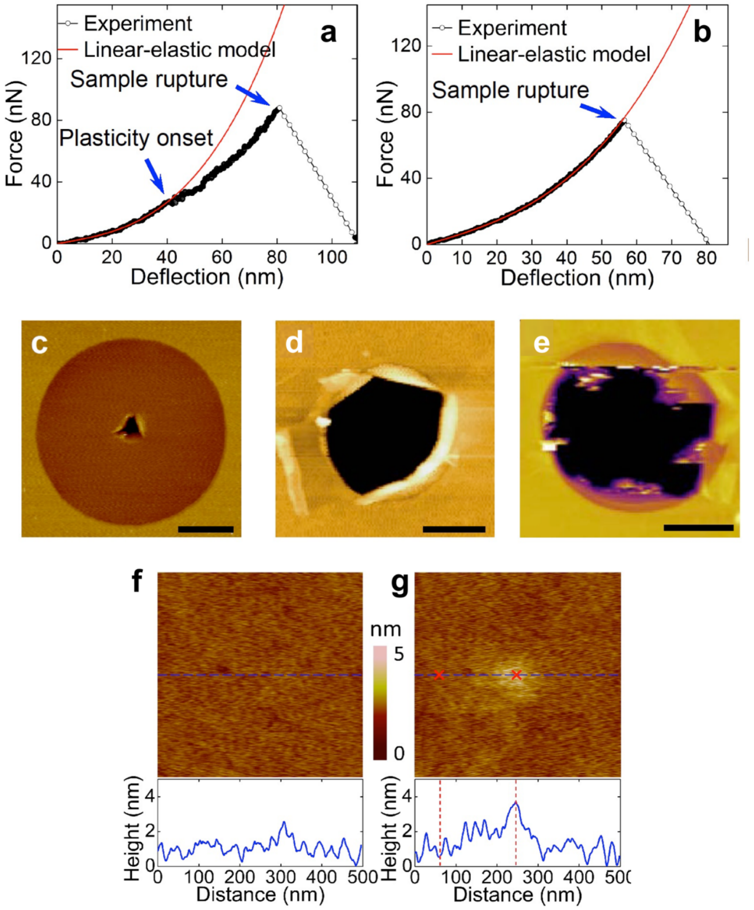

Figure 2.2 (a,b) Typical ductile and brittle force-versus-deflection curves for suspended GO membranes. (c) AFM topology image of ruptured monolayer GO after membrane deflection tests. (d,e) AFM topology images of ruptured pristine graphene and less-oxidized GO, respectively, after membrane deflection tests (images were adapted from the works of Lee *et al.*[18] and Cao *et al.*[16] (f,g) AFM scanning images of a 500 × 500 nm area at a suspended GO membrane center before (f) and after (g) testing. Scale bar, 500 nm (c,d). Scale bar, 1 µm (e).

2.2.2 Theoretical Analysis

To explore the origin of the experimentally observed plasticity, we modelled the tensioning of graphene and GO through a series of semi-empirical DFTB calculations using the open-source code CP2K (http://www.cp2k.org/). We first generated a molecular model of a ~2 × 2 nm^2 GO sheet with a functionalization level $\varphi = 0.7$ (defined as the fraction of oxidized carbon atoms). A 4:1 epoxide-to-hydroxyl functional group ratio was used to mimic the epoxide-rich composition confirmed by XPS analysis. A Monte Carlo-based Rosenbluth sampling algorithm was employed to determine the favorable locations of the functional groups from random choices according to a Boltzmann-like distribution (see Section 2.4.12 for the algorithm implementation). The obtained model shows excellent agreement with structural features previously reported for theoretically studied GO sheets in the literature (Section 2.4.13).[12,19-23] Then, we carried out molecular mechanics and molecular dynamics calculations to investigate the plasticity mechanism by applying equibiaxial tension on the nanosheet (Figure 2.3a), similar to the constraint on the material during membrane deflection experiments.

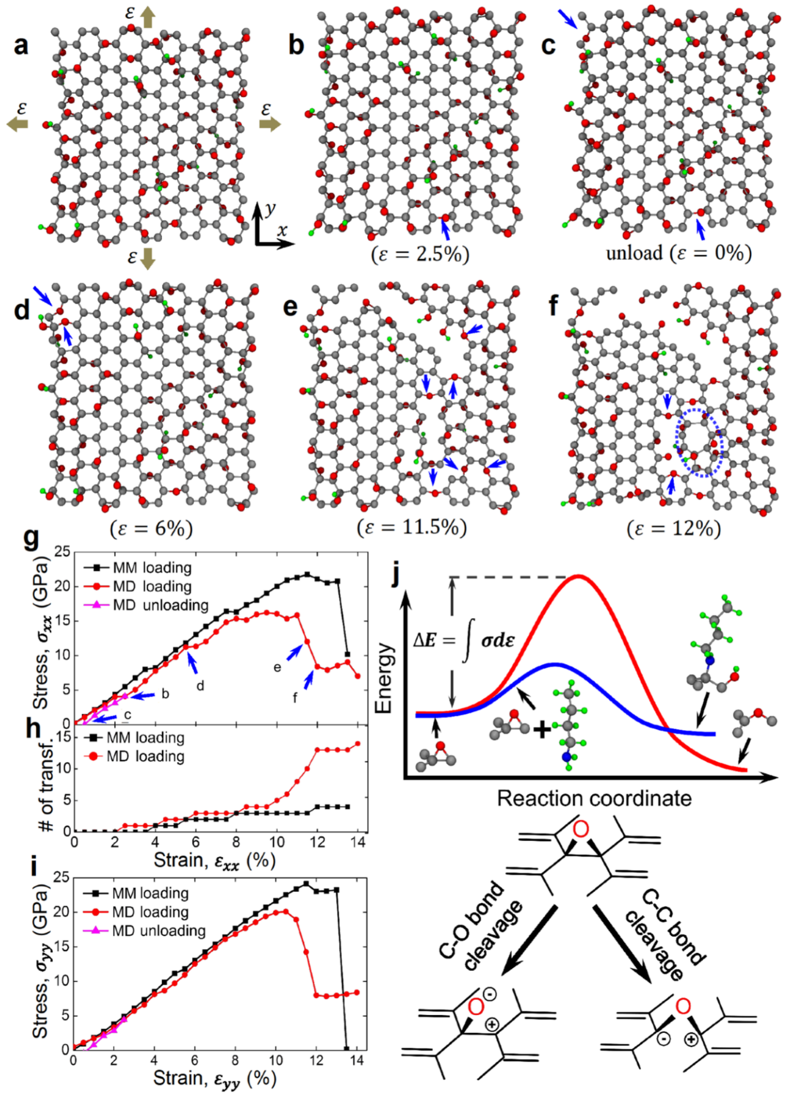

Figure 2.3 (a) The initial configuration of the GO sheet and the schematic of the constraints. Grey, red and green beads represent carbon, oxygen, and hydrogen atoms, respectively. (b–f) The snapshots of the deformed GO sheet during molecular dynamics (MD) simulations. The dark-blue arrows highlight the locations where epoxide-to-ether transformations occurred. The dashed circle in snapshot f highlights a Stone–Wales defect. (g) Stress–strain curves in the armchair direction (*x* axis in a) obtained from molecular mechanics and MD simulations. Labels in stress–strain curve refer to MD snapshot panels in this figure. (h) Accumulated number of epoxide-to-ether transformations as a function of strain. (i) Stress–strain curves along the zigzag direction (*y* axis in a). (j) An illustration of the relative energetic difference between the mechanochemically induced epoxide-to-ether transformation activated by strain energy (that is, C–C bond cleavage, red profile) and the epoxide ring-opening by *n*-butylamine (that is, C–O bond cleavage, blue profile). Grey, red, green, and blue beads represent carbon, oxygen, hydrogen, and nitrogen atoms, respectively. The chemical drawings beneath the profiles are

included only to illustrate the key differences between the two chemical pathways without including all the relevant species (water, *n*-butylamine, etc.) that can be involved to facilitate the transformations. As such, the formal charges that are indicated on the drawings should not be taken literally.

As shown in Figure 2.3g, the stress–strain response of the GO nanosheet along the armchair direction shows strain bursts at 3.5% strain in molecular mechanics (and 2% strain in molecular dynamics) simulations that appear to correspond with a mechanochemical epoxide-to-ether transformation reaction (Figure 2.3b). This reaction, biased by strain energy (Figure 2.3j), activated at stress levels of 8.0 GPa in molecular mechanics and 4.0 GPa in molecular dynamics simulations, respectively. The lower stress obtained from molecular dynamics (at 300 K) in comparison with molecular mechanics (at 0 K) suggests that this strain-energy-activated mechanochemical transformation is more favorable at ambient temperature, where the experiments were carried out. The ether groups that formed through C-C bond cleavage remained after unloading from 2.5% strain to 0% strain in our molecular mechanics simulation (Figure 2.3c), confirming that this reaction is irreversible and deformation is plastic.

In a previous density functional theory (DFT) study, Li *et al.* elucidated graphene and carbon nanotube unzipping during oxidative processes.[24] They showed that a spontaneous epoxide-to-ether transformation would happen if multiple epoxide groups align on the opposite ends of benzene rings in the same side of the graphitic basal plane to form a linear fault line. However, this particular configuration of linearly aligned epoxy groups considered by Li *et al.* is only a transient state (that is, highly unstable), and is statistically unlikely in the case of the stable suspended GO membranes studied herein. The GO models, generated in this study using the Monte Carlo algorithm, suggest that this fault line of epoxide groups is energetically unfavorable. Rather, our study reveals that epoxide groups in GO are randomly distributed and form a stable structure. The epoxide-to-ether transformation occurs only when the GO sheet is under a substantial mechanical stress (between 4.0 and 8.0 GPa) and leads to improved material toughness. Thus, considering these essential distinctions, the scenarios discussed by Li *et al.* and herein are significantly different.

As the strain increased, more epoxide-to-ether transformations accumulated (Figure 2.3h); at 6% strain, a second major strain burst was observed in the molecular dynamics stress–strain curve (Figure 2.3g) as the result of the strain energy release at the bond transformation locations (Figure 2.3d). At 9.5% strain, a nanoscale crack appeared in our simulation model (Figure 2.3e) but did not lead to a catastrophic failure of the material. Rather, it corresponds to a significant number of mechanically induced epoxide-to-ether transformations as the strain was increased (Figure 2.3h). The accumulation of these transformations led to a plateau in the stress–strain curve, indicating a delay in crack growth. At the end of this plateau, crack growth led to a stress drop and failure. The transition captured in Figure 2.3e,f clearly shows that the epoxide-to-ether transformation at the crack front is responsible for energy dissipation, presumably due to the blunting of the crack front by the higher flexibility offered by the C–O–C angle in the newly formed ether group. At 12% strain, a void initiated near the crack tip, and a Stone–Wales defect, commonly observed during failure in graphitic materials,[25] formed beside the void (Figure 2.3f).

As described above, the molecular dynamics stress–strain curve shown in Figure 2.3g clearly demonstrates the plasticity and damage tolerance of GO when being tensioned in the armchair direction. In contrast, the corresponding stress–strain curve in the zigzag direction (Figure 2.3i) exhibits negligible plastic behavior, suggesting that the mechanochemical response to strain energy in GO is chirality dependent. Together, these results provide an unexpected explanation for the predominantly ductile failure mechanism in our experiment: as shown by the molecular dynamics snapshots in Figure 2.3a-f, the novel epoxide-to-ether transformation that occurs on the basal plane of a GO nanosheet on indentation can readily accommodate a network of nanoscale cracks and prevents it from catastrophic failure until these nanocracks coalesce. This is consistent with the experimental observation of a damage zone in the suspended GO membrane after testing (Figure 2.2g).

2.2.3 Amine Modification of GO Sheets

Our results thus far suggest that the epoxide-to-ether transformation in the basal plane of GO is the origin of the plasticity and the ductile failure behavior that we observe in our experiments. Therefore, if the epoxide groups are removed such as through amine-induced ring-opening reactions,[26] GO should show a more pronounced brittle failure behavior. This is indeed the case: when 18 samples of *n*-butylamine-modified GO (A-GO) were tested, brittle failure was observed much more frequently than in the case of GO. Eight of the samples exhibited clear brittle failure (Figure 2.4b), and while the remaining samples showed a ductile failure behavior (Figure 2.4a), the degree of plastic deformation in them is significantly less than that in the GO membranes discussed earlier (cf. Figure 2.2a). Furthermore, the typical rupture topology of a suspended monolayer A-GO membrane that exhibited brittle failure (Figure 2.4b) showed features that are similar to those in pristine graphene and less-oxidized GO containing mainly hydroxyl groups (Figure 2.2e,d).[16,18] Together, these data support our assertion that the presence of epoxide groups, and thus the availability of epoxide-to-ether transformations, is responsible for the plasticity of the original GO samples. Presumably, the ring-opening reactions of the epoxide groups by *n*-butylamine[26] (Section 2.4.5 and Figure 2.6b) have rendered A-GO more brittle.

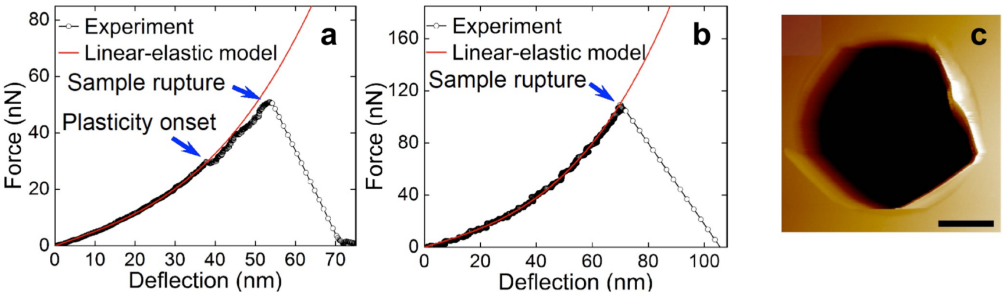

Figure 2.4 (a,b) Typical ductile and brittle force-versus-deflection curves for suspended A-GO membranes. (c) AFM topology image of ruptured monolayer A-GO after membrane deflection tests. Scale bar, 500 nm.

The pre-stress and elastic modulus values of our GO and A-GO, as derived from the elastic analysis of the experimental measurements (Section 2.4.11 and Figure 2.12) also support our conclusion. Assuming an effective GO thickness of h = 0.75 nm,[27] the higher pre-stress in A-GO (0.9 ± 0.2 GPa) compared with that for our original GO with $\varphi = 0.7$ (0.65 ± 0.3 GPa) suggests that amine modification did indeed increase membrane tension. We note that the value for our original GO was notably higher than that reported by Cao *et al.*[16] (0.14 ± 0.02 GPa by assuming the same GO thickness h = 0.75 nm) with $\varphi = 0.2$, presumably due to stronger interactions between the basal planes of our highly oxidized nanosheets and the substrate. In contrast, the elastic modulus of A-GO is 223.3 ± 33.2 GPa, which is slightly lower than that of the original GO with $\varphi = 0.7$ (elastic modulus E = 256.4 ± 28.2 GPa; elastic modulus in two-dimensional (2D) form E^{2D} = 192.3 ± 21.2 N m^{-1}) as a result of the ring opening of the epoxide groups. Both of these values are much lower than those reported by Cao *et al.*[16] (E = 384 ± 31 GPa, E^{2D} = 269 ± 21 N m^{-1}) for a GO sample with $\varphi = 0.2$, suggesting that the elastic modulus for GO decreases with increasing levels of functionalization. This conclusion is further supported by the good agreement between our experimental measurements and the predicted elastic properties extracted from additional DFTB calculations on GO nanosheets with various functionalization levels (φ = 0.1, 0.2, 0.36, 0.7 and 0.9) (Figure 2.5a, Section 2.4.16, Figure 2.15, and Table 2.4). Furthermore, our DFTB simulations agree very well with DFT predictions by Liu *et al.* for disordered GO models at the same functionalization levels despite differences in functional group ratios (a 1:2 epoxide-to-hydroxyl group ratio was used by Liu *et al.*, evidently different from ours).

In addition, we note with interest that the GO studied by Cao *et al.* (with a 20% functionalization level but a hydroxyl-rich composition) yields an elastic modulus also in agreement with our DFTB predictions for the GO model with a 20% functionalization level but an epoxide-rich composition. Therefore, we may reasonably assume that the elastic modulus of GO is mainly affected by the functionalization level, rather than by the relative proportions of different oxygen-containing functional groups. More specifically, the studies by Cao *et al.* and Liu *et al.* and this study contain the same relative amounts of sp^2- versus sp^3-type carbon–carbon bonding in systems with the same functionalization level, independent of the relative amounts of each functional group present. Thus, one can reasonably expect that the overall electronic structure of the GO backbone dominates the measured elastic properties (*i.e.,i.e.,* stiffness and pre-stress) of the material, whereas the identity of the bonded functional groups directly influences the deviation from elastic mechanical behavior (*i.e.,i.e.,* the extent of observed plasticity).

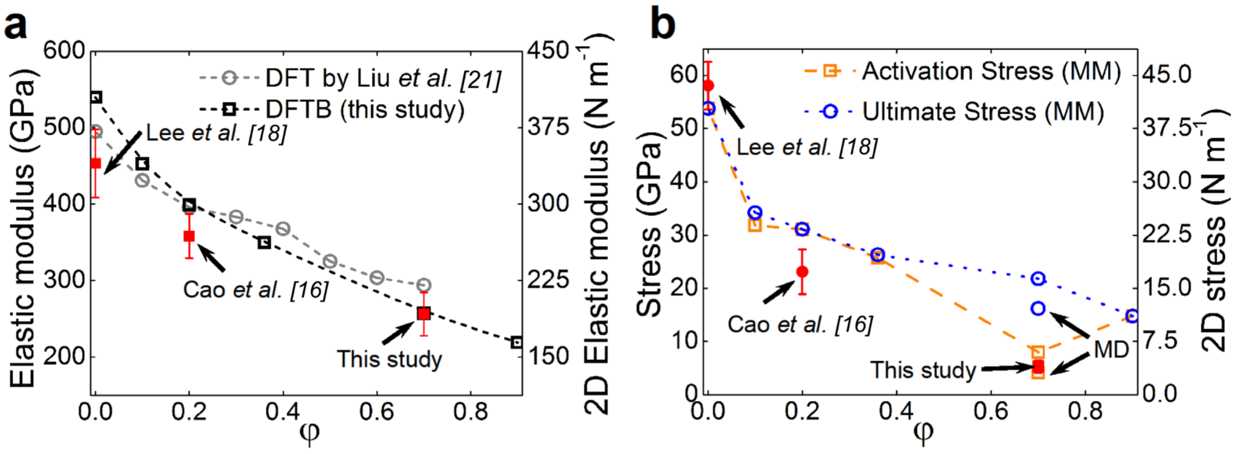

Figure 2.5 (a) Comparison of elastic moduli predicted by density functional theory (adopted from Reference 21) and density functional-based tight-binding (DFTB) for GO with increasing φ with experimental results for graphene (that is, $\varphi = 0$) from Reference 18, GO with $\varphi = 0.2$ from Reference 16, and GO with $\varphi = 0.7$ (this study). (b) Comparison of ultimate and activation stresses predicted by molecular mechanics with values reported for graphene (three-dimensional stress was converted by assuming a GO thickness of $h = 0.75$ nm), GO with $\varphi = 0.2$ and GO with $\varphi = 0.7$. Molecular dynamics predictions of ultimate and activation stresses for GO with $\varphi = 0.7$ are also plotted. Hollow and solid symbols represent DFTB predictions and experimental results, respectively. Error bars refer to standard deviations.

2.2.4 Effect of Functionalization Level and Functional Group Identity

To further elucidate the extent to which epoxide groups, unlike hydroxyl groups, enable GO to deform plastically, we compared the fracture surfaces obtained by Cao *et al.* with those obtained in our study (with a 70% functionalization level and an epoxide-rich composition). Cao *et al.* experimentally showed that the fracture surfaces of hydroxyl-rich GO tend to be brittle. DFT simulations predict that, for membranes of this composition, brittle failure occurs along a path populated by hydroxyl-functionalized carbon atoms. In contrast, our study shows that epoxide-rich GO fails in a ductile manner. Our simulations suggest that crack propagation is hindered due to energy dissipation through epoxide-to-ether transformations. Thus, one can reasonably conclude that the presence of epoxide groups enables GO to exhibit plastic behavior.

Analyzing the stress at the onset of plasticity allows us to further relate the material strength of GO with its level of functionalization. In contrast to the case of pristine graphene, which is nearly defect-free,[18] it is impossible to define an ‘intrinsic material strength’ for GO. Instead, we used the term ‘activation stress’ to describe the onset of the plastic deformation of GO, which is defined as the stress value at the membrane center when the sample is at the plastic onset point, the last data point where the material behaves linear elastically. Since this is the first point in the stress–strain curve where plastic behavior begins, the activation stress is analogous to the yield stress in metals. Thus, using contact analysis in the linear elastic regime,[28] the activation stress is given by

$$\sigma = \sqrt{\frac{FE}{4\pi hR}} \qquad 2.1$$

where F is the force at the plastic onset point and $R = 25$ nm is the tip radius of the AFM probe. The experimentally determined activation stress (see Section 2.4.11) of a suspended monolayer GO is thus 5.3 ± 1.2 GPa (or 4.0 ± 0.9 N m^{-1}), consistent with the mechanical stress applied in our DFTB simulation at the point where epoxide-to-ether transformations were activated for a GO nanosheet with $\varphi = 0.7$. Given this good agreement, further equibiaxial tension simulations on GO samples with varying functionalization levels (Section 2.4.16, Figure 2.15) then allow us to construct a relationship between the activation stress for the epoxide-to-ether functional group transformation and the material strength of these samples. In particular, the difference between the activation and ultimate stresses can now be used to indicate the extent of GO plasticity. As shown in Figure 2.5b, while the predicted ultimate stress for GO decreases monotonically with increasing φ, the activation stress decreases up to $\varphi = 0.7$ and then increases. This behavior suggests that while the level of plasticity in GO can be increased by increasing its propensity to undergo epoxide-to-ether transformations, its effect is countered by the loss of material heterogeneity for systems with $\varphi > 0.7$. Beyond this level of functionalization, further oxidization leads to the removal of graphitic domains (that is, loss of heterogeneity) so that higher strain energies are required to activate mechanochemical reactions, and, thus, loss of plasticity. This trend may also explain why this epoxide-to-ether transformation induced plasticity was not observed in previous experimental and theoretical studies of GO with either low functionalization levels or low epoxide populations;[12,16,21] sufficient functionalization levels and adequate epoxide populations are both needed for GO plasticity to become apparent.

2.3 Conclusion

In summary, we have established a molecular-level understanding of the correlation between the chemical structure (functional group distribution and functionalization level) of GO and its nanomechanical properties through a synergistic combination of experimental and theoretical investigation. A novel epoxide-to-ether transformation was found to be responsible for the plasticity and ductility of GO as observed in AFM membrane deflection experiments, revealing that the identity of GO functional groups directly influences its mechanical properties. This suggests that the mechanical properties of GO sheets can be tuned through its chemical structure. Importantly, the elastic modulus, strength, and plasticity of single-layer GO can be optimized by tuning the functionalization level and functional group distribution, as suggested by our computational results. These findings reveal a unique relationship between the chemical structures and mechanical properties of GO at the nanoscale, and establish GO as a two-dimensional building block with highly tunable mechanical properties for the design of high-performance nanocomposites.

2.4 Materials and Methods

2.4.1 Materials

Unless otherwise stated, all reagents were used as received. Graphite powder (grade 2139) was purchased from Asbury Carbons Inc. (Asbury, NJ). Sodium nitrate, potassium permanganate, absolute ethanol, concentrated hydrochloric acid, and *n*-butylamine (99.5%) were purchased from Sigma-Aldrich Co., LLC (Milwaukee, WI). Concentrated sulfuric acid, ether, and methanol were purchased from VWR International LLC (Radnor, PA). Phosphoric acid (85 wt %) was purchased from Mallinckrodt Baker Inc. (Phillipsburg, NJ). Hydrogen peroxide (30 wt % in water) was purchased from Sigma-Aldrich Co., LLC (Milwaukee, WI) and refrigerated during storage. Ultrapure deionized water (resistivity 18.2 MΩ cm) was obtained from a Milli-Q Biocel A10 system (Millipore Inc., Billerica, MA). Silicon wafers (Item # 785, 100 mm diameter, p-type, B-doped, single-side polished) and silicon wafers with a 500-nm-thick thermal oxide layer (100-mm diameter, N/Phos-doped, single-side polished) were purchased from University Wafer Inc. (Boston, MA).

2.4.2 Synthesis of Graphene Oxide

Graphite oxide was prepared using a modified Hummer's method.[15] Briefly, a 9:1 v/v mixture of concentrated H_2SO_4 (360 mL):H_3PO_4 (40 mL) was added to a mixture of graphite (3 g) and potassium permanganate (18 g). The reaction mixture was heated to 50 °C and stirred for 12 h. The mixture was cooled to room temperature and poured over ice (~400 mL). Then, H_2O_2 (8 mL of a 30 wt % solution) was added until the solution turned bright yellow. The resulting graphite oxide was filtered through a 250 μm US Standard testing sieve (VWR International LLC, Radnor, PA) and centrifuged (840 *g* for 1 h) in a model 5804R centrifuge (Eppendorf Inc., Westbury, NY) with the supernatant decanted away. The remaining solid was then washed with ultrapure deionized water (200 mL), HCl (200 mL of a 30 wt % solution) and EtOH (2 × 200 mL). For each wash, the mixture was filtered through the sieve and then centrifuged (840 *g* for 1 h) with the supernatant decanted away. The remaining material was coagulated with ether (200 mL) and filtered over a polytetrafluoroethylene (PTFE) membrane (Omnipore, 5 µm pore size, Millipore Inc., Billerica, MA) overnight. The GO filter cake was then dispersed in ultrapure deionized water, with the dispersion stirred overnight. Any residual unexfoliated graphite oxide was removed by centrifuging at 840 *g* for 5 min 2x with the precipitate discarded. The final dispersion contained ~1 mg mL^{-1} of GO, with a C:O ratio determined by elemental analysis to be 1.13. Accounting for a water content of 14.53% results in a C:O ratio of 1.57. GO films for XPS analysis were prepared by drop-casting GO solution onto silicon wafers with a thermal oxide layer, followed by drying under ambient conditions.

2.4.3 Preparation of Amine-Modified Graphene Oxide

Suspended GO monolayers were deposited on patterned Si substrates by the Langmuir–Blodgett technique (see procedure in Section 2.4.9). The substrates were then placed next to three drops of *n*-butylamine on a glass slide inside of a closed petri dish and left overnight. XPS characterization of these A-GO samples (Section 2.4.5) was carried out after membrane deflection experiments were performed.

2.4.4 Characterization

XPS was performed in the KECK-II/NUANCE facility at NU using a Thermo Scientific ESCALAB 250Xi (Al Kα radiation, $h\nu = 1{,}486.6$ eV) (Thermo Fisher Scientific Inc., West Palm Beach, FL) equipped with an electron flood gun. XPS data were analysed using Thermo Scientific Avantage Data System software (version 5.923), and a SMART background was subtracted before peak deconvolution and integration. Scanning electron microscopy (SEM) images were taken using a FEI NovaNano 600 scanning electron microscope (FEI Co., Hillsboro, OR). Carbon, hydrogen, and nitrogen (CHN) elemental analysis by combustion and oxygen elemental analysis by pyrolysis were performed by Micro Analysis Inc. (Wilmington, DE), with samples dried at 80 °C under vacuum for 4 h. Water content was measured by Karl Fischer titration using a C20 Compact Karl Fischer Coulometer (Mettler-Toledo International Inc., Columbus, OH) on films dried at 80 °C under vacuum for 4 h, and bath-sonicated for 5 min in dry MeOH in a sealed vial. Water contact angles were measured using a VCA Optima contact angle instrument (AST Products Inc., Billerica, MA) by dropping 4 μL of ultrapure deionized water onto the substrate, with measurements taken at three different locations on each substrate.

2.4.5 XPS Analysis of GO and A-GO

XPS is a powerful technique for the characterization of the surface chemical composition of nanomaterials, and has been extensively used to study functional groups in GO.[1,29] While XPS can detect these functional groups with high accuracy, the resulting C1s spectrum consists of several overlapping peaks corresponding to the different types of carbon atoms present. To accurately quantify the amount of each functional group, the C1s XPS spectrum must be carefully deconvoluted using the correct binding energies and number of peaks. Among previously reported studies, variation in the binding energy assigned to each functional group is presumably due to the heterogeneous chemical structure of GO. Whereas the structural model of GO includes five types of functional groups, some researchers may choose to assign only four peaks to simplify deconvolution. For example, a common practice is to fit the epoxide and hydroxyl groups as a single peak, rather than as two separate peaks. However, this does not imply that XPS cannot distinguish between epoxide and hydroxyl groups. Although these two groups are expected to have similar binding energies, the epoxide group (C-O) can exhibit a larger chemical shift (relative to the C-C group) into the emission range of the carbonyl group (C=O).[29] Indeed, several previous works separately deconvoluted and quantified epoxide and hydroxyl groups.[30-32]

The C1s XPS spectrum of GO was deconvoluted into five peaks corresponding to the functional groups and binding energies (BEs) listed in Table 2.1. Binding energies were based on previously reported values[26] and are in good agreement with the literature.[15,29-32] All spectra were calibrated by assigning the binding energy of the graphitic peak (C-C) at 284.46 eV. The C-C binding energy is normally assigned at 284.5-285.0 eV, with chemical shifts of +1.5, +2.5, and +4.0 eV typically assigned to the functional groups of C-OH, C=O, and C(O)-O, respectively.[33] We fit the epoxide and hydroxyl groups separately, assigning the peak at 285.90 eV to the C-OH group and the peak at 286.52 eV to the C-O group. The peaks at 287.88 eV and 289.42 eV were attributed to the C=O and C(O)-O group, respectively. Based on this analysis, the percentage of graphitic carbon atoms (C-C) in our unmodified GO is 27.4%, while the oxidized carbon atoms consist mainly of epoxides (C-O, 60.6%).

The C1s XPS spectrum of A-GO was deconvoluted into seven peaks corresponding to the five functional groups of GO and two additional groups arising from the amine modification (Table 2.1). Binding energies were based on previously reported values for amine-modified GO.[26] In contrast to the unmodified GO, the percentage of graphitic carbon atoms in A-GO is 65.8%, and that of C-O carbon atoms is 7.2%, suggesting the removal of epoxide groups and reduction of GO after amine functionalization. As noted in Section 2.2.3, the removal of epoxide groups (the source of ductility in GO) is expected to lead to brittle failure of GO in membrane deflection tests. However, both brittle and ductile failure modes for A-GO were observed, which can be attributed to the remaining epoxide groups that were not ring-opened.

Additional peaks in the deconvoluted C1s XPS spectrum of A-GO corresponding to amine (C-N, 4.7%) and amide (C(O)-N, 10.4%) carbon atoms are further evidence of the successful amine modification of GO (Figure 2.6b). The N1s XPS spectrum of A-GO contains a peak (Figure 2.6b), indicating the presence of nitrogen in A-GO. However, the weak intensity of this peak suggests low nitrogen loading, which is consistent with the low percentage of C-N and C(O)-N carbon atoms in the C1s XPS spectrum of A-GO (Figure 2.6b and Table 2.1). The low nitrogen content of A-GO can be explained by the spontaneous elimination of vicinal amine and hydroxyl groups formed during the ring-opening of epoxides by n-butylamine. We propose that these vicinal groups possess a *syn* configuration as one face of the GO single-layer is anchored to the substrate and is thus inaccessible to amine functionalization. This is analogous to the case of vicinal *syn*-diols, which simulations predict would spontaneously detach from the GO surface.[34] Vicinal amine and hydroxyl groups may be similarly unstable due to the angle strain of tetrahedral carbons in a planar structure and Pitzer strain (Figure 2.7a) and can react further to result in loss of N-(*n*-butyl) hydroxylamine and reduction of the carbon backbone (Figure 2.7b). This elimination of vicinal amine and hydroxyl groups explains the low percentage of C-N and C(O)-N carbon atoms, as well as the small increase (3.5%) in the percentage of C-OH carbon atoms and the reduction of GO after amine modification.

Table 2.1 Tabulated XPS peak locations and intensities for GO and A-GO.[26]

Graphene oxide (GO)		
	BE (eV)	Relative Area
C-C	284.46	27.4%
C-OH	285.90	2.3%
C-O	286.52	60.6%
C=O	287.88	9.5%
C(O)O	289.42	0.3%

Amine Graphene Oxide (A-GO)		
	BE (eV)	Relative Area
C-C	284.54	65.8%
C-OH	285.95	5.8%
C-O	286.69	7.2%
C=O	288.18	6.3%
C(O)O	—	—

C-N	—	—
C(O)-N	—	—

C-N	286.48	4.7%
C(O)-N	287.43	10.4%

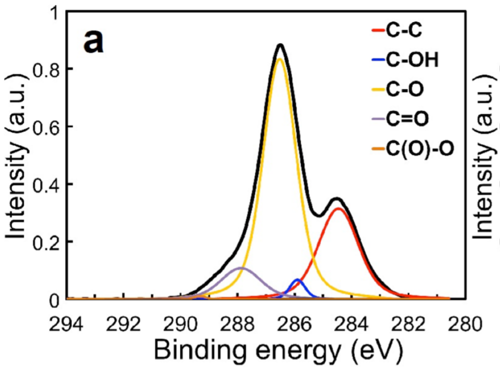

Figure 2.6 (a,b) C1s XPS spectra for GO (a) and A-GO (b), respectively. (b, inset) N1s XPS spectrum for A-GO.

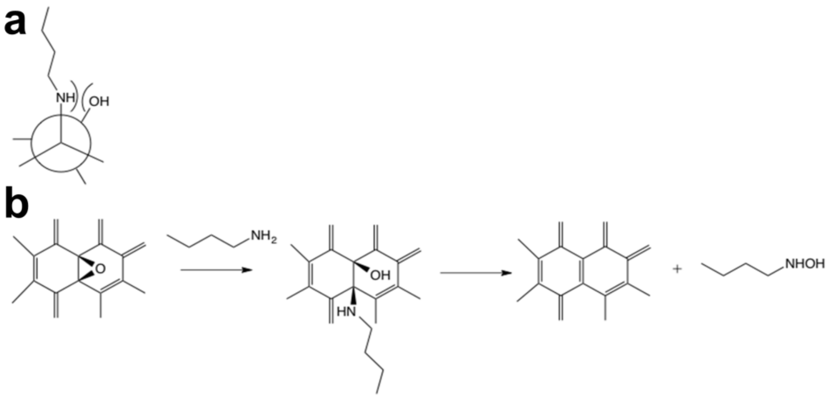

Figure 2.7 (a) Newman projection of the vicinal amine and hydroxyl groups, illustrating the Pitzer strain. (b) Reaction scheme of *n*-butylamine functionalization of GO, showing the elimination of vicinal amine and hydroxyl groups with a *syn* configuration.

2.4.6 Comparisons of Our XPS Spectra with Previously Reported Literature

To further confirm the epoxide-rich composition of our GO sample, we compared our C1s XPS spectrum to those of previously reported materials with well-characterized composition: highly oxidized GO with predominantly epoxide groups (synthesized by the same method we used),[15] and GO with low oxidation level and predominantly hydroxyl groups.[16] We expected our spectrum to match closely with the epoxide-rich GO and to differ dramatically from the epoxide-poor GO. As stated previously, there is variation in the reported binding energies of GO functional groups and in the number of fitted peaks used by researchers. Therefore, to make a valid comparison between all three spectra and prevent misinterpretation, the three spectra were analyzed using the same method (see above), with the peaks assigned to the same binding energies (Figure 2.8).

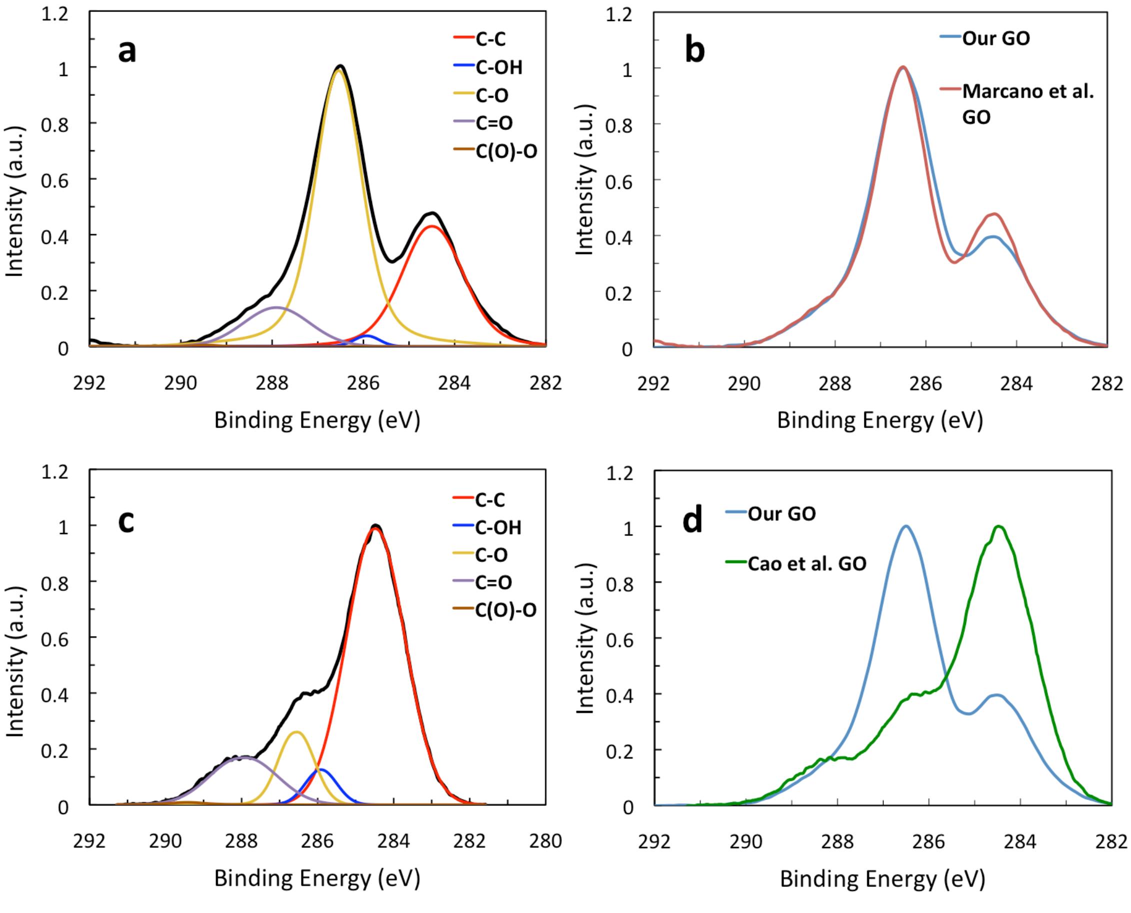

Figure 2.8 (a) Deconvoluted C1s XPS spectrum of Marcano *et al.*[15] (b) Overlaid C1s XPS spectra of our GO and the GO of Marcano *et al.*, showing the similarity between the composition of the two materials. (c) Deconvoluted C1s XPS spectrum of Cao *et al.*[16] (d) Overlaid C1s XPS spectra of our GO and the GO of Cao *et al.* showing the clear difference between the composition of the two materials. The data by Marcano *et al.* was obtained from the authors, and the data by Cao *et al.* was digitized from the published article.

We deconvoluted the raw data of the C1s XPS spectrum reported by Marcano *et al.*,[15] and obtained an oxidation level of ~69%, in good agreement with their previously reported value and the functionalization level of our GO. Similar to our sample, the oxidized carbons consist mainly of epoxides (C-O, 57.4%). Overlaying the C1s XPS spectra of our GO and the GO made by Marcano *et al.*[15] further highlights the similarity between the two materials (Figure 2.8b). These results confirm that the composition of our material closely matches with previous studies. Marcano *et al.* also characterized their sample with solid-state nuclear magnetic resonance (ssNMR) spectroscopy and found that the epoxide peak was more intense than the hydroxyl peak, suggesting that epoxide groups are the predominant functional group. This validates the XPS results and given that the composition of our material is very similar to the GO characterized by Marcano *et al.* (based on XPS data), this suggests that our GO is indeed epoxide-rich.

We analyzed the digitized C1s XPS spectrum from Cao *et al.*[16], as we were unable to obtain original data from the authors. The published spectrum was digitized using ImageJ and imported into the Avantage software that we used to analyze our data. Deconvolution yielded an oxidation level of ~70%, which is similar to their reported value of 71.4%. The functional group distribution we obtained differs (Table 2.2) from what was reported by Cao *et al.* presumably because we fit the epoxide and hydroxyl peaks separately. Nevertheless, we found the percentage of epoxide groups (11.3%) to be significantly lower than that of our GO. In their spectrum, it is evident that the intensity of the peak corresponding to oxidized carbons is much lower than the intensity of the peak corresponding to graphitic carbons (the opposite is true for our GO) (Figure 2.8d). This clearly shows that the composition and functional group distribution of their GO is very different from that of our GO, suggesting that the difference in measured mechanical properties originates from variations in chemical structure between the two materials, as noted in Section 2.2.4.

Importantly, this analysis provides further evidence that an epoxide-rich composition is necessary for plasticity to be observed in GO single-layers.

Table 2.2 Tabulated XPS peak locations and intensities for GO from previous studies.[15,16]

Marcano *et al.* (GO)[15]		
	BE (eV)	Relative Area
C-C	284.46	30.5%
C-OH	285.90	1.7%
C-O	286.52	57.4%
C=O	287.88	10.1%
C(O)O	289.42	0.3%

Cao *et al.* (GO)[16]		
	BE (eV)	Relative Area
C-C	284.46	69.8%
C-OH	285.90	4.8%
C-O	286.52	11.3%
C=O	287.88	13.7%
C(O)O	289.42	0.5%

2.4.7 Fabrication of Si Substrates with Microwells *(This work was carried out by Dr. Fan Zhou)*

Si substrates containing arrays of microwells with 1.76 μm diameter and 4 μm depth were fabricated using a combination of photolithography and deep reactive-ion etching (DRIE). A 1.2-μm-thick photoresist layer (S1813 positive photoresist manufactured by Dow Electronic Materials Microposit, catalog number DEM-10018348, distributed by Capitol Scientific Inc., Austin, TX) was spin-coated onto the Si wafer at 4,000 rpm using a Cee 200X spin coater (Brewer Science Inc., Rolla, MO). Following a 1 min soft bake at 100 °C on a hot plate, the wafer was exposed to ultraviolet light (365 nm, 18 mW cm^{-2}) for 4 s on a Suss MABA6 Mask Aligner instrument (SÜSS MicroTec AG, Garching, Germany). After exposure, the wafer was developed in a MF 319 developer (manufactured by Dow Electronic Materials Microposit, catalog number: DEM-10018042, Capitol Scientific, Inc, Austin, TX) for 60 s. Spin rinsing was carried out with ultrapure deionized water (200 mL) for 30 s at ~300 rpm, followed by a 60 s spin dry at 3,000 r.p.m.

The resulting photoresist-masked silicon wafer was then subjected to microwell etching using a STS LpX Pegasus DRIE machine (SPTS Technologies Ltd., San Jose, CA). After etching, the remaining photoresist was removed using acetone, and the wafer was cleaned using isopropanol and ultrapure deionized water. This wafer was then cleaved into smaller substrates to be used in the Langmuir–Blodgett deposition and subsequent membrane deflection experiments.

2.4.8 Preparation of Substrates for Langmuir-Blodgett Deposition

Prior to Langmuir–Blodgett deposition, the substrates were cleaned using the following procedure: (1) submerged in 2 mL of a 3:1 v/v mixture of concentrated H_2SO_4:30 wt % H_2O_2 and heated in a Biotage SPX microwave reactor (Biotage Inc., Uppsala, Sweden, software version 2.3, build 6250) at 180 °C for 45 min, (2) sonicated for 10 min each in ultrapure deionized water (~10 mL), methanol (~10 mL), and ultrapure deionized water (~10 mL), respectively, (3) dried under a flow of nitrogen for 1 min, and (4) treated with O_2 plasma (5 min at 190 W and 10-15 mTorr O_2) in a Model PC-2000 plasma cleaner (South Bay Technology Inc., San Clemente, CA). After this cleaning process, the substrates were left under ambient conditions and their water contact angles were monitored until the desired values were reached (~30°, 60° or 90° after 3 hours, 2 days, and 1 week, respectively; Figure 2.9) before Langmuir–Blodgett deposition (see procedure below). The water contact angle of the freshly plasma-treated substrates was ~0°, gradually increasing over time and reaching a maximum of ~95° one week after plasma treatment.

The yield of intact suspended GO membranes is found to be strongly dependent on the water contact angle of the substrate (Figure 2.9). SEM images show that substrates with a contact angle of < 60° resulted in ruptured membranes, while substrates with a contact angle of ~60–95° yielded intact membranes. Suspended membranes that were deposited on substrates with lower water contact angle (*i.e.,i.e.,* recently plasma-cleaned) tend to rupture frequently during the drying process presumably due to the capillary pressure and surface tension of water trapped in the wells during Langmuir–Blodgett deposition, which exerts a downward force on the membrane.[35,36] Substrates with higher water contact angles (*i.e.,i.e.,* more hydrophobic surfaces) may reduce this effect and prevent membrane rupture.

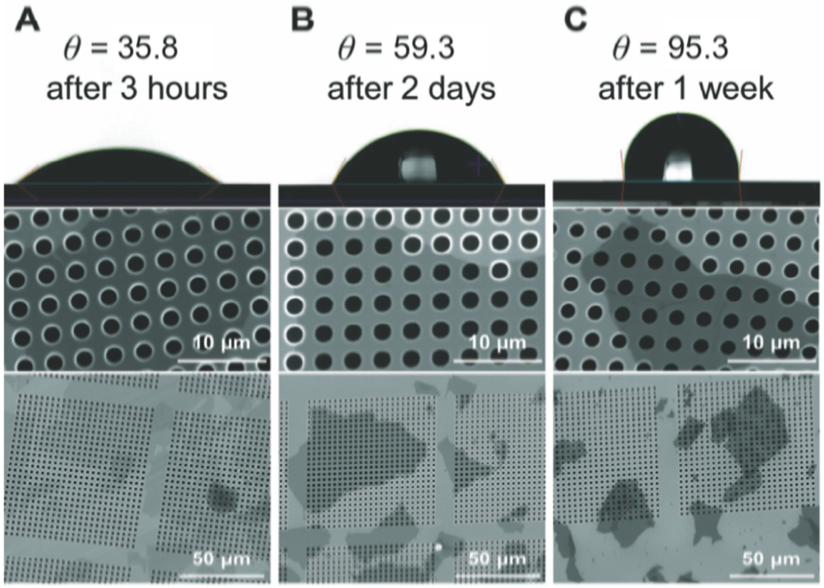

Figure 2.9 Top row: Water contact angles of bare Si substrates at various times after substrate cleaning. Middle and bottom rows: SEM images of GO monolayers deposited on the same substrates with the water contact angles shown above. Wells that contain a ruptured membrane have bright edges due to the edge effect, while those that contain intact membranes have dark edges. (a) Deposition on a substrate with < 60° water contact angle results in ruptured membranes. (b) Deposition on a substrate with an optimal water contact angle of ~ 60° yields intact membranes. (c) Deposition on a substrate with > 60° water contact angle yields a lower coverage of intact but wrinkled membranes, presumably due to the hydrophobic nature of the substrate surface.

2.4.9 Langmuir–Blodgett Assembly of GO Monolayers

To prepare suspended GO monolayers for the AFM membrane deflection experiments, the Langmuir–Blodgett assembly method was employed.[17] The as-prepared aqueous GO dispersion was diluted with MeOH to a mixture of 5:1 v/v MeOH:GO dispersion. The Nima model 116 trough (Nima Technologies, Ltd., Espoo, Finland) was cleaned with acetone and filled with ultrapure deionized water. Generally, GO solution (300–480 μL) was spread onto the water surface dropwise at a rate of 100 μL min^{-1} using a glass syringe, forming a monolayer film on the surface. The surface pressure was monitored using a tensiometer attached to a Wilhelmy plate. The film was allowed to equilibrate for at least 20 min after spreading, and then compressed by barriers at a speed of 100 $\text{cm}^2\ \text{min}^{-1}$. The GO monolayer was transferred near the onset of the surface pressure increase (Figure 2.10) by vertically dipping the substrate into the trough and slowly pulling it up at a rate of 2 mm min^{-1}.

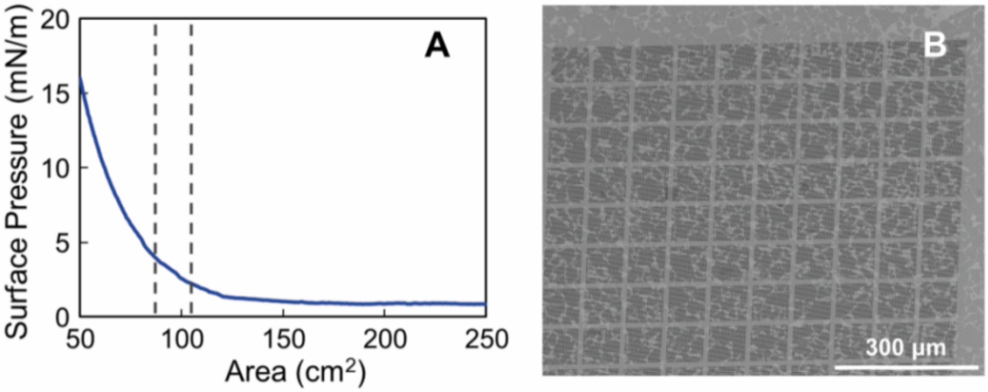

Figure 2.10 (a) Typical surface pressure/area isotherm obtained during the LB deposition of GO monolayers. (b) Close-packed monolayers were obtained by depositing near the onset of surface pressure increase (the region indicated by the dashed lines in (a)).

2.4.10 Atomic Force Microscopy Membrane Deflection Tests *(This work was carried out by Dr. Xiaoding Wei)*

A single-crystal diamond probe (catalog number: ART D160, K-TEK Nanotechnology, Wilsonville, OR) was used to indent at the membrane centre with an AFM (Dimension 3100, Veeco Instruments Inc., Plainview, NY) as shown in Figure 2.11a. The stiffness of the cantilever (k = 3.18 N m^{-1}) was calibrated using a standard cantilever (CLFC-NOBO, Bruker Inc., Billerica

MA).[18] The tip radius of the AFM probe (R = 25 nm) was measured by an FEI NovaNano 600 SEM (FEI Co., Hillsboro, OR) as shown in Figure 2.11b. All experiments were performed at room temperature and 16% humidity inside a customized environmental chamber. A constant deflection rate of 1 μm s^{-1} was used in all tests.

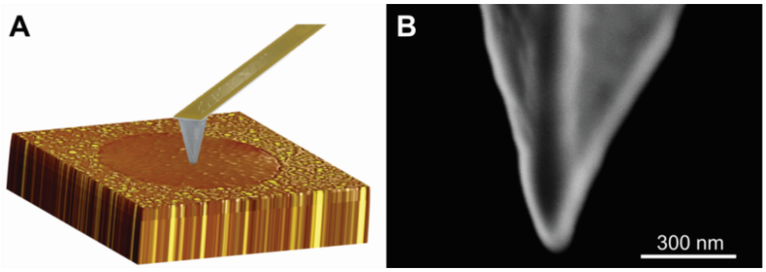

Figure 2.11 (a) Schematic of AFM membrane deflection test on a suspended circular GO membrane. (b) Scanning electron micrograph of the AFM tip.

For a suspended circular linear elastic membrane under a central load, the force versus deflection response can be approximated as[18]

$$F = \pi\sigma_0 h\delta + \frac{Eh}{q^3 a^2}\delta^3 \qquad 2.2$$

where F is the applied force, δ is the membrane centre deflection, h is the effective thickness of the monolayer GO membrane (taken as 0.75 nm),[27] σ_0 is the pre-stress in the membrane, a is the membrane diameter, E is the elastic modulus and v is the Poisson's ratio. According to DFTB calculation results (Figure 2.15), the Poisson's ratio of the GO studied here was taken as 0.2 (Table 2.4).

2.4.11 Analysis of AFM Membrane Deflection Test Results *(This work was carried out by Dr. Xiaoding Wei)*

By fitting the force vs. deflection response with Equation 2.2, while keeping σ_0 and E as two free variables, both the pre-stress and elastic modulus were determined. For all tests, the experimental curves were only fitted up to the plastic onset points. To avoid artifacts, the plastic onset point was determined as the data point beyond which the least-squares fitting using Equation 2.2 produces an R^2 value lower than 0.999. Elastic analysis results for GO and A-GO samples are compared in Figure 2.12.

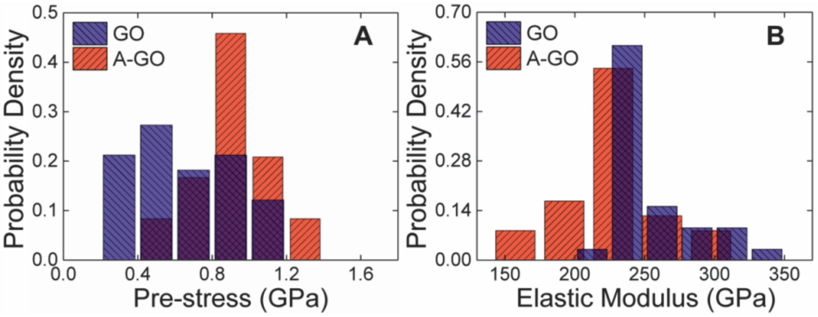

Figure 2.12 Histograms of pre-stress (a) and elastic modulus values (b) derived for GO and A-GO membranes.

The two-parameter Weibull probability distribution function is expressed as:

$$P = 1 - \exp\left[-\left(S / S_0\right)^m\right] \tag{2.3}$$

where P is the probability of material damage or failure for the material subjected to a quantity S, S_0 is the scale factor for the corresponding quantity, and m is the shape factor (or Weibull modulus) that determines the breadth of the probability distribution. A small m means a wide variation in the analyzed quantity that implies a broad range of defects in the material. A large m means either that the material failure is insensitive to the presence of defects or that there is a narrow range of defects in the material. In this study, the quantities of interest in Equation 2.3 are activation stress and breaking force.

Figure 2.13a and b show the distributions of activation stress and breaking force for GO and A-GO. As discussed previously, both GO and A-GO specimens exhibited ductile and brittle types of force vs. deflection curves but with different statistical distributions. All GO samples except for one showed ductile failure, presumably due to the plasticity that originated from the epoxide-to-ether group transformation as discussed above. In contrast, a significant portion (~ 44%) of the A-GO specimens failed in a brittle way, indicating the presence of a different failure mechanism. Indeed, the bi-modal distribution of the A-GO activation stress values (Figure 2.13a) suggests that Weibull analysis should be carried out on the data sets of A-GO for each failure mode to evaluate the different mechanisms. As such, individual Weibull analysis was carried out separately on the two classes of A-GO specimens that exhibited ductile and brittle modes of failure (Table 2.3).

Weibull analysis of the activation stress of ten ductile A-GO membranes yields a scale factor of 6.3 GPa (shape factor = 12.9), lower than that for the eight brittle A-GO membranes (scale factor = 8.4 GPa, shape factor = 9.7) (Figure 2.13 and Table 2.3). Both of these values are higher than the activation stress of all GO membranes (scale factor = 5.4 GPa, shape factor = 8.3). Weibull analysis of the breaking force values (Figure 2.13d) yields a similar trend: The scale factor for the ten ductile A-GO membranes (63.5 nN, shape factor = 4.9) is lower than that for the eight brittle A-GO membranes (77.2 nN, shape factor = 11.8) but higher than that for all GO membranes (scale factor = 51.8 nN, shape factor = 4.1). Interestingly, the shape factor of the breaking force for the ductile A-GO is very close to that for all GO membranes, suggesting the same failure mechanism governs both materials. The larger scale factors of the Weibull analyses of the breaking forces for both ductile and brittle A-GO specimens, compared to that for the GO membranes, suggest that A-GO has gained much-improved mechanical strength with only a partial loss of plasticity. However, the shape factors of the Weibull analyses of the breaking forces for both GO and A-GO are still significantly lower than that for pristine graphene (~16),[18] indicating failure is highly affected by imperfect lattices and inherent voids in the materials.

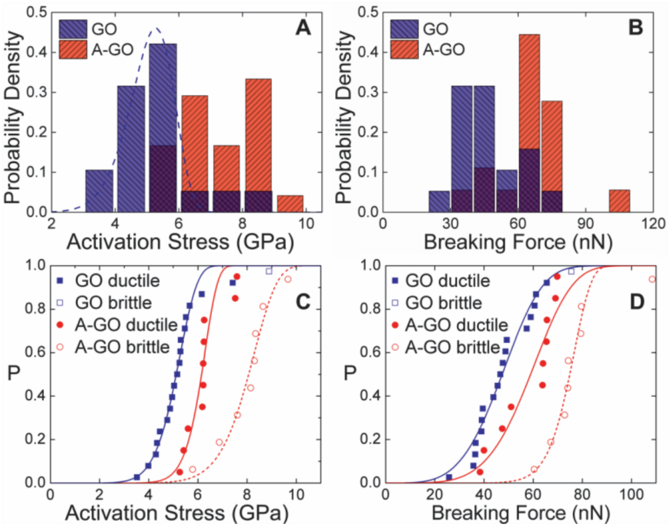

Figure 2.13 (a) Histograms of activation stress values of GO and A-GO monolayers. Dashed line indicates the fitted Weibull distribution for GO. (b) Histograms of the breaking force of GO and A-GO. Weibull analysis of activation stress (c) and breaking force values (d) for GO and A-GO specimens that showed ductile (solid circles) and brittle (open circles) failure, respectively.

Table 2.3 Weibull analysis results for GO and A-GO activation stresses and breaking forces.

		Activation Stress		Breaking Force	
		Scale Factor (GPa)	Shape Factor	Scale Factor (nN)	Shape Factor
GO	Total	5.4	8.3	51.8	4.1
	Ductile	5.4	8.3	51.8	4.1
	Brittle	N/A	N/A	N/A	N/A
A-GO	Total	7.5	5.4	70.7	6.8
	Ductile	6.3	12.9	63.5	4.9
	Brittle	8.4	9.7	77.2	11.8

2.4.12 Development of GO Molecular Models *(This work was carried out by Rafael A. Soler-Crespo)*

The configurations of functional groups in GO have great impacts on the modelling results, as discussed in previous literature.[3,20,22,23,37,38] Thus, having physically meaningful GO models that can represent the behavior of realistic GO sheets is important. In our work, the generation of models was carried out using a modified version of the algorithm developed by Paci *et al.*[12] While thermodynamics favors the formation of low-energy structures over those of high energies in chemical transformations, the strongly oxidative conditions involved in the synthesis of GO are more conducive for functional groups to form stochastically (that is, kinetically driven) regardless of the relative energy associated with different oxidation pathways. In light of this, a configurational-bias Monte Carlo algorithm was modified to introduce a range of functional groups on a graphene sheet to account for both thermodynamically and kinetically driven oxidation processes.[12] The implemented algorithm comprises the following:

(1) A graphene sheet was generated with dimensions 1.988 × 2.091 nm^2.

(2) Atoms were added in two alternating steps through a Monte Carlo addition scheme that considered all possible functionalization sites. In the first step, N independent and partially oxidized sheets were generated by adding two hydroxyl and four epoxide groups (one-half to each side of each sheet). Epoxide oxygen atoms were placed at a vertical distance of 1.24 Å with respect to the graphene basal planes, and at the midpoints of the lines joining two adjacent carbon atoms. Initially, hydroxyl oxygen atoms were placed at a vertical distance of 1.43 Å over carbon atoms, and associated hydrogen atoms were placed at a vertical distance of 0.95 Å over those oxygen atoms. The final, optimal C–O–H bond angles were obtained after geometry optimization.

(3) Each of the N sheets was subjected to geometry optimization and stress relaxation using DFTB as implemented in CP2K (http://www.cp2k.org/). This technique generates stress-free initial structures and represents the most significant modification of the algorithm proposed by Paci *et al.*[12] Structures obtained by geometry optimization alone were found to contain compressive stresses on the order of 3 GPa, which could bias optimization results, leading to inaccurate system minima. (4) For each of the N sheets, the Rosenbluth factor was calculated as given by:

$$p_j = \frac{\exp(-\beta E_j)}{\sum_{i=1}^{N} \exp(-\beta E_i)} \tag{2.4}$$

where

$$\beta = \frac{1}{k_B T_{art}} \tag{2.5}$$

Here p_j is the probability of observing the jth sheet naturally, E_j is the minimized energy of the jth sheet, E_i corresponds to an energy sum over all the N generated GO models, k_B is Boltzmann's constant and T_{art} represents an artificial temperature value utilized to weight the effect of temperature in minima selection. This method, known as Rosenbluth sampling, is akin to Boltzmann distributions in statistical mechanics. The artificial temperature, T_{art}, was chosen to be 300 K, the temperature at which membrane deflection experiments in this study were carried out. The Rosenbluth factor for each of the N sheets was compared with a random number in the range [0, 1]. This process resulted in the selection of M structures ($M < N$) to be further oxidized, and allowed structures with relatively high energies to exist while biased for the selection of structures with relatively low energies.[12]

(5) Four additional epoxide groups were added (one-half to each side of the sheet), resulting in *N* independent sheets from each of the *M* structures. Then, geometry optimization and stress relaxation were carried out on each of the *MN* sheets and the Rosenbluth factor was calculated.

(6) GO sheets with various functionalization levels, φ = 0, 0.1, 0.2, 0.36, 0.7 and 0.9, were generated by repeating steps 2–5.

This approach means the GO models generated in this study are disordered and energetically favorable (Figure 2.14 and Section 2.4.13). All models were oxidized to a 4:1 epoxide/hydroxyl functional group ratio, based on the relative chemical composition suggested by XPS (Table 2.1). As an oxygen atom is covalently bound to two carbon atoms in an epoxide group and to one carbon atom in a hydroxyl group, the fraction of oxidized carbon atoms, φ, for each GO model is defined as:

$$\varphi = \frac{N_{Carbon,oxidized}}{N_{Carbon,total}} = \frac{2N_{Oxygen} - N_{Hydrogen}}{N_{Carbon}} \qquad 2.6$$

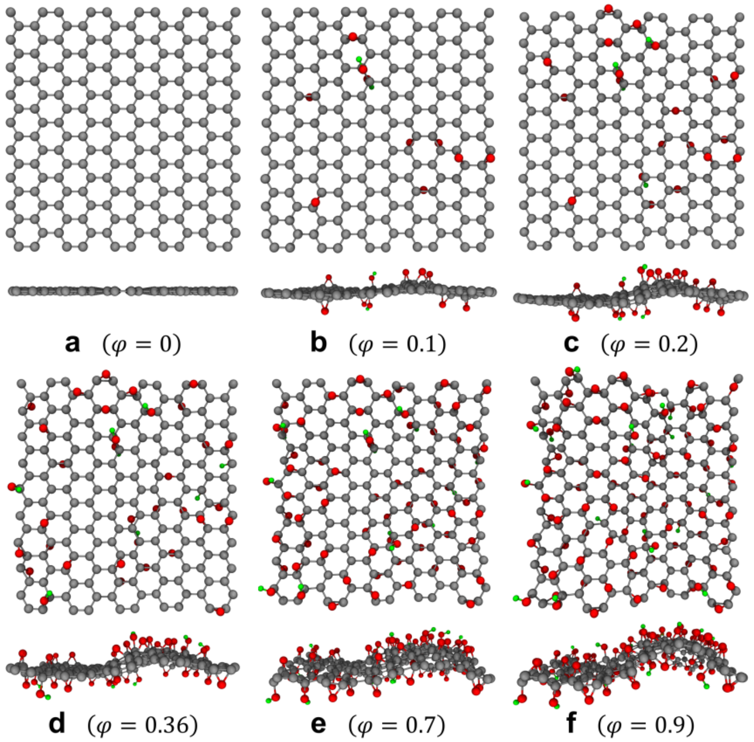

Figure 2.14 (a) Graphene (with 0% oxygen coverage, *i.e.,i.e.,* φ = 0). (b-f) GO with 10 (φ = 0.1, (b)), 20 (φ = 0.2, (c)), 36 (φ = 0.36, (d)), 70 (φ = 0.7, (e)), and 90 (φ = 0.9, (f)) % oxygen coverage. Gray, red, and green beads represent carbon, oxygen, and hydrogen atoms, respectively.

2.4.13 Validation of GO Model Generation Algorithm

Figure 2.14 shows snapshots of the top and side views for the six models generated in this study. Models with φ = 0, 0.1, 0.2, 0.36, 0.7, and 0.9 were generated to represent a range of oxidation levels potentially attainable in GO sheets. Specifically, the model with 70% oxygen coverage is consistent with the analysis reported by Marcano *et al.* (69% oxidized C).[15] After the sheets were geometry- optimized, and the residual stresses eliminated, the microstructures of the models were quite comparable to the Lerf-Klinowski model of GO,[6] where hydroxyl and epoxides were the dominant functionalities. The placement and directionality of functional groups in our model is consistent with various reports in the literature.[20,22,23,37,38] Specifically, we capture two reported observations. First, hydroxyl groups that appear on the same side of the basal plane are para-positioned (*i.e.,i.e.,* on the opposite sides of the same hexagonal ring). On the other hand, hydroxyl groups on opposite sides of the basal plane are either meta- or ortho-positioned (*i.e.,i.e.,* the second hydroxyl group is present in any of the carbon atoms that is not opposite to that bearing the first hydroxyl group). For φ ≥ 0.70, a small number of carbonyl, oxetane, and ether groups were also observed, consistent with the reports of Erickson *et al.*[3] Also, we note that while Erickson *et al.* found evidence for the formation of islands of functional groups in sheets with φ ≈ 0.80, we did not include this "islanding" phenomenon in our models, as the scale on which this is thought to occur is too large to be captured by our calculations.[3] Second, we observe that sheet waviness increases in our models with increasing oxygen coverage, as reported in experiments and computations.[39-42]

2.4.14 Molecular Mechanics Simulation Methodology *(This work was carried out by Rafael A. Soler-Crespo)*

MM simulations were carried out using DFTB, a semi-empirical quantum-mechanical method.[43] This approach was chosen to balance computational efficiency and accuracy, and its performance has been demonstrated to be superior to that of classical force fields.[12,43] The *mio-0-1* Slater–Koster parameter set and charge self-consistency were used.[44] Charges were treated using a smooth particle-mesh Ewald summation scheme, with one grid point per Å. The Ewald convergence parameter was set to 0.35, and a cutoff radius of 10 Å for the real-space forces was used. Stresses were obtained using the virial theorem. Three types of tensile tests were carried out on graphene and GO under displacement control conditions: (i) uniaxial strain tension in the armchair direction (that is, tension was applied in the armchair direction with the boundaries in the zigzag direction fixed), (ii) uniaxial strain tension in the zigzag direction (that is, tension was applied in the zigzag direction with the boundaries in the armchair direction fixed), and (iii) equibiaxial tensile strain. Displacements of the unit-cell boundaries of the tensile direction were described according to 0.5% strain increments. Geometry optimization was carried out between each increment. Mechanical properties were extracted from MM simulations using continuum mechanics approximations for isotropic, linear elastic materials at low strains (Section 2.4.16, Table 2.4, and Figure 2.16). The results show good agreement with the experimental measurements summarized in Figure 2.13 (for a detailed discussion, please see Section 2.4.16).

2.4.15 Molecular Dynamics Simulation Methodology *(This work was carried out by Rafael A. Soler-Crespo)*

Molecular dynamics simulations were carried out based on DFTB forces. A 0.5-fs time step and the microcanonical ensemble were used. Temperature was maintained at 300 K with a Nose–Hoover thermostat and a thermostat relaxation time constant of 25 fs. One picosecond of dynamics was performed between each strain increment. Tensile strains were applied using the same procedure outlined in the molecular mechanics simulation methodology. The only molecular dynamics simulations carried out in this report correspond to equibiaxial tensile strain for the GO sheet with $\varphi = 0.7$, which is representative of the material in this study. The analysis used for MM simulations was applied to extract mechanical properties from MD simulations.

2.4.16 Interpretation of Simulation Results

Figure 2.15 shows a summary of the computational results obtained from MM simulations for the GO models with different oxygen coverages generated in this study. First, we were interested in extracting linear elastic properties, which can be estimated from knowledge of material elastic constants.[28] If a material is isotropic linear elastic, the following relationships hold:

$$E = \frac{C_{11}^2 - C_{12}^2}{C_{11}} \qquad 2.7$$

$$\nu = \frac{C_{12}}{C_{11}} \qquad 2.8$$

where E is the elastic modulus of the system, ν is the Poisson's ratio of the system and C_{11} and C_{12} are elastic constants.

From the uniaxial strain tension results in the armchair direction (Figure 2.15a,b), a set of elastic constants, C_{11} and C_{12}, can be determined through least- squares fitting the stress-strain curves at small strains. By applying the same procedure on the uniaxial strain tension results in the zigzag direction (Figure 2.15c and d), another set of C_{11} and C_{12} can be determined. The two sets of constants determine a set of elastic moduli (E_A and E_Z, subscripts A and Z represent values in the armchair and zigzag directions, respectively) and Poisson's ratios (ν_A and ν_Z), independently. The nonlinearity in the stress-strain curves at small strains (Figure 2.15a-d, especially for GO with $\varphi = 0.9$) arises mainly from increasing waviness intrinsic to the sheets due to their highly oxidized nature. To alleviate this artifact, the elastic constants of the material were determined by fitting the segments where the tangential slopes stabilized. Furthermore, stress-strain curves were shifted using the stabilized tangential slopes so that the linear extrapolation of the curves passed through the origin.

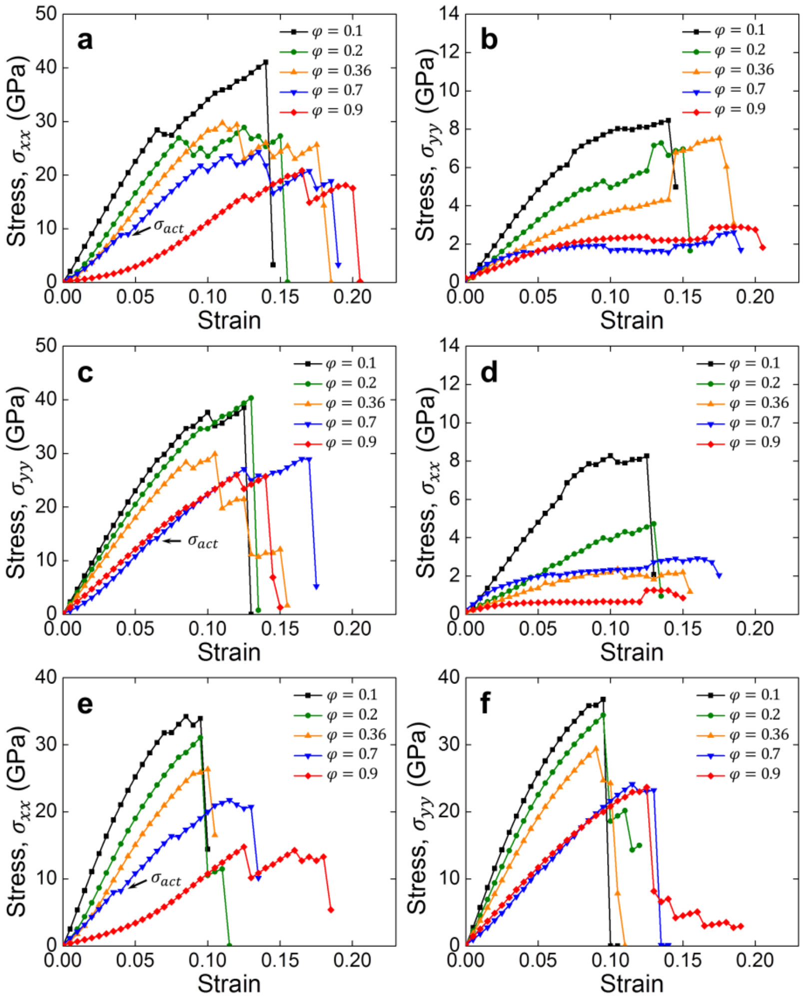

Figure 2.15 (a,b) Stress-strain curves along the armchair (a) and zigzag (b) directions during uniaxial strain tension along the armchair direction. (c,d) Stress-strain curves along the zigzag (c) and armchair (d) directions during uniaxial strain tension along the zigzag direction. (e,f) Stress-strain curves along the armchair (e) and zigzag (f) directions during equibiaxial tensile strain. Marked by arrows are the activation stresses when the first epoxide-to-ether transformation occurs in 70% functionalized GO under each constraint.

As shown in Table 2.4, the elastic modulus of GO decreases with increasing functionalization level due to the transition from stiff sp^2 bonds to sp^3 bonds. The elastic modulus in the zigzag direction is marginally greater than that in the armchair direction for most of the GO models. However, for the model with $\varphi = 0.7$, the elastic moduli derived for both directions are identical within numerical uncertainty. This justifies the isotropic linear elastic models used to analyze the experimental results (see Equation 2.1 and 2.2). We also find that the Poisson's ratio oscillates between 0.07 and 0.24, and does not show any trends in either the armchair or zigzag directions, possibly due to the stochastic directionality of epoxide groups added during model generation. The Poisson's ratio values for GO with $\varphi = 0.7$ are very close in both directions. Therefore, we chose $\nu = 0.2$ as the Poisson's ratio in Equation 2.2 for elastic analysis.

At large strains, the epoxide-to-ether group transformation was identified in the calculations on all GO models, as shown in Figure 2.15. The activation stress was obtained by inspecting the molecular trajectories of the model at individual strain steps to directly identify the first epoxide-to- ether transformation. The stress level applied at the strain step prior to the first observed transformation was defined as the activation stress. The activation stress first decreases with increasing oxygen coverage and reached a minimum at $\varphi = 0.7$. However, when the system becomes more oxidized ($\varphi = 0.9$), it increases. This result suggests that the epoxide-to-ether transformation activation is affected by not only epoxide group population, but also material heterogeneity. Beyond $\varphi = 0.70$, more oxidization leads to loss of heterogeneity so that the transformation activation becomes more difficult. As a consequence of epoxide-to-ether transformations, all GO models exhibited plasticity before failure. To compare plasticity between different models, plastic strains were extracted by defining plastic strain (ε^p) as the strain caused purely by epoxide-to-ether transformations. As shown in Table 2.4, the trend in plastic strain is opposite to that of the activation stress. The simultaneous minimum activation stress and maximum plastic strain at $\varphi = 0.70$ suggest that GO ductility is optimized at this specific chemical composition. Finally, the ultimate strength ($\sigma^{\max}$) monotonically decreases when φ increases as a result of more sp^3 bonds, which are weaker than sp^2 bonds. In summary, our calculations suggest that there is ample space for tuning the mechanical properties (*i.e.,i.e.,* elastic modulus, strength and ductility) of GO. Based on our results, the material studied in this report should possess optimal ductility.

Table 2.4 Mechanical properties derived from the MM calculations on graphene and GO with various φ. Uniaxial strain tension tests yielded the elastic modulus E, Poisson's ratio ν, maximum stress σ^{max}, and plastic strain ε^p (subscripts A and Z represent values in the armchair and zigzag directions, respectively). Additionally, σ^{act} is the activation stress in the armchair direction under equibiaxial tension. All values were calculated assuming a GO thickness of h = 0.75 nm for comparison. Values for graphene (in parentheses) assume h = 0.34 nm.

φ	E_A [GPa]	E_Z [GPa]	ν_A	ν_Z	$\sigma_A^{\max}$ [GPa]	σ^{act} [GPa]	$\sigma_Z^{\max}$ [GPa]	ε_A^p [%]
0	538.1 (1187.0)	541.6 (1194.8)	0.23	0.23	53.8 (118.6)	N/A	55.0 (121.3)	N/A
0.1	447.1	458.7	0.22	0.21	41.1	31.8	38.5	1.0
0.2	377.4	421.2	0.17	0.09	28.9	31.1	40.3	2.0
0.36	331.6	368.1	0.13	0.10	29.7	25.7	29.9	2.5
0.7	257.6	257.3	0.22	0.24	24.3	8.0	29.0	3.5
0.9	191.6	247.1	0.17	0.07	20.9	14.8	26.0	1.0

To provide further insight into the epoxide-to-ether transformation mechanism, we extracted the local C-C bond strain information in the 70% functionalized GO model before and after the first transformation. As shown in Figure 2.16, there is a highly localized tensile strain in the C-C bond of the epoxide group prior to its transformation (Figure 2.16a). In contrast, the C-O bonds in that epoxide ring undergo much less strain. This demonstrates why the C-C bond breaks instead of the C-O bonds when an epoxide group in GO is subjected to a critical in-plane mechanical load. After the transformation (Figure 2.16b), a significant strain relaxation was observed in the same location. This local C-C bond strain analysis provides further insight into how the transformation mechanism helps arrest the nano-cracks in GO and affords the material enhanced toughness as discussed previously.

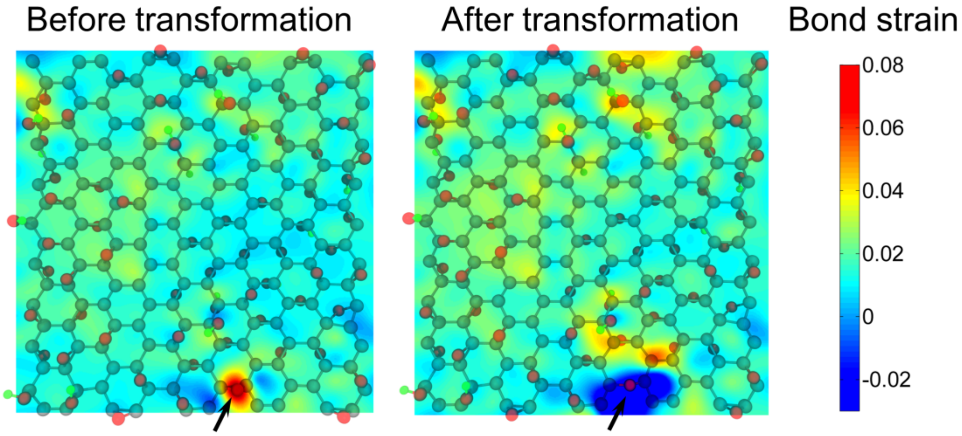

Figure 2.16 Local C-C bond strain fields for GO with φ = 0.70 before (a) and after (b) the first epoxide-to-ether transformation. Arrows highlight the location where the first epoxide-to-ether transformation occurs. Gray, red, and green beads represent carbon, oxygen, and hydrogen atoms, respectively.

Chapter 3

Enhancing the Toughness of Single-Layer GO Through Hydrogen-Bonding Interfacial Interactions

Portions of this chapter may appear in the following manuscript:

Soler-Crespo, R. A.;[†] Mao, L.;[†]; Wen, J.; Nguyen, H. T.; Zhang, X.; Wei, X.; Miller, D. J.; Huang, J.; Nguyen, S. T.; Espinosa, H. D. Atomically thin polymer layer optimizes toughness of graphene oxide monolayers. *Manuscript to be submitted.*

[†] Equal contribution

3.1 Introduction

As discussed in Chapter 1, extensive interfacial interactions between hard (stiff) and soft (ductile) components is one of the key design principles that enables the length-scale extension of mechanical properties in nacre. Successful application of this design concept to carbon nanomaterial-based composites requires an understanding of the nanoscale mechanisms by which interfacial interactions enhance mechanical performance. Direct correlation between interfacial interactions and mechanical properties can be achieved in a nanoscale composite system comprising a single interface; specifically, single-layer GO modified with an ultrathin layer of a soft material.

In Chapter 2, we showed that epoxide groups engender GO with damage tolerance by transforming into ether groups, and effectively bridging nanoscale cracks within the basal plane of the sheet. This motivates the use of a longer, ductile bridging moiety to connect larger areas of the GO sheet through interfacial interactions, thereby bridging cracks at longer length scales and increasing the damage tolerance of GO. In this way, the GO can bear more mechanical load before failing, thus increasing its toughness. To maximize the crack-bridging ability, the bridging moiety must be capable of extensive interfacial interactions with GO. As such, we selected polyvinyl alcohol (PVA), which is known to form extensive hydrogen bonds with the oxygenated groups of GO.[1,2] We envisioned that a hydrogen bond-mediated polymer network would form on the GO surface and bridge oxidized domains, provided that the contour length of the polymer chains is comparable in size to two or more oxidized domains.

In this chapter, we show that the addition of an ultrathin PVA layer significantly enhances the fracture toughness of GO nanosheets through polymer chain-mediated crack-bridging at the microscale (100 nm to 1 μm), leading to a three-fold increase in the load-bearing capacity of GO.

Nanoscale characterization of these GO-PVA nanolaminates strongly suggests that the origin of this toughening is an extended, nanostructured hydrogen-bonding network on the surface of GO. The key role of reformable hydrogen bonds between GO and PVA, in enhancing fracture toughness and failure resistance of GO, is revealed by a detailed fracture mechanics model guided by atomistic molecular dynamics (MD) calculations. Through this approach, we identify the "microscale" version of a typically macroscopic mechanism in which nanoconfined polymers delay load localization and fracture,[3-7] and demonstrate how interfacial interactions between GO and a soft material can be leveraged to enhance the toughness of GO. Together, our results suggest that GO-polymer nanolaminates can serve as effective constituents in macroscopic GO-based composites, and highlight the importance of tailoring the interfacial chemistry of nanoscale constituents to maximize mechanical properties.

3.2 Results and Discussion

3.2.1 Study Overview

Testing of freestanding GO-PVA nanolaminates with an overall thickness of ~2 nm requires a method that can resolve nanometer displacements and µN forces. To accomplish this, we employed atomic force microscopy (AFM) membrane deflection experiments. GO nanosheets modified with a ~1.5 nm thick layer of PVA (total thickness of 2.5 nm) were fabricated by sequential Langmuir-Blodgett (LB) deposition of GO[8] and PVA onto a patterned Si substrate (Figure 3.1a and Section 3.4.4). Prior to nanomechanical testing, the formation of a nanostructured PVA network on GO was confirmed through high-resolution transmission electron microscopy (HRTEM) techniques (Figure 3.2), and the polymer microstructure was studied via AFM characterization (Figure 3.1b). Notably, the load-deflection behavior of GO-PVA nanolaminates revealed a three-fold increase in load-bearing capacity, as compared to unmodified

GO single-layers, accompanied by permanent deformation and bulging of polymer in the region where the membranes were loaded (Figure 3.3). Such deformation and bulging suggests the existence of a toughening mechanism, schematically shown in Figure 3.1c, and later identified as crack bridging. The atomistic basis of this crack-bridging mechanism in GO-PVA was revealed through molecular and continuum modeling techniques (Figure 3.4), in which reformable hydrogen-bonding interactions between GO and PVA chains lead to effective interfacial load transfer, resulting in a significant increase of GO's load bearing capacity.

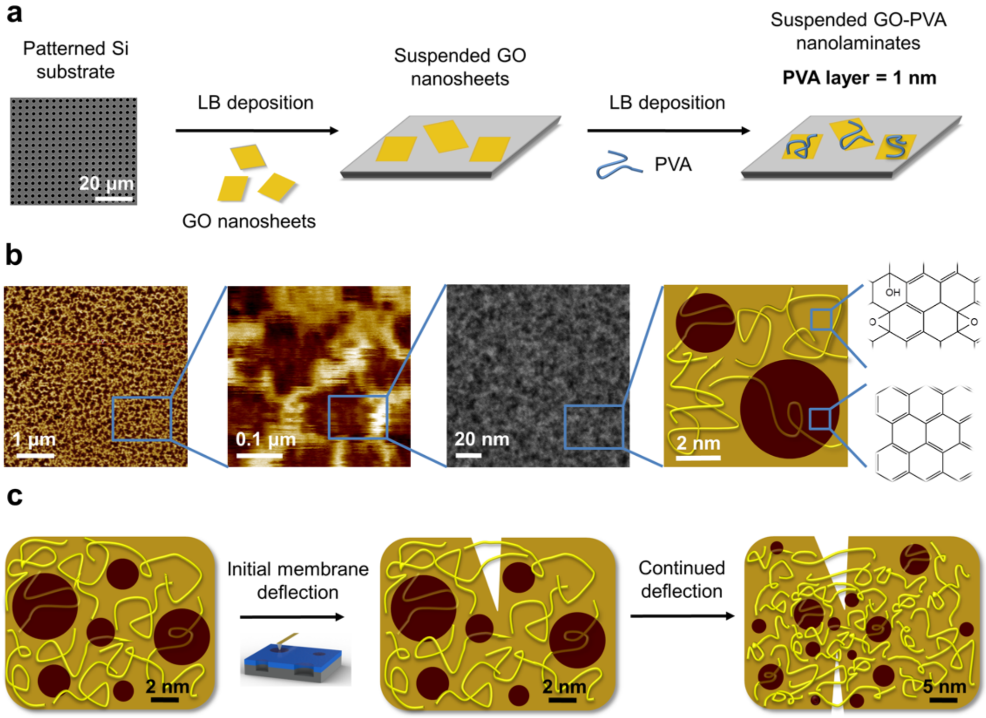

Figure 3.1 (a) Langmuir-Blodgett (LB) fabrication of suspended GO-PVA nanolaminates. (b) Hierarchical structure of GO-PVA nanolaminates. The AFM images in the first two panels show the microscale structure, and the STEM image in the third panel shows the nanoscale structure. The proposed molecular structure based on HRTEM and EELS characterization is shown as a schematic in the fourth panel. (c) Schematic of microscale crack-bridging in GO-PVA nanolaminates during AFM membrane deflection experiments. In b) and c), brown and gold represent graphitic and oxidized domains, respectively, while yellow denotes PVA chains.

3.2.2 Nanoscale Structure of GO-PVA Nanolaminates

The structure of GO comprises graphitic domains (~3-6 nm^2) interspersed within a continuous network of oxidized domains.[9] Hence, we hypothesized that PVA chains used in this study (~130 repeat units and ~34 nm contour length) can suitably interact with and bridge across multiple GO oxidized domains. In contrast, longer PVA chains would be unable to effectively bridge the oxidized domains, as they would preferentially form polymer-polymer hydrogen bonds, resulting in PVA aggregates on the GO sheet that interact minimally with the oxidized domains. AFM images of the nanolaminates fabricated using longer PVA chains confirmed that this is indeed the case, as this results in aggregation of PVA molecules on the GO surface (Section 3.4.5). The nanoscale structure of the investigated GO-PVA nanolaminates is revealed by HRTEM (see discussion below) and is not readily distinguishable from that of GO in both this work and previous literature,[9] since both PVA and the oxidized GO domains are amorphous (Figure 3.2a,b). To overcome this limitation, we employed electron energy loss spectroscopy (EELS), a spectroscopic technique that is sensitive to differences in local chemical composition, to elucidate the structure of GO-PVA nanolaminates.

The close association of PVA chains with the oxidized domains of GO was verified by analyzing the plasmon peak position in the low loss region of the EELS spectra. We utilized EELS in TEM mode to characterize a series of reference samples to establish peak positions for the graphitic, oxidized, and PVA-covered regions present in GO-PVA nanolaminates (Section 3.4.6). The locations of PVA adsorption with respect to the oxidized and graphitic domains of GO were then determined through an EELS line scan in scanning transmission electron microscopy (STEM) mode, given the finer lateral resolution of STEM (in our experiments, ~0.25 nm spot size, compared to a 500 nm region in TEM). In the high-angle annular dark-field (HAADF) image of the GO-PVA nanolaminate (Figure 3.2c), an EELS line scan across regions of varying z-contrast revealed changes in chemical composition. As the line scan moves from the low-z-contrast region to the high-z-contrast region, across a distance of 10 nm, the $\pi + \sigma$ plasmon peak in the corresponding EELS low-loss spectra shifts from 15 (low-z-contrast) to 17 eV (moderate-z-contrast), and then to 21 eV (high-z-contrast) (Figure 3.2d). These values correspond to the $\pi + \sigma$ peak positions for graphitic, oxidized, and GO-PVA domains, respectively. In addition, subtracting the EELS low-loss spectrum corresponding to the oxidized domain of GO, from the spectrum of GO-PVA, provides the spectral contribution from pure PVA, a peak at 23 eV (Figure 3.2d). These data suggest that PVA is mostly present on the oxidized domains of the GO sheet (*i.e.,i.e.,* the high-z-contrast areas) and confirms the hypothesis that hydrogen-bonding interactions lead to the formation of a nanostructured PVA network on the oxidized domains, which extends over the entire surface of GO (Sections 3.4.6 and 3.4.7).

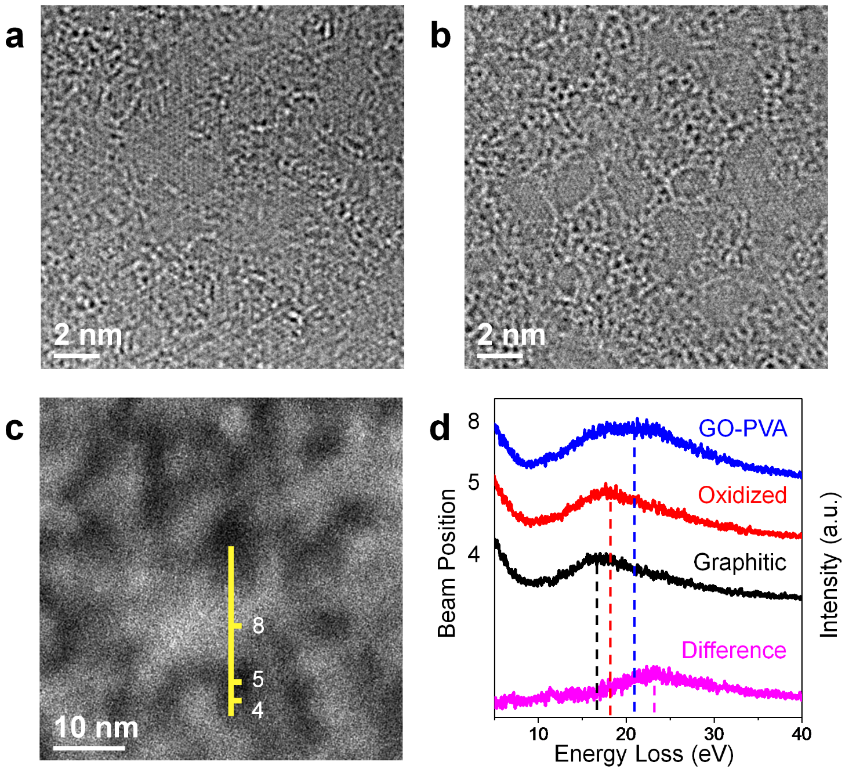

Figure 3.2 (a) HRTEM image of GO. (b) HRTEM image of GO-PVA nanolaminate. (c) EELS line scan across HAADF-STEM image of GO-PVA nanolaminate. The yellow line represents the line scan pathway, with the numbers corresponding to the beam position at individual points along the line scan. (d) EELS spectra corresponding to the line scan in (c). Taking the difference between the spectra of GO-PVA and oxidized GO yields the spectra contribution from PVA, a peak located at 23 eV.

Interestingly, atomic force microscopy (AFM) imaging of the GO-PVA nanolaminates reveals a much larger microscale pattern of interconnected PVA-dense regions (~20-150 nm in size), consistent with features that arise from polymer dewetting (Figure 3.1b).[10] Similar to nanoscale dewetting of liquid films on substrates with micron-scale chemical heterogeneities,[10] the heterogeneity of the GO-PVA surface (*i.e.,i.e.,* graphitic and PVA-covered regions as described above), can support differential growth of PVA. Such growth presumably leads to visible PVA dewetting on the microscale as observed by AFM (Figure 3.1a and Section 3.4.5), and a 1-2 order of magnitude difference between the length scale of the chemical heterogeneity and that of the dewetting pattern, comparable to previous literature.[11] In contrast, when PVA is deposited on a predominantly graphitic surface, a dewetting pattern at the micron scale is not observed by AFM imaging (Section 3.4.5).

Together, the AFM, HRTEM, and EELS data obtained in this study confirm the presence of a hierarchical PVA network structure comprised of nanoscale and microscale features, which is expected to lead to differences in mechanical behavior. The ultra-thin, nanostructured PVA network observed here through HRTEM characterization is evidence of strong interactions between GO and PVA, which can lead to the bridging of microcracks in the GO, resulting in toughening effects. Beyond an ultra-thin layer that arises as a combination of polymer deposition and compression during membrane deflection experiments, additional PVA that does not directly interact with the GO surface cannot bridge in-lane cracks. In this sense, the microscale PVA pattern found in AFM images is not directly responsible for the microoscale crack-bridging that we report herein. As described in Section 3.2.3, where we perform nanomechanics experiments to interrogate this behavior, we show that the toughening observed in GO nanosheets can only arise if nanoconfined PVA chains interact with multiple oxidized domains to enable crack-bridging.

3.2.3 Mechanical Characterization of GO-PVA Nanolaminates

Ideally, GO-PVA nanolamintes are designed for superior toughness and stiffness. The force-deflection profile for a suspended GO-PVA nanolaminate (Figure 3.3a) exhibits an impressive rupture force of 155 ± 31 nN, a large three-fold increase in the maximum load that it can bear before rupture, in comparison to unmodified GO (47 ± 12 nN).[12] Such superior strength cannot be explained using a rule of mixtures (ROM) model, clearly demonstrating that the PVA chains (strength of 40-140 MPa for bulk PVA[13-16] versus 25 GPa for GO[12,17,18]) must have a toughening effect on the GO monolayer, increasing its load-bearing capacity. Furthermore, when the force-deflection profile for GO-PVA nanolaminates (Figure 3.3a) is fit to a linear elastic membrane solution over the early stages of deformation (deflection of 25-50 nm), an elastic modulus $E = 78 \pm 11$ GPa is obtained (Section 3.4.12). This is in good agreement with ROM predictions, and rapidly approaches the theoretical maximum for GO-PVA nanolaminates as PVA becomes atomically thin. Together with the increase in rupture force described above, this reasserts that the nanostructured polymer network provides excellent load transfer and increases toughness while achieving high stiffness. Importantly, the stiffness of the GO-PVA nanolaminate in this work is 2-10 times higher than that of GO-polymer nanocomposites reported in the literature,[1,13,19-21] which highlights the benefit of utilizing ultra-thin polymer layers, approaching atomic thickness, to optimize toughness (via crack-bridging) and stiffness.

One can envision that the polymer nanostructure in GO-PVA nanolaminates, punctuated by a hydrogen bond network, will lead to a synergistic redistribution of nanomechanical loads. As flaws nucleate in the relatively weaker, oxidized domains of GO, PVA chains can bridge these domains (discussed below), enabling microscale crack-bridging mechanisms, and toughening GO (*i.e.,i.e.,* load-bearing capacity). Crack-bridging in GO-PVA nanolaminates further manifests through their highly inelastic behavior after rupture, as they continue to bear significant load for an additional 350 nm of deflection, unlike GO (Figure 3.3a). As we show below, in the discussion of the atomistic modeling of the fracture process, such behavior is only possible if the reinforcing, nanostructured PVA network limits crack growth during the loading process (Figure 3.1c). If the crack length is comparable to the bridging zone length (on the order of the extended length of an adsorbed PVA chain), it is possible to stabilize the developing flaw and limit its growth;[22] specifically, when PVA chain and crack length are comparable, the hydrogen bond network formed between PVA chains and GO is able to transfer load and lead to further crack-bridging at the microscale. Indeed, the rupture of the indented GO-PVA nanolaminates (Figure 3.3b), is confined to the area in direct contact with the AFM tip (> 25 nm radius), in stark contrast to the more prominent rupture typically observed for a single GO nanosheet (Figure 3.3c), suggesting that mechanical energy is dissipated during crack growth. Such a phenomenon can be considered the "microscale" version of crack-bridging mechanisms shown for fiber-reinforced ceramics and concretes,[7,22-24] and provides a practical mechanism to greatly increase the toughness of GO-based materials

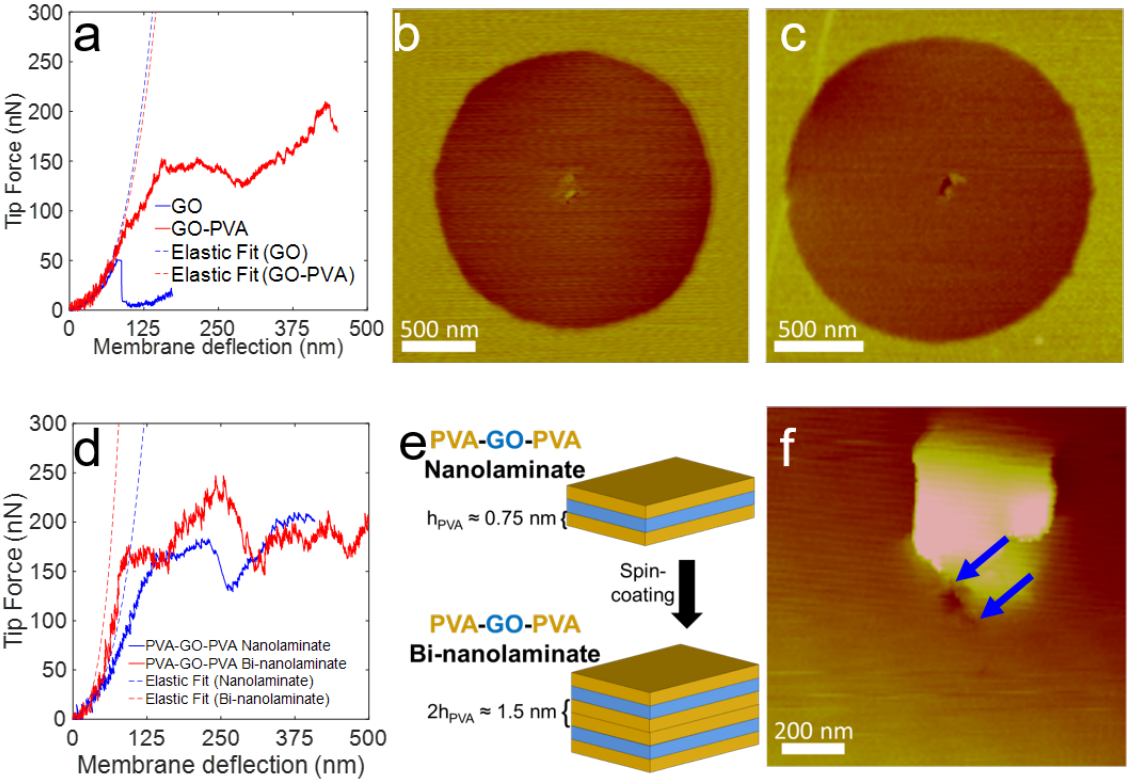

Figure 3.3 (a) Force-deflection curve for GO and GO-PVA. (b,c) Rupture surface for (b) GO-PVA and (c) GO, respectively. (d) Force-deflection curve for PVA-GO-PVA nano- and bi-nanolaminates. (e) Schematic depicting PVA-GO-PVA nanolaminates, obtained by premixing GO and PVA in solution, with PVA thickness *h*. The thickness of the resulting interface in PVA-GO-PVA nano- and bi-nanolaminates is shown in brackets as a multiple of the thickness of the constituent nanolaminate. (f) Rupture surface for PVA-GO-PVA bi-nanolaminates. Nanocracks are highlighted by blue arrows. Regions with brighter color represent larger features in the topology, attributable to bulging of PVA chains near the indented region due to plastic deformations in PVA.

Importantly, the microoscale crack-bridging mechanism observed in GO-PVA nanolaminates implies that a small amount of PVA is needed to toughen GO. The nanoscale indentation experiments reported here were carried out on a GO nanosheet coated with an ultra-thin (1.5 nm) PVA layer, in contrast to previous studies where thicker polymer layers (> 10 nm) were utilized,[1,20] resulting in diminished mechanical properties due to the high volume fraction occupied by the polymer. Furthermore, as computations reveal (Section 3.2.4), the effectiveness of microoscale crack-bridging mechanisms is readily dependent on the interface formed between GO and the crack-bridging PVA chains. Taken together, the current results and previous literature suggest the GO-PVA nanolaminate reported in this work is a synergistic configuration of the building blocks. Indeed, as the thickness of PVA in GO-PVA nanolaminates approaches atomic thickness, PVA chains enable significant toughness enhancement mechanisms and limit the negative effects of increasing polymer volume fraction on stiffness.

3.2.4 Atomistic Basis of Crack-Bridging and Quantification of Energy Release Rate

To investigate the toughening mechanism of GO-PVA, we analyze crack-bridging by PVA chains as illustrated in Figure 3.1c. Specifically, we envisioned utilizing fracture mechanics to quantify the process zone in the wake of the crack, and determine the extent of extrinsic toughening using cohesive laws.[22] For that purpose, we begin by elucidating the synergistic relationship between atomically thin PVA and GO monolayers. We probe interfacial load transfer mechanisms between GO and PVA by quantifying the evolution of traction, *i.e.,* load on a PVA chain when subjected to displacements parallel with GO surfaces, as a function of crack opening. To achieve this, we conducted all-atom MD simulations (see Section 3.4.13 for simulation details) implementing the ReaxFF force field,[25] which has been parametrized[26] for predictions with hydrocarbons and graphene oxide-based systems. Briefly, a single PVA chain (45 monomers, 11 nm contour length) was suspended over two GO sheets, with an initial crack opening of 1 nm, and the sheets were pulled apart to increase crack opening while measuring the traction-crack opening response of PVA. Theoretically, PVA chains should display a significantly strong traction-crack opening response, punctuated by stick-slip traction signatures, due to the reformable nature of interfacial hydrogen bonds between GO and the backbone of the PVA chain. In agreement with this hypothesis, the GO-PVA presents a traction exhibiting peaks and valleys (Figure 3.4a). An average traction of 0.6 nN was determined, due mainly to the presence of functional groups capable of forming a high density of hydrogen bonds. Interestingly, PVA chains load to a peak traction of about 1 nN (Figure 3.4a) and slip, unloading the traction in the chain until new hydrogen bonds reform. The process repeats itself with further sliding of the polymer chains. In stark contrast, such strong traction effects cannot be observed for graphene-PVA as van der Waals interaction dominate, and hydrogen bonds cannot be formed due to the lack of oxygen-containing surface functional groups. Notably, our computations suggest this behavior becomes strain rate insensitive below a critical strain rate value (Section 3.4.14).

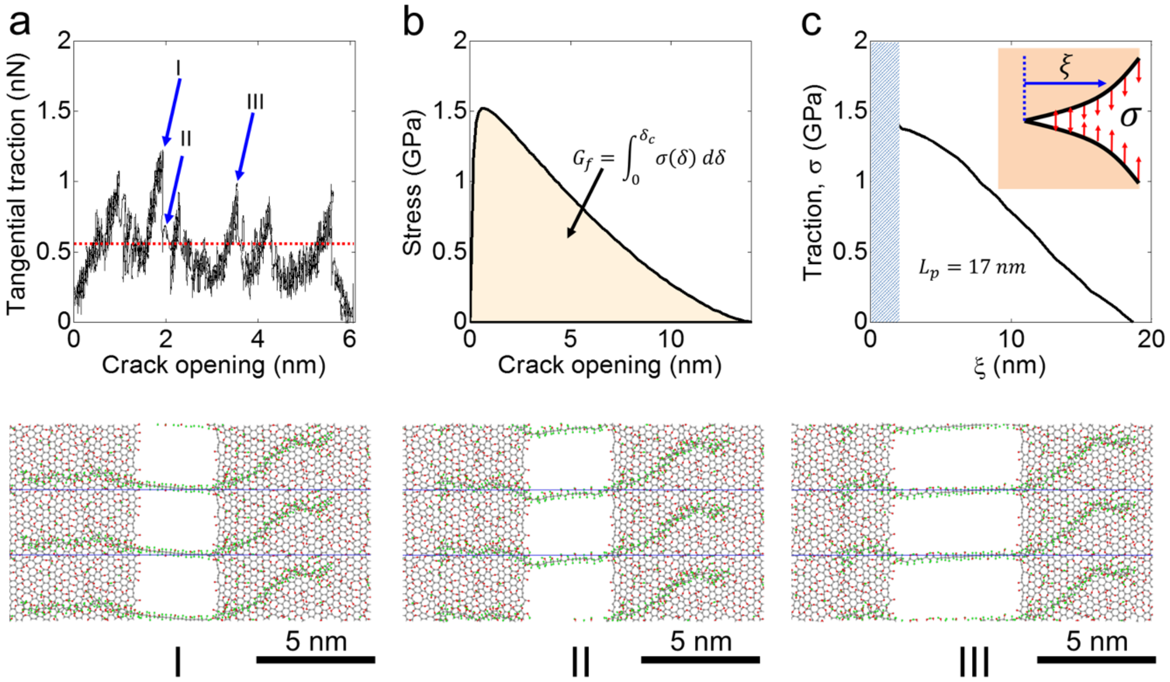

Figure 3.4 (a) Traction-crack opening (Mode II) behavior of a single PVA chain suspended over two GO sheets. Labels denote deformation in the atomistic model, as shown in the bottom row of Figure 3.4. Gray, red and green beads represent carbon, oxygen, and hydrogen atoms, respectively. The simulation domain, bound by solid blue lines, and two periodic images are shown for clarity. (b) Traction-crack opening behavior for an ensemble of PVA chains bridging a crack in GO, as obtained from fracture mechanics model. The integration of this curve reveals the energy release rate contribution from PVA chains. (c) Calculation of process zone length, L_p, from notch test by employing the extended finite element methodology. Inset shows traction-separation contributions, represented by red arrows, accounted for in the solid by explicitly modeling GO normal stress-crack opening (Mode I), and including PVA traction-crack opening contributions after cracks nucleate in GO as smeared Mode I contributions. The shaded region from $\xi = 0$ nm to $\xi = 0.5$ nm corresponds to the region where traction contributions are transferred from GO to the PVA chain.

This hydrogen-bonding, tangential stick-slip mechanism, made possible by the strong interactions between GO and PVA, suggests the atomic basis of the crack-bridging phenomena observed in membrane deflection experiments. High load stresses experienced by the material under the indenter initiate failure in the GO-PVA nanolaminates in the form of microcracks.[12] However, in contrast to pristine GO, these microcracks are bridged by the PVA polymer chains delaying microcrack coalescence and failure. To confirm this hypothesis, the traction-crack opening behavior captured for PVA suspended over GO monolayers is introduced in a fracture mechanics framework[22] to obtain the traction-crack opening response and the energy release rate involved during crack-bridging by an ensemble of PVA chains (Section 3.4.15). Our analysis reveals that the energy release rate G of GO-PVA-which arises as a sum of the energy release rates of GO and PVA crack bridging, G_0 and G_f, respectively-is G = 13.97 nN/nm (Figure 3.4b). In contrast, GO monolayers[27] have G_0 = 4.54-6.11 nN/nm, which is only a third of the GO-PVA system, while graphene has G_0 = 15.9 nN/nm, [27,28] which is comparable to GO-PVA. The model reveals that the average traaction-crack opening response of PVA suspended over GO crack edges, a consequence of reformable stick-slip hydrogen-bonding, is responsible for a three-fold increase in the energy release rate of GO-PVA nanolaminates, making them as tough as monolayer graphene. Indeed, this average traction-crack opening response (Figure 3.4b) develops with small crack openings and is accompanied by a gradual release of traction, stabilizing energy release during crack growth. Notably, the process zone for GO-PVA, *i.e.,* region around the GO crack tip with significant PVA traction that impedes crack opening, measured employing finite element analysis (Section 3.4.15) is ~17 nm and in stark contrast to that of quasi-brittle GO (~0.5 nm; Figure 3.4c). In this light, our observations reveal the importance of interfacial load transfer near the crack tip, provided by PVA chains near the GO surface capable of forming a high density of reformable hydrogen bonds, and show the GO-PVA system to be the molecular analog of ceramics reinforced by short fibers.[22]

3.2.5 Mechanical Characterization of PVA-GO-PVA Nano- and Bi-nanolaminates

The crack-bridging mechanism observed for the GO-PVA nanolaminates investigated here suggests that depositing PVA on both faces of the GO nanosheet should lead to further improvements in strength, without affecting stiffness, if polymer volume fraction is kept constant.

Such PVA-GO-PVA nanolaminates were prepared by spin coating a pre-mixed GO-PVA solution[29] on a patterned substrate (further information provided in Section 3.4.9). Remarkably, this method allows us to reduce the thickness of the polymer layer beyond 1 nm, as AFM imaging suggests both sides of the GO nanosheet are covered by a PVA monolayer with thickness of only ~0.75 nm (total sample thickness = 2.5 nm; Section 3.4.10). Notably, the force-deflection profile of the PVA-GO-PVA nanolaminate (Figure 3.3d) shows a rupture force of 176 ± 24 nN, a 15% increase with respect to that of GO-PVA nanolaminates (155 ± 31 nN). As anticipated, and since the volume fraction of PVA in the system remains constant, the elastic modulus (E = 78 ± 10 GPa) of PVA-GO-PVA nanolaminates remains unchanged from that of GO-PVA (E = 78 ± 11 GPa; Section 3.4.12).

The success in extending the crack-bridging mechanism to PVA-GO-PVA nanolaminates prompted us to explore whether nanoconfined polymer reinforcement still applies to a thicker system, such as PVA-GO-PVA bi-nanolaminates. Through spincoating, we obtained a mix of nanolaminates and bi-nanolaminates on patterned Si substrates. The 5 nm thickness of the latter is consistent with the stacking of two PVA-GO-PVA nanolaminates of 2.5 nm thickness (Figure 3.3e). To ensure the applicability of the analysis used to interpret the experimental results, we compared membrane deflection behavior, applicable to PVA-GO-PVA bi-nanolaminates, to bending in thicker plates (Section 3.4.12). The 2D elastic modulus of bi-nanolaminate PVA-GO-PVA (E_{2D} = 365 ± 72 N/m) scales with the number of PVA-GO-PVA nanolaminates (E_{2D} = 196 ± 26 N/m; Figure 3.3d and Section 3.4.12), suggesting there is excellent load transfer between PVA-GO-PVA nanolaminates. This implies that GO-based nanocomposite materials with superior load-bearing capacity may be obtained by stacking PVA-GO-PVA nanolaminates, as the mechanical properties of individual PVA-GO-PVA nanolaminates are maintained.

Consistent with inter-laminate load transfer, a peak force of 201 ± 53 nN was measured for PVA-GO-PVA bi-nanolaminates. While this 15% increase in rupture force over PVA-GO-PVA nanolaminates (176 ± 24 nN) is only one feature of material performance, force-deflection curves and AFM surface analysis suggest that the material is capable of a large amount of energy dissipation. Indeed, the post-test surface of PVA-GO-PVA bi-nanolaminates distinctly contains a heightened feature, presumably an accumulation of plastically deformed PVA chains (*e.g.,* bulging of the loaded polymer region), in the center of the membrane after significant loading. Closer inspection of this feature (Figure 3.3f) reveals the presence of surrounding nano-cracks (~75-100 nm) which likely did not penetrate through the entire thickness of the bi-nanolaminate assembly as failure within the loading capabilities of the cantilever were exhausted. Based on these observations, we attribute this peak force to the puncture of the top PVA-GO-PVA nanolaminate, which explains why no force scaling is observed. Presumably, a visible fissure is not present because the bottom PVA-GO-PVA nanolaminate behaves as a "reinforcing net" in the indentation process. Ideally, if the bi-nanolaminate could be further deflected, a progressive failure of the layers should occur in the assembly, thereby suggesting the presence of a crack arrest mechanism – a highly desirable feature in the design of nanocomposites.

3.3 Conclusion

In summary, this research demonstrated how GO toughness can be significantly enhanced through controlled interfacial interactions with a soft polymer, and elucidated structure-property relationships present in these GO-PVA nanolaminates. The materials characterization, nanomechanical experiments, and computational studies conducted herein confirmed that deposition of a layer of PVA approaching atomic thickness (~0.75 nm thick) onto the GO surface, leads to significant toughening due to microscale crack-bridging, attributable to hydrogen bond-mediated stick-slip behavior during crack growth. Importantly, the mechanism shown here is the molecular analog of macroscopic crack-bridging observed in ceramic and fiber-reinforced composites, and uncovered strong interfacial synergies between atomically thin polymers and 2D materials that can be exploited in future interfacial designs. Based on our findings, we are confident that the tuning of interfacial interactions will be leveraged to enhance the mechanical performance of a variety of 2D materials and, in turn, stimulate the design of the macroscopic composites with improved load-bearing capacity.

3.4 Materials and Methods

3.4.1 Materials and Instrumentation

Unless otherwise stated, all reagents were used as received. Graphite powder (grade 2139) was purchased from Asbury Carbons Inc. (Asbury, NJ). Sodium nitrate, potassium permanganate, absolute ethanol, concentrated hydrochloric acid, and *n*-butylamine (99.5%) were purchased from Sigma-Aldrich Co., LLC (Milwaukee, WI). Concentrated sulfuric acid, ether, and methanol were purchased from VWR International LLC (Radnor, PA). Phosphoric acid (85 wt %, was purchased from Mallinckrodt Baker Inc. (Phillipsburg, NJ). Hydrogen peroxide (30 wt % in water) was purchased from Sigma-Aldrich Co., LLC (Milwaukee, WI) and refrigerated during storage. Ultrapure deionized water (resistivity 18.2 MΩ cm) was obtained from a Milli-Q Biocel A10 system (Millipore Inc., Billerica, MA). Silicon wafers (Item # 785, 100 mm diameter, p-type, B-doped, single-side polished) and silicon wafers with a 500 nm-thick thermal oxide layer (100 mm diameter, N/Phos-doped, single side-polished) were purchased from University Wafer Inc. (Boston, MA).

HRTEM, STEM, and EELS characterizations were conducted using the Argonne Chromatic Aberration-Corrected TEM (ACAT) (a FEI Titan 80-300 ST with an image aberration corrector to correct both spherical and chromatic aberrations) at an accelerating voltage of 80 kV to reduce knock-on damage. The nanolaminate TEM specimens were prepared by sequential Langmuir-Blodgett deposition of GO and PVA, or spin-coating a premixed aqueous solution of GO and PVA, onto TEM grids (Sections 3.4.4 and 3.4.9). HRTEM images were taken under conditions when spherical and chromatic aberration coefficients are corrected below certain values ($C_s < 5$ μm, $C_c < 10$ μm). Low-loss EELS spectra were recorded in an image-coupled mode. To avoid electron beam damage, a low probe current (5 pA) in STEM mode, relatively large probe size (~0.25 nm), and short dwell time (0.1 second) were used for the EELS line scan.

Scanning electron microscopy (SEM) images were taken using a FEI NovaNano 600 scanning electron microscope (FEI Co., Hillsboro, OR). CHN elemental analysis by combustion and O elemental analysis by pyrolysis were performed by Micro Analysis Inc. (Wilmington, DE), with samples dried at 80 °C under vacuum for 4 h. Water content was measured by Karl Fischer titration using a C20 Compact Karl Fischer Coulometer (Mettler-Toledo International Inc., Columbus, OH) on films dried at 80 °C under vacuum for 4 h, and bath sonicated for 5 min in dry MeOH in a sealed vial. Water contact angles were measured using a VCA Optima contact angle instrument (AST Products Inc., Billerica, MA) by dropping 4 μL of ultrapure deionized water onto the substrate, with measurements taken at three different locations on each substrate.

3.4.2 Synthesis of Graphene Oxide

Each batch of graphite oxide was prepared using a modified Hummer's method.[30] Briefly, a 9:1 v/v mixture of concentrated H_2SO_4 (360 mL):H_3PO_4 (40 mL) was added to a mixture of graphite (3 g) and potassium permanganate (18 g). The reaction mixture was heated to 50 °C and stirred for 12 h. The mixture was then cooled to room temperature and poured over ice (~400 mL), followed by the addition of H_2O_2 (8 mL of a 30 wt % solution) until the solution turned bright yellow. The resulting graphite oxide was filtered through a 250 μm U.S. Standard testing sieve (VWR International LLC, Radnor, PA) and centrifuged (840 *g* for 1 h) in a model 5804R centrifuge (Eppendorf Inc., Westbury, NY) with the supernatant decanted away. The remaining solid was then washed with ultrapure deionized water (200 mL), HCl (200 mL of a 30 wt % solution), and ethanol (2 × 200 mL). After each wash, the mixture was filtered through the sieve and then centrifuged (840 *g* for 1 hour) with the supernatant decanted away. The remaining material was coagulated with ether (200 mL) and filtered over a PTFE membrane (Omnipore, 5 μm pore size, Millipore Inc., Billerica, MA) overnight. The GO filter cake was then dispersed in ultrapure deionized water, with the dispersion stirred for 18 hours. Any residual unexfoliated graphite oxide was removed by centrifuging at 840 *g* for 5 min 2x with the precipitate discarded. The final dispersions contained ~3 mg mL^{-1} of graphene oxide (GO), with a C:O ratio determined by elemental analysis to be 0.92. Accounting for water content of 14.53% results in a C:O ratio of 1.57. GO films for XPS analysis were prepared by drop casting GO solution onto silicon wafers with a thermal oxide layer, followed by drying under ambient conditions.

3.4.3 Preparation of Si Substrates with Microwells *(This work was carried out by Dr. Fan Zhou)*

Si substrates containing arrays of microwells with 1.76 μm diameter and 4 μm depth were fabricated using a combination of photolithography and deep reactive-ion etching (DRIE). A 1.2 μm-thick photoresist layer (S1813 positive photoresist manufactured by Dow Electronic Materials Microposit, catalog number: DEM-10018348, distributed by Capitol Scientific Inc., Austin, TX) was spin-coated onto the Si wafer at 4000 rpm using a Cee 200X spin coater (Brewer Science Inc., Rolla, MO). Following a 1 minute soft bake at 100 °C on a hot plate, the wafer was exposed to UV light (365 nm, 18 mW cm^{-2}) for 4 seconds on a Suss MABA6 Mask Aligner instrument (SÜSS MicroTec AG, Garching, Germany). After exposure, the wafer was developed in a MF 319 developer (manufactured by Dow Electronic Materials Microposit, catalog number: DEM-10018042, Capitol Scientific, Inc, Austin, TX) for 60 seconds. Spin rinsing was carried out with ultrapure deionized water (200 mL) for 30 seconds at approximately 300 rpm, followed by a 60 second spin dry at 3000 rpm.

The resulting photoresist-masked silicon wafer was then subjected to microwell etching using a STS LpX Pegasus DRIE machine (SPTS Technologies Ltd, San Jose, CA). After etching, the remaining photoresist was removed using acetone, and the wafer was cleaned using isopropanol and ultrapure deionized water. This wafer was then cleaved into smaller substrates to be used in the LB deposition and subsequent membrane-deflection experiments.

Prior to LB deposition, the substrates were cleaned using the following procedure: 1) submerged in 2 mL of a 3:1 v/v mixture of conc. H_2SO_4:30 wt % H_2O_2 and heated in a Biotage SPX microwave reactor (Biotage Inc., Uppsala, Sweden, software version 2.3, build 6250) at 180 °C for 45 min, 2) sonicated for 10 min each in ultrapure deionized water (~10 mL), methanol (~10 mL), and ultrapure deionized water (~10 mL), respectively, 3) dried under a flow of nitrogen for 1 min, and 4) treated with O_2 plasma (5 min at 190 W and 10-15 mTorr O_2) in a Model PC-2000 plasma cleaner (South Bay Technology Inc., San Clemente, CA). After this cleaning process, the substrates were left under ambient conditions and their water contact angle was monitored until the desired value was reached prior to LB deposition (~30°, 60° or 90° after 3 hours, 2 days, and 1 week, respectively). As reported previously,[12] the yield of intact suspended GO membranes is dependent on the water contact angle of the substrate (Section 2.4.8). As such, substrates with a water contact angle of approximately 60-70° were used to prevent membrane rupture.

3.4.4 Langmuir–Blodgett Assembly of GO-PVA Nanolaminates

To prepare suspended, GO-PVA nanolaminates for the AFM membrane deflection experiments, the Langmuir-Blodgett (LB) assembly method was employed[8] to first deposit GO, followed by PVA. The as-prepared aqueous GO dispersion was diluted with MeOH to a mixture of 5:1 v/v MeOH:GO dispersion. The Nima model 116 trough (Nima Technologies, Ltd., Espoo, Finland) was cleaned with acetone, and filled with ultrapure deionized water. Typically, the GO/MeOH solution (300-480 μL) was spread onto the water surface dropwise at a rate of 100 μL min^{-1} using a glass syringe, forming a monolayer film on the surface. The surface pressure was monitored using a tensiometer attached to a Wilhelmy plate. The film was allowed to equilibrate for at least 20 min after spreading, and then compressed by barriers at a speed of 100 cm^{2} min^{-1}. The single GO nanosheet was transferred near the onset of the surface pressure increase by vertically dipping the substrate into the trough and slowly pulling it up at a rate of 2 mm min^{-1}.

The LB technique was used to deposit an ultrathin PVA layer onto the suspended GO monolayers. To prevent the GO monolayer from washing off during the deposition, PVA was deposited the day after LB deposition of the GO. A 1 mg mL^{-1} aqueous solution of PVA was diluted with EtOH to a mixture of 5:1 v/v EtOH:ultrapure deionized water. The LB trough was cleaned with acetone, and filled with ultrapure deionized water. Generally, PVA solution (600 μL) was spread onto the water surface dropwise at a rate of 100 μL min^{-1} using a glass syringe, forming a film on the surface. The surface pressure was monitored using a tensiometer attached to a Wilhelmy plate. The film was allowed to equilibrate for at least 20 min after the spreading, and then compressed by barriers at a speed of 100 cm^{2} min^{-1}. The PVA layer was transferred at a surface area of 50 cm^{2} by vertically dipping a substrate containing suspended GO monolayers into the trough and slowly pulling it up at a rate of 2 mm min^{-1}.

3.4.5 Dewetting Mechanism of PVA Chains on the Surface of GO

The HRTEM and AFM data presented above show that microscale polymer features beyond the nanostructured PVA network are present on the surface of GO-PVA nanolaminates (Figure 3.1b). An understanding of the formation mechanisms behind this hierarchical network can provide insight towards the rational design of nanolaminate systems with novel mechanical properties. Such structures presumably arise through a combination of PVA adsorption at the nanoscale and polymer dewetting at the microscale. At the nanoscale, the first monolayer of PVA chains preferentially adsorbs to the oxidized domains through hydrogen-bonding interactions, thus nucleating preferential sites onto which subsequent PVA chains can adsorb. In addition, because the size of the graphitic domains that punctuate the network of oxidized domains is less than the length of an extended PVA chain, some of the PVA chains can presumably bridge across the graphitic domains to connect to other PVA chains on neighboring oxidized domains. This results in the formation of a nanostructured PVA network. The resulting nanoscale heterogeneity (PVA-sparse graphitic and PVA-dense oxidized regions) presumably leads to differential adsorption of PVA at the microscale, and formation of the PVA features observed in AFM images.

In contrast, when PVA is deposited onto reduced GO (rGO) nanosheets, under the same conditions used to fabricate GO-PVA nanolaminates (Section 3.4.4), a largely continuous PVA coating is obtained (Figure 3.5c). The lack of PVA patterns implies that dewetting does not occur due to the more homogeneous surface of rGO, which primarily contains graphitic domains and relatively few oxidized domains. Furthermore, the highly graphitic nature of rGO implies that it engages in predominantly van der Waals interactions with PVA, rather than the hydrogen-bonding present in GO-PVA nanolaminates. Interestingly, the PVA coating on reduced GO is punctuated by small pinholes (Figure 3.5d), suggesting that a small number of oxidized domains serve as surface point heterogeneities that lead to minor dewetting and subsequent pinhole formation.

As alluded to previously, the formation of the hierarchical PVA network may also depend on polymer size. The PVA chains used in this work (~34 nm contour length, molecular weight of 6 kDa) are comparable in size to 4-5 GO oxidized domains, and can engage in extensive hydrogen-bonding with these domains, leading to the even coating of microscale PVA features on the GO surface (Figure 3.1b). However, the use of longer PVA chains (~140 nm contour length, molecular weight of 25 kDa) results in uneven coverage of PVA on the GO surface (Figure 3.5a), implying weaker GO-PVA interactions. This is supported by high-magnification AFM images which reveal PVA nanoparticles on the GO surface (Figure 3.5b), rather than the microscale features observed when shorter PVA chains are used, suggesting that PVA prefers to engage in intramolecular hydrogen-bonding instead of interacting with the GO domains. The acquired data demonstrates that selecting a polymer of appropriate size, that is capable of suitable interactions with GO, can allow unique mechanical properties to manifest in the resulting nanolaminate assembly, such as the microscale crack-bridging reported herein.

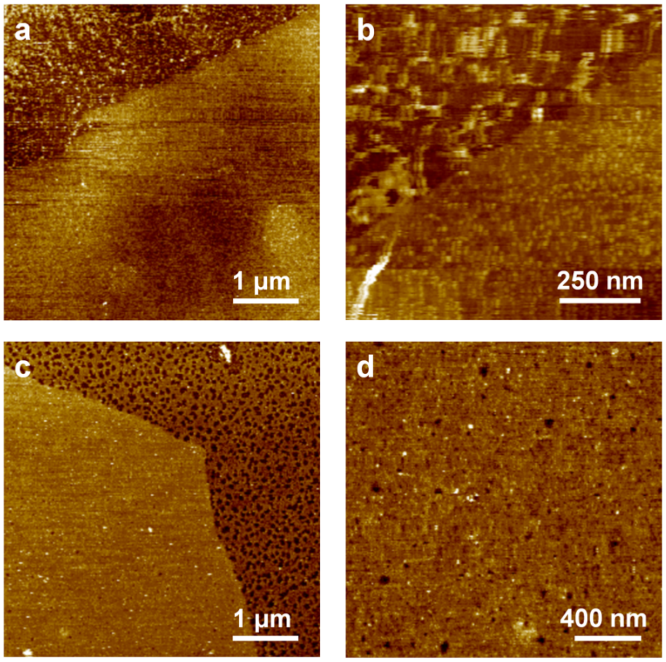

Figure 3.5 (a) Uneven polymer coverage on the surface of a GO nanosheet modified with PVA (25 kDa). (b) PVA (25 kDa) aggregating into nanoparticles on the GO surface, suggesting that at higher polymer molecular weight, PVA-PVA interactions are favored over GO-PVA interactions. (c) rGO modified with a nearly continuous layer of PVA (6 kDa). (d) Pinholes in the PVA (6 kDa) coating on the rGO surface.

3.4.6 EELS Characterization of GO Nanosheets and GO-PVA Nanolaminates

A series of control samples (graphene, GO, GO-PVA, PVA, and amorphous carbon) were prepared and characterized via EELS in TEM mode to serve as references for interpreting the EELS data of GO-PVA nanolaminates, as discussed in Section 3.2.2. Single-layer graphene samples, pre-deposited on Au-coated QUANTIFOIL R 2/4 TEM grids, were obtained from Graphenea Inc. (Cambridge, MA). GO and GO-PVA nanolaminate specimens were deposited onto lacey carbon-coated Cu TEM grids (Product #01895, distributed by Ted Pella Inc., Redding, CA) via the LB method. PVA samples were prepared by spin-coating ~8 μL of an aqueous PVA dispersion (30 mg mL^{-1}) onto lacey carbon-coated Cu TEM grids at 4000 rpm, with an acceleration of 400 rpm used to reach this final speed.

The bare lacey carbon film of the prepared TEM grids served as the amorphous carbon samples. During TEM experiments, a short exposure time of 0.1 second was used to prevent possible amorphous carbon buildup, which could alter the sample's plasmon peak position. The plasmon peak positions of the other reference samples were consistently below that of amorphous carbon (25 eV), suggesting there was no significant carbon buildup during experiments, and the obtained peak positions are representative of the non-contaminated control samples.

Previous studies have shown that the position of the π + σ plasmon peak in the EELS low-loss region (<100 eV) can be used to differentiate carbon-based materials such as graphene,[31] GO,[32] amorphous carbon,[32] and organic polymers.[33] The π + σ peak in the EELS spectrum of unmodified GO is in good agreement with a previous report,[32] and is significantly right-shifted in comparison to the π + σ peak of graphene, attributable to the presence of oxygen and the increased number of sp^3 carbon bonds in GO.[32] For pure PVA, which has a 2:1 C:O content and only sp^3 carbon atoms, the π + σ peak is at 23 eV (Figure 3.6). As such, the addition of a PVA layer (66% sp^3 carbon) on top of GO (~30% sp^3 carbon), as present in GO-PVA nanolaminates, should cause the π + σ plasmon peak of GO to shift to values in the 19-23 eV range. This is indeed observed in the EELS spectrum of GO-PVA nanolaminates, which exhibits a broad feature at ~21 eV (Figure 3.6). As this feature spans a large 17-23 eV range, it likely comprises individual contributions from GO and PVA.

Based on the aforementioned reference data, the position of the plasmon peak in the EELS spectra of GO-PVA nanolaminates obtained in line-scan mode (Figure 3.6) can be used to distinguish between the three different domains present: 1) mainly graphitic (graphene-like; π + σ peak = 15.5 ± 0.5 eV[31]); 2) more oxidized (GO-like; π + σ peak = 18.0 ± 1.0 eV[32]); and 3) PVA-covered (π + σ peak = 21.0 ± 0.5 eV). As discussed in Section 3.2.2, the EELS line scan of a GO-

PVA nanolaminate was interpreted as showing the preferential adsorption of PVA to the oxidized domains of GO.

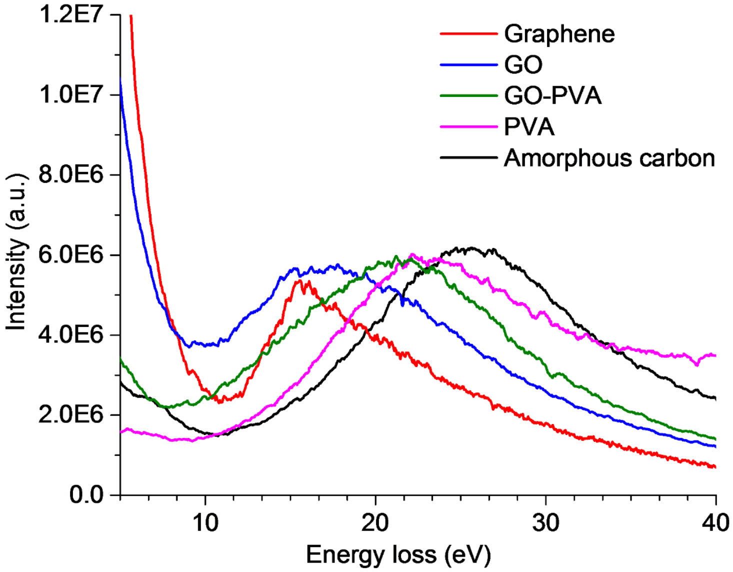

Figure 3.6 EELS spectra (collected in TEM mode) showing the π + σ plasmon peaks of graphene, GO, GO-PVA, PVA, and amorphous carbon.

3.4.7 XPS Characterization of GO Nanosheets and GO-PVA Nanolaminates

X-ray photoelectron spectroscopy (XPS) was gathered in the Keck II/NUANCE facility at Northwestern University using a Thermo Scientific ESCALAB 250Xi (Al Kα radiation, *hν* = 1486.6 eV) (Thermo Fisher Scientific Inc., West Palm Beach, FL) equipped with an electron flood gun. Samples for XPS analysis were prepared via LB deposition of GO and GO-PVA onto Si wafers (Item #785, 100 mm diameter, p-type, B-doped, single side polished) purchased from University Wafer Inc. (Boston, MA). XPS data was obtained from three different locations on the surface of each sample, and was analyzed using Thermo Scientific Avantage Data System software (version 5.923), with a Smart background subtracted prior to peak deconvolution and integration.

While EELS can capture the nanoscale chemical composition of GO-PVA nanolaminates, XPS can confirm the adsorption of PVA molecules on GO nanosheets over the micron length scale, due to the larger XPS spot size (500 μm). Compared to the C1s XPS spectrum of GO, that of GO-PVA exhibits a clear change in the peak position, which can be attributed to the addition of PVA (Figure 3.7). While the spectra of both materials contain a peak at a binding energy of 284.5 eV, corresponding to the graphitic carbon atoms of GO,[34] the second peak in the GO-PVA spectrum (centered at 287 eV) is clearly shifted to a lower binding energy than that of GO (centered at 286.5 eV). In the GO spectrum, this second peak can be deconvoluted into five components corresponding to the oxygenated functional groups of GO, with the hydroxyl group at the lowest binding energy.[35,36] Modification of the GO surface with PVA, which contains hydroxyl groups that have a similar binding energy (286.1 eV[37]) to those of GO (285.9 eV[38]) increases the overall hydroxyl content. As such, it is reasonable to expect the peak representing the combined oxygenated groups of GO to shift to a lower binding energy. This explains the shift in the oxygenated peak position of GO-PVA and confirms the adsorption of PVA on GO.

In addition to the peak position, the relative peak intensities are noticeably different in GO and GO-PVA (Figure 3.7). The intensity of the oxygenated peak in GO (287 eV) is significantly greater than that of the peak corresponding to graphitic carbon atoms (284.5 eV). In contrast, the intensity of the oxygenated peak in GO-PVA (286.5 eV) is similar to that of the graphitic carbon peak, suggesting that addition of PVA decreases the oxygen to carbon (O:C) ratio in GO-PVA. This is reasonable as the synthesized GO nanosheets have an O:C ratio of 0.66 (as determined by XPS survey scan), while pure PVA has an O:C ratio of 0.5. For the prepared GO-PVA nanolaminates, which contain GO and PVA in an approximate 1:1.5 weight ratio (based on the thickness and similar chemical composition of the two materials), an O:C ratio of 0.56 would be expected. In agreement with this prediction, the measured O:C ratio for the prepared GO-PVA nanolaminates is 0.61. Together with the XPS spectrum of GO-PVA, this data confirms that the

PVA coverage detected by EELS is also present across the entire surface of GO-PVA nanolaminates.

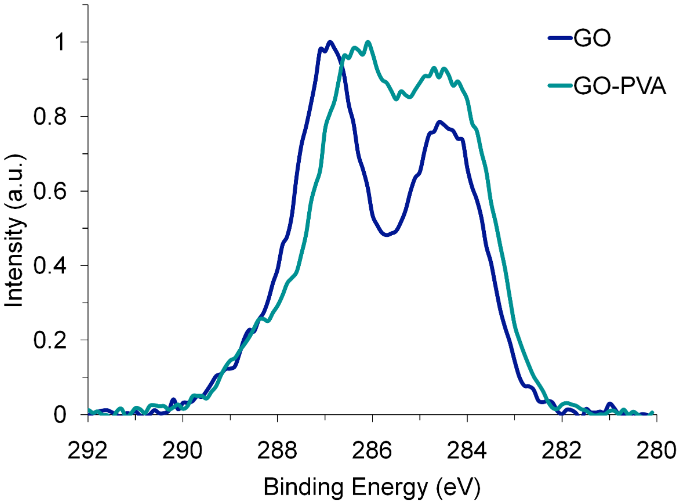

Figure 3.7 C1s XPS spectra of GO and GO-PVA. Both the peak shape and position of the GO spectrum change upon addition of PVA, indicating the successful GO modification.

3.4.8 FFT Patterns of GO Nanosheets and GO-PVA Nanolaminates

A comparison of the fast Fourier transform (FFT) patterns of GO and GO-PVA reveals no significant differences between the two materials (Figure 3.8b,c), showing that TEM analysis alone cannot distinguish between them. Due to the presence of graphitic domains in GO and GO-PVA, both materials exhibit a symmetric six-fold pattern similar to that of pristine graphene (Figure 3.8a). The blurring of this six-fold pattern is attributed to the severe breaking of lattice symmetry in the graphitic domains of GO and GO-PVA.

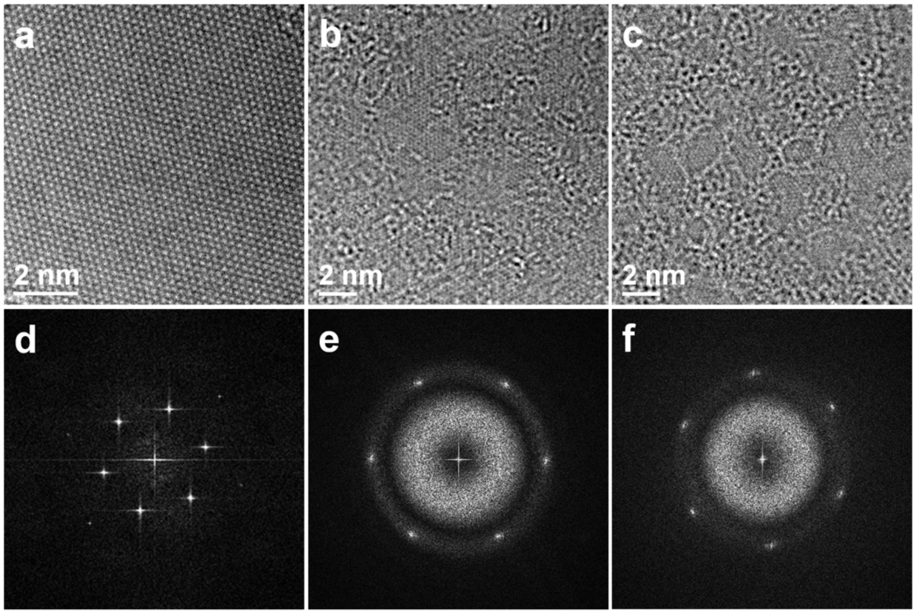

Figure 3.8 HRTEM images and fast Fourier transform (FFT) patterns of single-layer (a) graphene, (b) GO, and (c) GO-PVA. Both GO and GO-PVA exhibit graphitic domains dispersed throughout a continuous network of oxidized domains.

3.4.9 Fabrication of PVA-GO-PVA Nano- and Bi-nanolaminates

An aqueous PVA solution was prepared by dissolving PVA (200 mg) in ultrapure deionized water (16.7 mL) and stirring for at least 3 hours. This solution was mixed with the as-prepared aqueous GO dispersion (3.335 mL) to yield a 1:20 w/w GO:PVA dispersion, which was diluted to a final volume of 30 mL and centrifuged at 840 *g* rcf for 20 min. The supernatant was decanted to remove excess PVA not bound to GO nanosheets and the precipitate was re-dispersed in ~27 mL of ultrapure deionized water. The resulting dispersion of PVA-GO-PVA was spin-coated onto the patterned Si substrates at 2000 rpm, with an acceleration of 200 rpm to obtain a mix of PVA-GO-PVA nano- and bi-nanolaminates, which could be distinguished based on SEM and AFM characterization.

3.4.10 Thickness of GO Nanosheets, Nanolaminates, and Bi-nanolaminates

Comparing AFM thickness measurements of GO nanosheets before and after PVA modification revealed an increase in thickness, indicating the successful adsorption of PVA chains onto GO. Unmodified GO nanosheets have a thickness of about 1 nm (Figure 3.9a), in good agreement with previous reports.[8,39] After Langmuir-Blodgett deposition of an ultra-thin layer of PVA onto GO nanosheets (Section 3.4.4), the thickness of the resulting GO-PVA nanolaminates is around 2.5 nm (Figure 3.9b), suggesting that the layer of PVA on GO is about 1.5 nm thick. Compared to GO, the increased local height variations on the GO-PVA nanolaminate surface are attributed to the discontinuous microscale PVA network on GO, as discussed in the main manuscript. In contrast, the local surface height of the PVA-GO-PVA nanolaminates is more uniform, despite having similar measured thickness as the GO-PVA nanolaminates (about 2.5 nm; Figure 3.9c, orange line). This is due to the difference in fabrication process: PVA-GO-PVA nanolaminates were produced by spin-coating a premixed solution of GO and PVA, rather than Langmuir-Blodgett deposition (Section 3.4.9), which presumably results in more homogeneous PVA coverage at the microscale.

In addition, an even thinner PVA layer can be achieved by spin-coating, as PVA chains adsorb to both faces of GO nanosheets within the premixed solution. This implies that the PVA layer on each face is only about 0.75 nm thick. Therefore, bilayer PVA-GO-PVA nanolaminates comprising a stack of two PVA-GO-PVA nanolaminates should have a thickness of around 5 nm. As seen in Figure 3.9c (green line), the thickness of a PVA-GO-PVA nanolaminate stacked on top of another PVA-GO-PVA nanolaminate is about 2.5 nm, suggesting that the entire bilayer assembly does indeed have a thickness of around 5 nm. Together, the AFM measurements clearly show the presence of PVA on GO nanosheets and confirm that the employed fabrication methods can achieve ultrathin (~0.75-1.5 nm) PVA layers on GO.

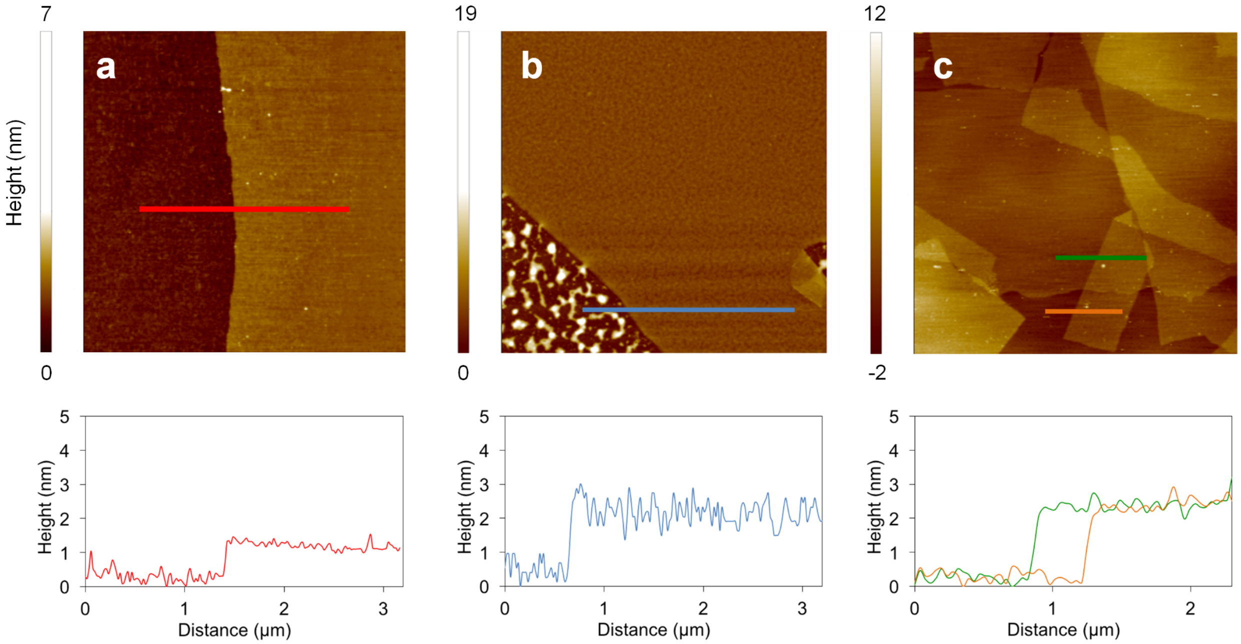

Figure 3.9 (a) GO nanosheet, with a height of ~1 nm. (b) GO-PVA nanolaminate, with a height of ~2.5 nm. The height variation of the nanolaminate is due to the microscale PVA network on the surface of GO. (c) PVA-GO-PVA nano- and bi-nanolaminates. PVA-GO-PVA nanolaminates on both Si (orange line) and another nanolaminate (green line) exhibit a height of ~2.5 nm; as such, the bi-nanolaminate is expected to have a thickness of ~ 5 nm.

3.4.11 Atomic Force Microscopy Membrane Deflection Tests

A single-crystal diamond probe (catalog number: ART D160, K-TEK Nanotechnology, Wilsonville, OR) was used to indent at the membrane center with an AFM (Dimension 3100, Veeco, Plainview, NY). The stiffness of the cantilever (k = 3.18 N m^{-1}) was calibrated using a standard cantilever (CLFC-NOBO, Bruker).[40] The tip radius of the AFM probe (R = 25 nm) was measured by an FEI NovaNano 600 SEM (FEI Co., Hillsboro, OR). All experiments were performed at room temperature and 16% humidity inside a customized environmental chamber. A constant deflection rate of 1µm s^{-1} was used in all tests.

For a suspended, circular, linear elastic membrane under a central load, the force vs. deflection response can be approximated as[41]

$$F = \pi \sigma_0 h \delta + \frac{Eh}{q^3 a^2} \delta^3 \qquad 3.1$$

where F is the applied force, δ is the membrane center deflection, h is the effective thickness of the specimen (Section 3.4.10), σ_0 is the pre-stress in the membrane, a is the membrane radius, E is the elastic modulus, and q is a dimensionless constant defined as $q = (1.05 - 0.15v - 0.16v^2)^{-1}$ where v is the Poisson's ratio. According to previous density functional-based tight-binding (DFTB) calculations,[12,18] the Poisson's ratio of the systems studied here was taken as 0.2. We defined specific guidelines to select the fitting region on the raw data (Section 3.4.12) to achieve consistency when fitting the linear elastic behavior of different samples.

3.4.12 Elastic and Rupture Force Analysis of Membrane Deflection Results

To consistently fit AFM force-deflection curves obtained from different samples, a set of criteria was established for selecting the region of the curve to be fitted using the linear elastic, membrane deflection model.[41] Based on these criteria, the first point of the fitted region is selected as the point at which the force in the AFM cantilever matches the average force measured as the tip approaches the membrane as shown in Figure 3.10a. This is the point where the force in the cantilever is zero post-membrane adhesion (*i.e.,i.e.,* after the cantilever straightens after snapping into the membrane), the adhesion and deflection forces are balanced, and the tip effective force is zero. This selection is reasonable because adhesive effects are eliminated from the fitting process and only loads applied directly on the membrane by the AFM tip are considered. The final point of the fitted region is chosen at first occurrence of non-linear behavior, as determined by manipulating the linear elastic, membrane deflection model to the form

$$\ln F \approx 3 \ln \delta + \ln\left(\frac{Eh}{q^3 a^2}\right) \tag{3.2}$$

for large deflections (Figure 3.10b). Based on these two points, the force deflection-curves are then fitted to the linear elastic, membrane deflection model using an in-house MATLAB code (Version 2012a, MathWorks).

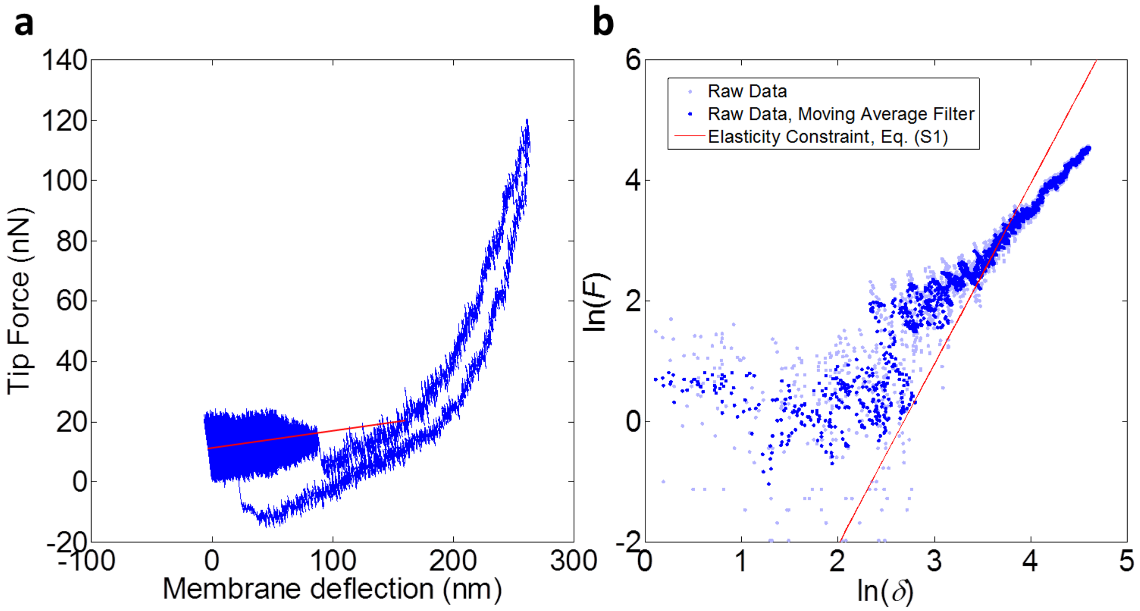

Figure 3.10 (a) Selection of first point for fitting the AFM force-deflection curves. This point corresponds to the deflection value when the tip effective force, post-membrane adhesion (*i.e.,i.e.,* after the cantilever straightens after snapping into the membrane), matches the average value force measured during tip approach. (b) Selection of the last point for fitting the AFM force-deflection curves, when the experimental data deviate from the value of the slope given by Equation 3.2.

Table 3.1 and Figure 3.11 summarize the results obtained by fitting the obtained AFM membrane deflection data, as described in Section 3.4.11, for GO-PVA, PVA-GO-PVA, and $(\text{PVA-GO-PVA})_2$ nanolaminates. The elastic moduli of polymer-covered GO materials is lower than that of GO and in agreement with the rule of mixtures (ROM),[42] attributable to the significant volume fraction occupied by the soft PVA component. As all the nanolaminate samples contained equivalent volume fractions of GO and PVA, it is reasonable to expect that their elastic moduli should remain constant under the ROM framework. In terms of the performed analysis, membrane deflection theory is unable to model the experimental results as the number of layers in the system increases and the problem approaches plate bending theory. In this light, and given that (PVA-GO-PVA)$_2$ bi-nanolaminates consist of 6 total material layers, we assume that membrane deflection theory still holds given: i) the low stiffness of PVA, *i.e.,* the indentation is effectively over two stiff GO layers, and ii) the cubic nature of the force-deflection behavior measured experimentally, *i.e.,* force-deflection is linear when plate bending is dominant.[43] Given our assumptions, the 2D elastic modulus of (PVA-GO-PVA)$_2$ nanolaminates should follow the modulus scaling relation $E_{2D,n} = nE_{2D}$, since the 2D modulus of a system containing n layers of 2D elastic modulus E_{2D} should be $E_{2D,n}$. Interestingly, the highest prestresses measured herein for GO-PVA nanolaminates (0.06 GPa ± 0.03 GPa) are much lower than those previously found for GO (0.7 ± 0.3 GPa),[12] suggesting that PVA can induce significant lattice relaxation within the GO sheets.

Table 3.1 Elastic modulus and prestress obtained in experiments based on linear elastic analysis from force-deflection curves.

System	2D elastic modulus (N/m)	Modulus (GPa)	Prestress (GPa)
GO[12]	192 ± 21	256 ± 28	0.7 ± 0.3
GO-PVA	196 ± 28	78 ± 11	0.06 ± 0.03
PVA-GO-PVA Nanolaminate	196 ± 26	78 ± 10	0.03 ± 0.01
(PVA-GO-PVA)$_2$ Bi-nanolaminate	365 ± 72	72 ± 14	0.02 ± 0.01

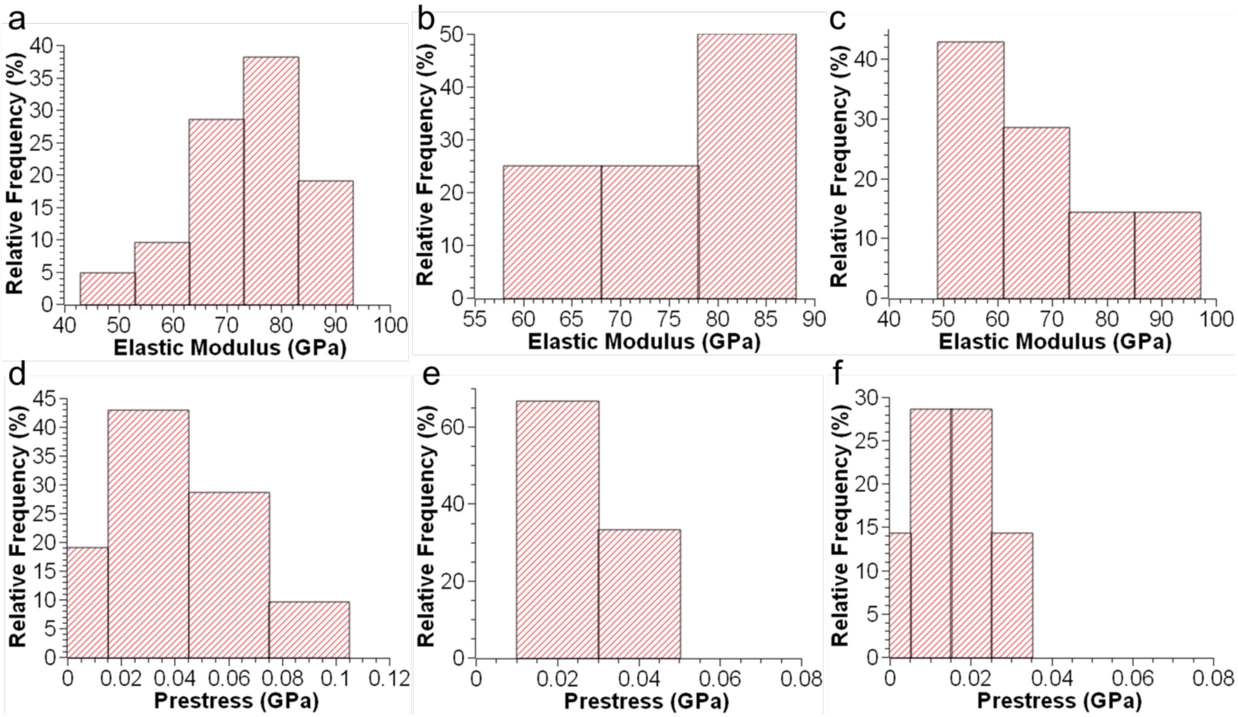

Figure 3.11 (a-c) Elastic modulus as obtained from linear elastic fit for (a) GO-PVA nanolaminate, (b) PVA-GO-PVA nanolaminates and (c) $(PVA\text{-}GO\text{-}PVA)_2$ bi-nanolaminate samples. (d-f) Prestress as obtained from linear elastic fit for (d) GO-PVA nanolaminate, (e) PVA-GO-PVA nanolaminate and (f) $(PVA\text{-}GO\text{-}PVA)_2$ bi-nanolaminate samples.

3.4.13 All-Atom Molecular Dynamics Simulations of GO-PVA Fracture Process

The Large-scale Atomic/Molecular Massively Parallel Simulator (LAMMPS) software package was employed to carry out all-atom MD simulations.[44] The ReaxFF force field,[25] as parametrized[26] for simulations with hydrocarbons and graphene oxide-based systems, was employed for all simulations described. Systems comprise a single PVA chain, 45 monomers in length, suspended over two 2 x 7 nm^2 GO sheets with a 70% degree of oxidation and a 4:1 epoxide:hydroxyl functional group ratio (Figure 3.4a) with an initial crack opening of 1 nm. Periodic boundary conditions were applied in the x and y directions, and a timestep of 0.2 fs was employed to consider the vibrational frequency of H atoms present in PVA and GO.

The system was first equilibrated in an NVT ensemble at a temperature of 300 K for 200 ps. The total energy of the system was monitored until convergence is achieved during equilibration, before equilibrated structures are subjected to loading. Then, a displacement-controlled uniaxial tensile strain experiment is performed by deforming the simulation box along the PVA chain axial direction (Figure 3.4a) in an NVT ensemble at 300K at a strain rate of 1×10^9 s^{-1}. Per-atom virial stresses for PVA and GO are independently calculated and summed, and subsequently averaged over all the atoms in each phase to obtain average virial stresses. Forces in the PVA chain are obtained by scaling virial stresses considering the PVA chain arc length (~13 nm). Crack opening is calculated by measuring the average distance between the atoms involved in the GO crack edges (Figure 3.4a).

To calculate the effective area of GO-PVA membranes four PVA chains, 45 monomers in length and separated by a lateral distance of 0.5 nm, were suspended over two 2 x 7 nm^2 GO sheets, separated by an initial crack opening of 1 nm, with a 70% degree of oxidation and a 4:1 epoxide:hydroxyl functional group ratio. The system was equilibrated in an NVT ensemble at a temperature of 300 K for 200 ps. The total energy of the system was monitored until convergence is achieved during equilibration, before equilibrated structures were utilized for calculations. The cross-sectional area of GO and PVA chains was calculated and summed to obtain the effective area of GO-PVA membranes – as required to estimate the energy release rate of GO-PVA (Section 3.4.14).

3.4.14 Strain Rate Sensitivity of Molecular Dynamics Calculations

The dynamics of hydrogen bond reformation have been previously explored in the literature.[45,46] Specifically, the bond reformation velocity for hydrogen bonded systems, which considers the time and distance over which hydrogen bond reforming processes occur, has been estimated between 0.025-125 m s^{-1}, with an average speed of 35.7 m s^{-1}. In this light, and to further verify strain rate sensitivity in our study, we conducted MD simulations of GO-PVA tensioning to extract traction-crack opening behavior using strain rates between 1x10^{8} s^{-1} (v = 1.5 m s^{-1}) and 1x10^{10} s^{-1} (v = 150 m s^{-1}), as shown in Figure 3.11. Our results clearly suggest there is no significant strain rate dependence when the strain rate is below 1x10^{9} s^{-1} (v = 15 m s^{-1}), which justifies the values and trends for traction-crack opening utilized in Section 3.4.15.

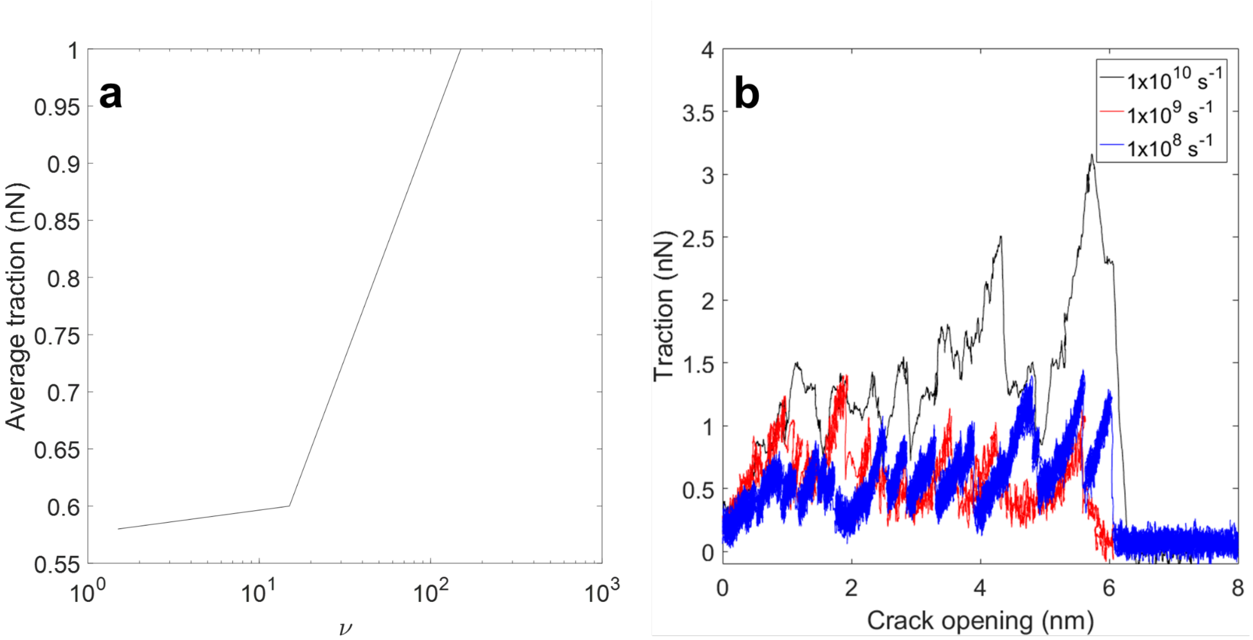

Figure 3.12 (a) Average traction observed during calculations for GO-PVA nanolaminates, as a function of pulling speed, *i.e.,* strain rate. (b) Traction-crack opening response for GO-PVA nanolaminates simulated in this study.

3.4.15 Energy Release Rate Estimation for GO-PVA Nanolaminates

To understand the magnitude of the crack bridging provided by the ultra-thin PVA network deposited over GO monolayers, concepts from fracture mechanics can be used to compare the energy release rate of GO and GO-PVA. In particular, it is well-established in the mechanics community that such bridging effects will result in a crack resistance curve.[22] The starting point of such a curve will be equal to the energy release rate of the matrix, *e.g.,* the supporting substrate for the fiber, or GO in this case. As the crack opens, and when this process reaches a steady state, the curve will plateau at a value that corresponds to the sum of the energy release rate contributions of the matrix and the crack bridging fibers. For GO-PVA, the crack bridging effect of PVA chains can be obtained by considering this plateau value. The total energy release rate of a system where crack bridging manifests, at steady state, is given by[22]

$$G = G_0 + G_f = G_0 + \int_0^{\delta_c} \sigma_t(\delta) d\delta \qquad 3.3$$

where G is the energy release rate of the composite system, G_0 is the energy release rate of the matrix (*i.e.,* GO) and G_f is the energy release rate of the crack bridging fiber (*i.e.,* the PVA chains). The energy release rate of the PVA chains, G_f, depends in turn on the crack opening δ and their tangential traction, σ.

In the derivation of the model, the assumptions are that: i) PVA chains have a random distribution in location and orientation, ii) the total length of all PVA chains is equal, and iii) the PVA chains are straight when suspended over a crack edge. Additionally, PVA chains are characterized based on the geometry shown in Figure 3.12a. The total chain length, L_f, and the embedded chain length, z, are critical components in determining the effective length of a PVA chain that can contribute to load bearing and provide reformable hydrogen-bonding with GO.

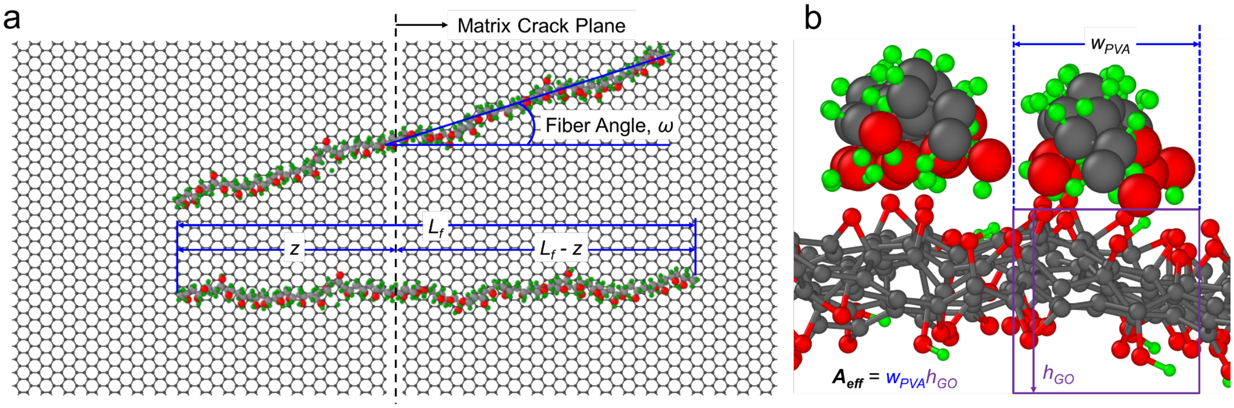

Figure 3.13 (a) Schematic of top view of GO-PVA. Gray, red and green beads represent carbon, oxygen and hydrogen atoms, respectively. GO functional groups are hidden for clarity. The geometrical definitions involved in the model are shown. (b) Schematic of cross-sectional view of GO-PVA showing the definition of the effective area of the model, which corresponds to the cross-sectional area of GO in contact with a PVA chain of width w_{PVA}. Gray, red and green beads represent carbon, oxygen and hydrogen atoms, respectively.

PVA chains can only be considered as crack bridging elements when subject to the condition $z \geq 0$. For uniform PVA chain lengths, the embedded length probability density function is assumed to be

$$p(z) = \frac{2}{L_f} \text{ for } 0 \leq z \leq \frac{L_f}{2} \qquad 3.4$$

Similarly, the probability density function for the effective PVA chain angle is given by

$$p(\omega) = \cos(\omega) \text{ for } 0 \leq \omega \leq \frac{\pi}{2} \qquad 3.5$$

where ω corresponds to the angle between lines normal to the matrix crack plane and a given PVA chain, and symmetry has been utilized to reduce the lower bounds of the system. Based on the molecular dynamics (MD) simulations performed herein, and assuming that hydrogen bonding operates isotropically and that PVA chains with the same embedded length z have the same tangential traction-crack opening behavior, stretching force on a PVA chain corresponding to an effective crack opening, δ_ω, can be determined by

$$\delta_{\omega} = \frac{\delta}{\cos\omega} \quad 3.6$$

To deduce the tensile behavior of the composite material, it is necessary to capture the traction transmitted across the matrix crack by integrating the traction contributions of each PVA chain over the aforementioned distributions, which corresponds to

$$\sigma_t = \frac{1}{A_{GO}} \int_0^{\frac{\pi}{2}} \left[\int_0^{\frac{L_f}{2}} t(z,\delta,\omega) p(z) dz \right] p(\omega) d\omega \quad 3.7$$

where A_{GO} corresponds to the cross-sectional area of GO that is covered by this PVA chain (which can be obtained by calculating the coverage density of PVA chains in the system, see Figure 3.12b), t corresponds to the traction-crack opening behavior of each individual PVA chain and p corresponds to probability distribution functions.

The MD calculations performed using ReaxFF, shown in Figure 3.4, illustrate the traction-crack opening behavior of a single PVA chain suspended over GO, and can be used to train a general model towards the numerical integration of Equation 3.7. The traction-crack opening behavior obtained from MD simulation results was fitted by an equation of the form $t = C_1 tan^{-1}(C_2\delta)$ as shown in Figure 3.13. For PVA chains, the fitting procedure revealed C_1 = 0.4033 nN and C_2 = 10.

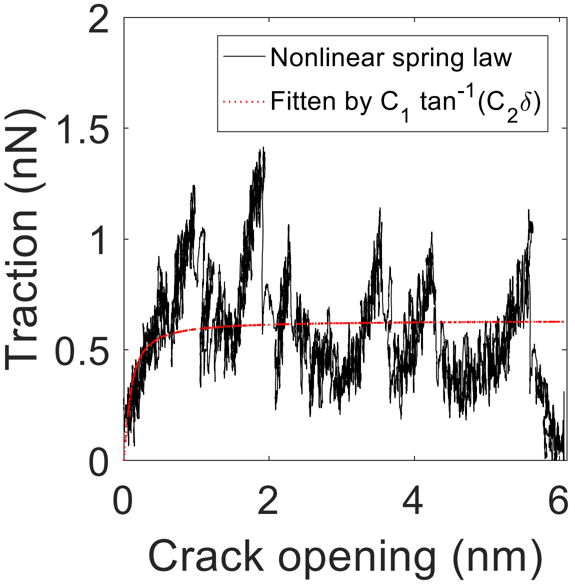

Figure 3.14 Traction-crack opening behavior of a PVA fiber suspended over GO with a 1 nm crack opening as obtained from all-atom molecular dynamics response. Subsequently, the response is fitted by a mathematical model to approximate the traction-crack opening law.

The molecular weight of PVA chains used in this report (6 kDa) contain approximately 130 monomers per chain and have a total chain length of approximately 34 nm upon full extension. To ensure the proposed model for the traction-crack opening behavior is physically meaningful and agrees with the constraint enforced by Equation 3.4, then $L_f/2$ = 14 nm, providing a safety factor to account for PVA chain length distribution in the prepared samples, and to ensure the model does not over-predict energy release rates.

Based on the proposed model (Figure 3.13), a number of scenarios are possible with different chain lengths. The most intuitive scenario occurs when the PVA chain lies completely on only side of the crack, leading to no observable bridging ($z < 0$). Notably, when z is shorter than the critical length ($z < 1$ nm), the chain will experience a reduced number of hydrogen-bonding stick-slip events leading to a traction determined by the model, and a short pull-out distance for the chain. However, when z exceeds the critical length ($z > 1$ nm), the chain will slide and be subjected to a significant number of hydrogen-bonding stick-slip events before being pulled out.

The model derived for the tangential traction-crack opening, when subjected to Equation 3.6, has the general form

$$t = t(\delta_\omega) \text{ for } \delta_\omega < z \qquad 3.8$$

$$t = 0 \text{ for } \delta_\omega \geq z \qquad 3.9$$

With this general form, the traction of a PVA chain as a function of crack opening can be computed as:

$$\sigma_t = \frac{1}{A_{GO}} \int_0^{\frac{\pi}{2}} \left[\int_{\delta/\cos(\omega)}^{L_f/2} 0.4033 \tan^{-1}\left(10 \frac{\delta}{\cos\omega}\right) \frac{2}{L_f} dz \right] \cos(\omega) d\omega \qquad 3.10$$

or equivalently

$$\sigma_t = \frac{2}{A_{GO} L_f} \int_0^{\pi/2} 0.4033 \tan^{-1}\left(10 \frac{\delta}{\cos\omega}\right) \left[\frac{L_f}{2} - \frac{\delta}{\cos\omega} \right] \cos(\omega) d\omega \qquad 3.11$$

Based on the composition of the system then $L_f = 28$ nm. Furthermore, based on ReaxFF MD simulations then $A_{eff} = 0.480$ nm^2, providing all the necessary values and enabling numerical integration to obtain the results shown in Figure 3.14.

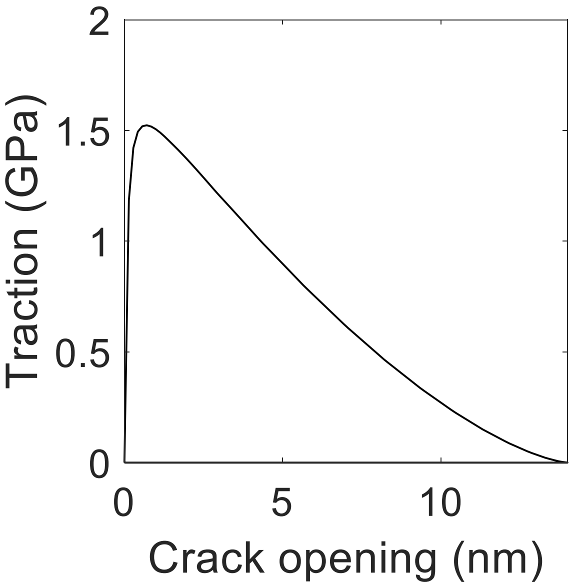

Figure 3.15 Traction-crack opening behavior of GO bridged by PVA chains at the crack edge, by employing the model derived herein. Numerical integration of this traction-crack opening law yields the energy release rate contribution of PVA chains, G_f.

The obtained tangential traction-crack opening shows an early development of the shear strength of PVA chains, making PVA chain crack bridging effective when the GO crack opening is still small and preventing crack blunting in GO. In addition, the tangential traction-crack opening behavior of the composite material shows a gradual release of stress, resulting in a smooth transfer of stress between GO and PVA chains as load is developed. The decrease in stress arises from the reduction in overlap between PVA chains and GO surfaces, and rationalizes the reduction in stress with crack opening. These observations are consistent with the physical picture of crack bridging, and explain features observed in the experiments.

Finally, to obtain a quantification of the increase in energy release rate of the composite material compared to GO, one can employ Equation 3.3. Numerically integrating the curve shown in Figure 3.14 reveals $G_f = 9.43$ nN/nm, comparable to G_0 (4.54-6.11 nN/nm[27]), leading to an energy release rate G for GO-PVA nanolaminates equal to 13.97 nN/nm, a three-fold increase in energy release rate when compared to GO only. Importantly, this calculation likely serves as a lower bound due to the simple geometry assumed for PVA chains, as they can likely interact with one another, and with GO, adapting a more complex morphology than the one assumed herein. Nevertheless, the numerical results are consistent with AFM membrane deflection experiments, and the physical behavior of PVA near GO and graphene crack edges as observed in all-atom MD simulations (Figure 3.4) highlights the significant role that PVA chains have in delaying failure and stabilizing the mechanical behavior of GO.

3.4.16 Process Zone Estimation Based on Extended Finite Elements Methodology

The extended finite element methodology (XFEM),[47] as implemented in ABAQUS 6.14, was applied to model the fracture process in GO-PVA by considering the crack opening traction-separation behavior of GO and PVA. Plane-stress elements (CPS4) as implemented in ABAQUS 6.14 are utilized, with element size of 0.5 nm. To conduct our study, a 10 x 100 nm^2 GO sheet with a 2 nm long slit (represented as a strong discontinuity in the XFEM method) was designed. Simulations of GO, *i.e.,* no PVA is present, are conducted by imposing a linear elastic fracture mechanics failure criteria based on the critical energy release rate of GO[27] ($G_c = G_0$, 4.54-6.11 nN/nm). GO is assumed to behave as an isotropic, linear elastic material with Young's modulus E = 220 GPa and Poisson's ratio v = 0.2. PVA is then implicitly considered in the system by including the traction-crack opening behavior produced after GO nucleates a flaw. To estimate the process zone, the traction near the crack tip is extracted after steady state crack growth is achieved. The process zone is defined as the distance over which load is being borne by the PVA traction-crack opening law, and is non-zero (Figure 3.4c).

Chapter 4

The Effect of Porosity on Scaling the Nanomechanical Properties of Single-Layer GO to Bulk Multilayer Films

Portions of this chapter may appear in the following manuscript:

Mao, L.;[†] Soler-Crespo, R. A.;[†] Park, H.; Espinosa, H. D.; Han, T. H.; Nguyen, S. T.; Huang, J., Stiffening of graphene oxide films by soft porous sheets. *Manuscript to be submitted.*

[†] Equal contribution

4.1 Introduction

In addition to its chemical structure, the porosity of GO is another structural feature that can be modified synthetically.[1,2] GO sheets contain intrinsic in-plane pores (typically <5 nm^2)[3] that form during the oxidation and exfoliation process; in addition, the porosity of the basal plane can be increased through chemical etching.[1] While pores are usually considered as structural defects that lower the strength and stiffness of graphene-based sheets at the single-layer level,[4] assembling porous constituents into bulk multilayered films can enable failure mechanisms that are significantly different from those observed in single-layer GO sheets, thus affording improved mechanical properties. GO sheets provide a unique opportunity to investigate how mechanical properties change with length scale, as they can be easily assembled into bulk multilayered structures[5] due to their high aspect ratio and two-dimensional (2D) structure.

In this chapter, we compare the mechanical properties of porous single-layer GO sheets with that of their bulk multilayer films. At the single-layer level, the elastic modulus of GO sheets decreases rapidly as their porosity increases, but becomes much less sensitive for bulk GO films. Surprisingly, co-assembly of pristine GO sheets and the soft high-porosity sheets with near-zero elastic modulus leads to even stiffer GO films. These results suggest that un-etched sheets are intrinsically disadvantageous building blocks for scaling up mechanical properties, and the much softer porous sheets can effectively act as a binder to improve interlayer stacking.

4.2 Results and Discussion

4.2.1 Synthesis and Characterization of Etched GO

Porous GO sheets were synthesized by chemically etching single-layer GO sheets as shown in Figure 4.1a, with the reaction time varied for 1, 3, or 5 hours to systematically tune the porosity. High-resolution transmission electron microscopy (HRTEM) images (Figure 4.1b-e) confirmed the successful generation of nanopores, and clearly show an increase in porosity as the etch time is extended (Figure 4.1c-e). Based on analysis of the HRTEM images, both the average nanopore size and area fraction corresponding to nanopores were found to increase with etch time. Together, these data show that the porosity can be readily tuned by controlling the reaction time.

A previous study has suggested that nanopore formation begins at the sp^3 oxidized domains of a GO sheet.[1] This implies that the etching process should not decrease the average sheet size, as it initiates at locations within a sheet rather than at its edges. Indeed, we observed little reduction in the average sheet size after the generation of nanopores, based on an analysis of scanning electron microscopy (SEM) images (Figure 4.5). Consistent with this etching mechanism, X-ray photoelectron spectroscopy (XPS) characterization showed decreasing amounts of sp^3 oxidized carbons as the etch time was extended, due to the nanopore etching process as well as the reduction of GO during the reaction (Section 4.4.4). Although reduction has been reported to enhance the strength and stiffness of single-layer GO,[6,7] our mechanical data (Section 4.2.2) strongly suggests that nanoporosity is the dominant factor in the mechanical performance of the etched GO sheets investigated herein, as they exhibit dramatic decreases in both strength and stiffness with increasing etch time.

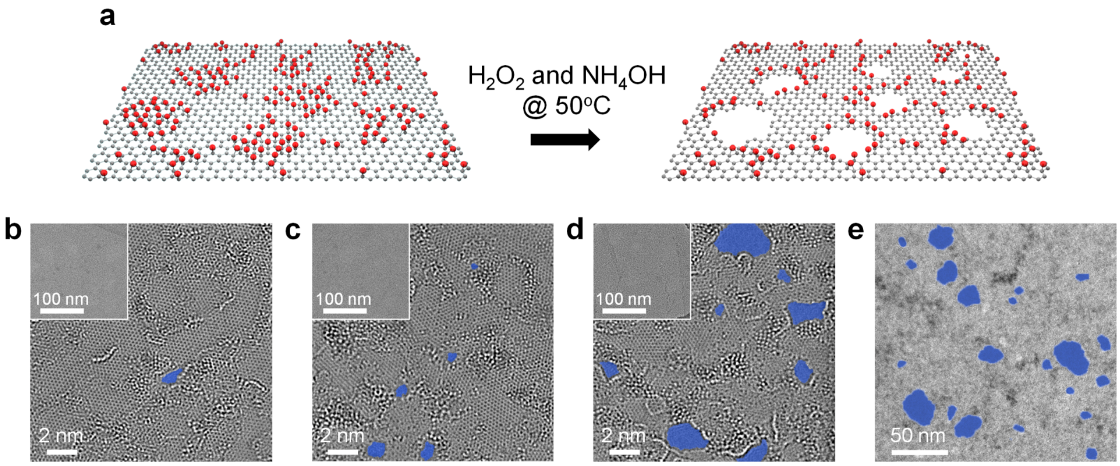

Figure 4.1 (a) Schematic models of pristine and etched GO. Red dots represent sites with oxygenated functional groups, which are preferentially etched, leaving holes on the graphene sheet. (b-d) high-resolution TEM images of the basal plane of a GO sheet (b) before and after being etched for (c) 1 and (d) 3 hours, respectively. Pores are highlighted in blue. Corresponding low-magnification TEM images are shown in the insets. (e) Low-magnification TEM image of 5 hr-etched GO, showing extensive formation of large pores.

4.2.2 Nanomechanical Characterization of Single-Layer Pristine and Etched GO

Prior to nanomechanical testing, pristine and etched GO single-layers were suspended via Langmuir-Blodgett deposition[8] over an array of circular microwells pre-fabricated on a silicon substrate (Section 4.4.5). The center of the membranes was deflected with an atomic force microscope (AFM) single-crystal diamond probe to determine the mechanical properties (Section 4.4.7). Figure 4.2a shows representative force-deflection responses obtained for pristine, 1 hr-etched, and 3 hr-etched GO sheets. As etch time increases, the stiffness and maximum load-bearing capacity of GO substantially decrease due to an increase in porosity, to the extent that 5 hr-etched GO is too weak to suspend on the substrate to reliably test (Section 4.4.8). In all cases, an abrupt increase in deflection occurs as the force drops due to film rupture and material failure. Notably, the maximum deflection to film rupture increases with etch time, consistent with an apparent increase in ductility due to the presence of a network of pores.

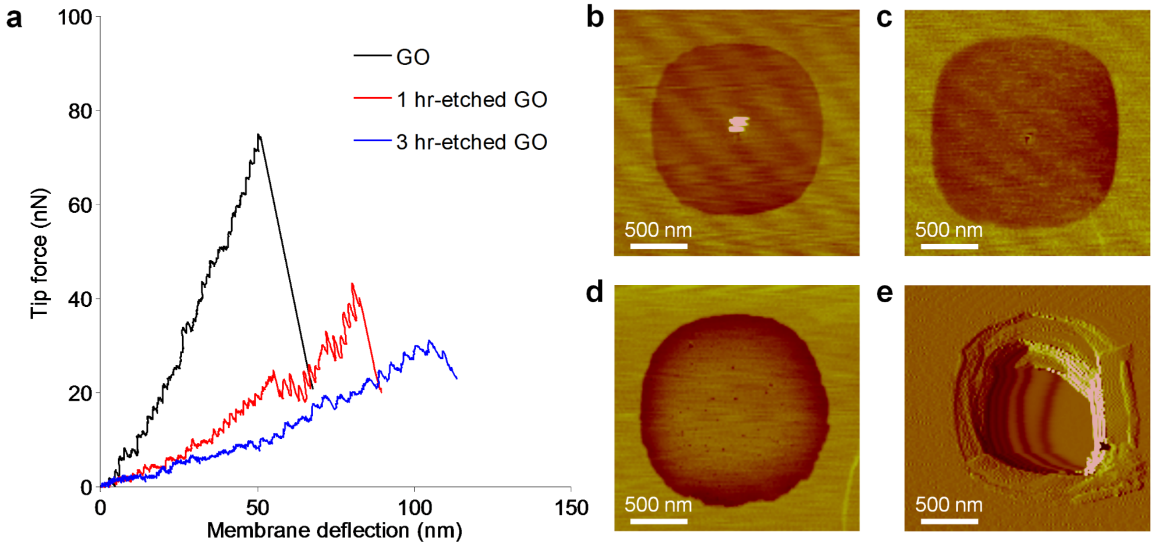

Figure 4.2 (a) Representative force-deflection curves obtained by membrane deflection experiments using a diamond AFM probe, suggesting etched sheets become softer and weaker as etch time increases. The 5 hr-etched GO sheets are too weak to be measured. (b-c) AFM images of ruptured membranes of (b) GO and (c) 1 hr-etched GO after membrane deflection tests. GO etched for 3 hours is significantly more porous (d), and ruptured completely after the test (e).

Representative post-rupture tapping-mode AFM topography scans for the samples (Figure 4.2b-c,e) show an increase in the radius of the puncture with increasing etching time, with catastrophic failure for 3 hr-etched GO membranes. The post-rupture AFM topography scans obtained for pristine GO in this work are in good agreement with previous experiments using the same methodology for GO single-layers with a similar chemical composition.[6] AFM topography scans prior to membrane deflection experiments obtained from 3 hr-etched GO show the presence of nanopores in the membrane, in contrast to scans obtained from pristine and 1 hr-etched GO membranes. These observations, combined with the trends found in force-deflection behavior, confirm the presence of pores on the material tested in nanoscale AFM experiments.

4.2.3 Nanoscale Mechanical properties of Single-Layer Pristine and Etched GO

Given the strong correlation between porosity and etch time that was observed in the HRTEM images of porous GO sheets, it was expected that the nanomechanical properties of GO would decrease with increasing etch time. This is indeed supported by the prestress and elastic modulus values obtained from the elastic analysis of our nanoscale AFM measurements, where the thickness value (h = 0.75 nm) is assumed in accordance with previous literature[9] (Figure 4.8). The pre-stress ($\sigma_o = 0.07 \pm 0.03$ GPa, $\sigma_o = 0.03 \pm 0.01$ GPa, and $\sigma_o = 0.04 \pm 0.02$ GPa for pristine, 1 hr-etched, and 3 hr-etched GO membranes, respectively) decreases substantially as etch time increases. This is presumably caused by the relaxation of the film due to significantly weaker adhesion of the sheet to the wall of the microwells, or increased ductility in the material itself. The elastic modulus of pristine GO membranes obtained from the analysis ($E = 282.8 \pm 20.6$ GPa) is in good agreement with previous literature for GO,[6,10] and exhibits a decrease of approximately an order of magnitude with increasing etch time ($E = 85.0 \pm 12.0$ GPa, and $E = 36.0 \pm 10.9$ GPa for 1 hr-etched and 3 hr-etched GO, respectively).

While GO becomes weaker and more compliant (*i.e.,* less stiff) as nanoporosity increases, its overall ductility (*i.e.,* maximum membrane deflection) increases substantially due to the inclusion of nanopores that facilitate ductile failure. Due to the synthesis method employed in this work, porous GO sheets contain multiple voids that nucleate during etching. As the material is loaded by the AFM tip, these voids coalesce until a crack with a certain critical dimension is formed. At this point, stress concentration effects increase the effective stress around the crack, leading to unstable crack propagation and material rupture for sharp cracks. However, the shape and dimensions associated with individual voids in GO can presumably form blunt cracks which result in ductile failure and endow the material with significant resistance to failure.

Notably, the AFM feedback loop parameters had to be adjusted to significantly reduce the tapping force imparted on the 3 hr-etched GO membranes during tapping-mode AFM topography scans prior to and after film rupture. Without careful consideration of the parameters utilized in this imaging process, the membranes tended to rupture catastrophically during acquisition of the sample topology. This suggests that pores within the 3 hr-etched GO membranes approach a critical size for the material, at which small loads are sufficient to cause abrupt film rupture due to the coalescence of voids inherent to the material. In agreement with this observation, relatively low surface tension forces during deposition ruptured most of the 5 hr-etched GO membranes, suggesting that their pore size exceeded this critical value, rendering them mechanically weak for engineering applications.

4.2.4 Mechanical Properties of Pristine and Etched GO Multilayer Films

While porosity greatly affects the stiffness and strength of GO at the single-layer level, these properties are much less sensitive for bulk multilayer films of porous GO. Previous studies have shown that the stiffness and strength of multilayer GO films is dominated by interlayer load transfer between the constituent sheets, rather than the mechanical properties of the sheets themselves.[11,12] This demonstrates that failure mechanisms in multilayered systems can be significantly different than those observed in single-layer GO sheets. Thus, this motivates the assembly of the relatively weak porous GO sheets into a multilayered structure, with the aim of investigating how single-layer porous GO mechanical properties scale to their bulk films. To fabricate these films, GO or porous GO sheets were stacked together to yield GO and porous GO films, respectively, with thickness of ~7-11 μm (Section 4.4.9). These films were then subjected to uniaxial tensile testing to compare their stiffness and strength against those of a pristine GO film.

Multilayer porous GO films maintained a significant fraction of the multilayer pristine GO film stiffness, compared to single-layer porous GO sheets, which exhibited major reductions in stiffness as mentioned previously (Figure 4.3a and Table 4.2). Notably, 1 hr-etched GO films are 87% as stiff as a pristine GO film, whereas 1 hr-etched GO sheets are only 30% as stiff as a GO sheet. Films comprising 3 hr-etched and 5 hr-etched GO sheets similarly maintained a much higher percentage of their original stiffness (62% and 28%, respectively) than their corresponding single-layer constituents (13% and ~0%, respectively) (Figure 4.3b). Together, these data suggest that both interlayer load transfer and sheet porosity contribute to modulating film stiffness. At low porosity, there are presumably minor changes to interlayer load transfer, resulting in 1 hr-etched GO films with stiffness approaching that of a pristine GO film. At higher porosities, the increasing void spaces within the basal plane of the constituent sheets presumably reduce the interlayer area over which load transfer occurs, and effectively decreases interlayer load transfer, resulting in 3 hr-etched and 5 hr-etched GO films with stiffness below that of a pristine GO film.

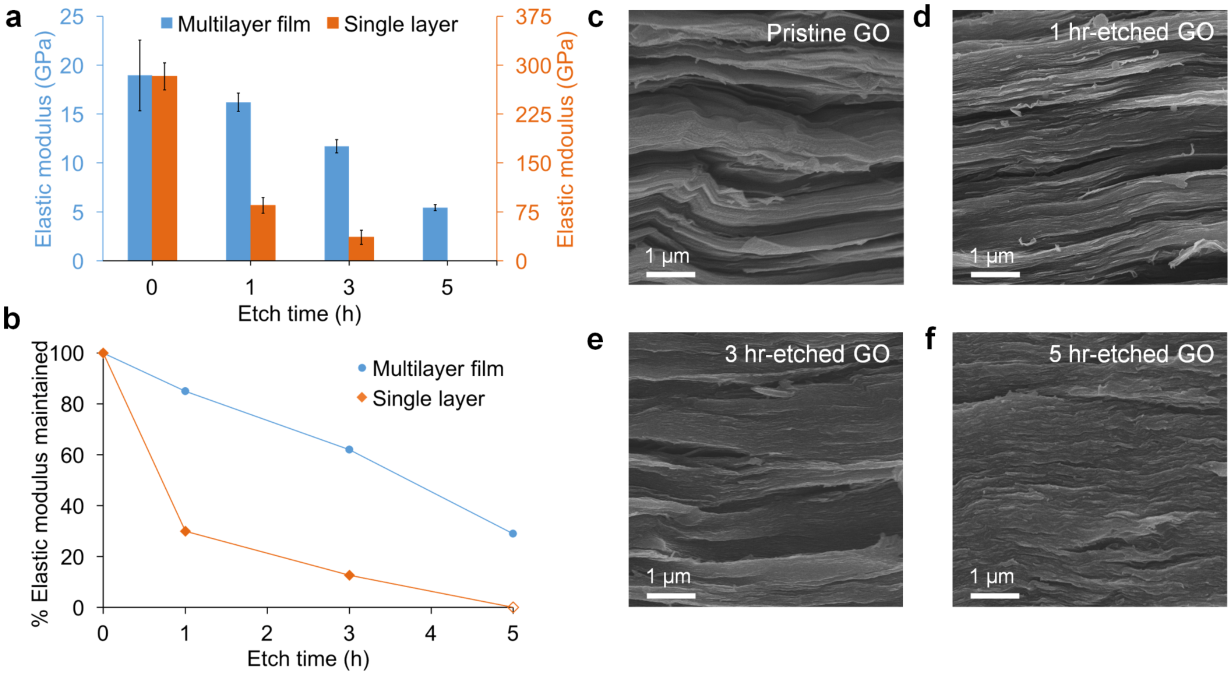

Figure 4.3 (a) Elastic moduli of single-layers and the corresponding multilayer films for pristine and etched GO sheets. (b) Percentage reduction of elastic moduli of GO sheets as etching time increases, showing that multilayer films are much more tolerant to etching than single-layers. (c-f) SEM fractographs of multilayer films of (c) pristine, (d) 1 hr-etched, (e) 3 hr-etched, and (f) 5 hr-etched GO sheets.

Due to their porosity-tolerance, porous GO films also maintain a significant amount of the tensile strength of a pristine GO film (Table 4.2). Among the porous films, 1 hr-etched GO films exhibit the highest tensile strength, which is 65% of the strength of pristine GO paper (Table 4.2, cf. entry 1 and 2). In comparison, 3 hr-etched and 5 hr-etched GO films retain 58% and 30% of the strength of a GO film. The difference in strength between pristine and 1 hr-etched GO films suggests that the tensile strength is initially more sensitive than the elastic modulus to the porosity of the constituent sheets. This is presumably due to decreased interlayer load transfer and the weakening of the porous GO sheets, which both contribute to lowering tensile strength. In addition, the increased porosity in 3 hr-etched GO may lead to stress concentration with the sheet, resulting in local failure and interlayer sheet pullout. However, at higher levels of porosity, the strength maintained in porous GO films becomes comparable to the stiffness maintained. This is in stark contrast to the corresponding single-layer porous GO sheets, which become too weak to test after a 5-hour etch time (Section 4.4.8). These results imply that the multilayer structure renders the tensile strength of porous GO films to be more tolerant to sheet porosity.

As mentioned previously, we predicted that interlayer load transfer between sheets could lead to porosity-tolerant mechanical properties in a multilayer film. To investigate the mechanism behind the ability of porous GO films to maintain significant stiffness and strength, the fracture surfaces of the porous GO films were imaged by SEM to analyze the interlayer packing of porous GO films. Notably, denser packing of sheets was observed with increased etch time (Figure 4.3c-f). While pristine GO films exhibit uneven fracture surfaces with numerous interlayer voids (Figure 4.3c), smoother fracture cross-sections with fewer voids are observed as the etch time increases (Figure 4.3d-f). In particular, 5 hr-etched GO films exhibit extremely smooth fracture surfaces, with very few interlayer voids visible (Figure 4.3f), suggesting that highly porous sheets can pack together more efficiently. These observations suggest that the manner of sheet stacking changes, which may lead to differences in interlayer load transfer and contribute to the porosity-tolerance of multilayer porous GO films.

4.2.5 Mechanical Properties of Mixed Pristine and Etched GO Multilayer Films

To address the tradeoff between the mechanical properties and interlayer packing of 5 hr-etched GO sheets, we predicted that co-assembly of 5 hr-etched and pristine GO sheets into a multilayered structure would allow for cooperative interactions and lead to excellent stiffness and strength. To test this theory, a series of mixed films containing 10, 25, 50, 75, and 90 wt % of 5 hr-etched GO sheets were fabricated and subjected to uniaxial tensile testing (Section 4.4.9). As expected, the tensile strength of the 10:90 mixed paper (10 wt % 5 hr-etched GO, 90 wt % pristine

GO) remained similar to that of a GO film (Table 4.2, cf. entry 1 and 5), confirming that the detrimental effects of porosity can be mitigated by the addition of GO sheets. Indeed, mixed films containing only 10 wt % of GO sheets maintain an impressive 62% of the strength of a pristine GO film, while a pure 5 hr-etched GO film retains only 30% (Table 4.2, cf. entry 1 and 5).

Based on the improved tensile strengths of the mixed films, we would expect similar results for the elastic modulus. Surprisingly, a nearly two-fold increase in the elastic modulus of the 10 wt % mixed film was observed (35.1 ± 1.7 GPa; compared to 19.0 ± 3.6 GPa for a pristine GO film), suggesting that the addition of highly porous sheets enhances the stiffness of the multilayer assembly. This stiffening effect was also observed in the 25 wt % mixed film, which exhibited a 1.7-fold increase in elastic modulus (31.6 ± 1.8 GPa) over that of the pristine GO film, despite a quarter of the sheets being highly porous. Remarkably, the 75 and 90 wt % mixed films were nearly as stiff as a pristine GO film (Table 4.2, cf entry 1, 8, and 9). In comparison, a pure 5 hr-etched GO film maintains only a quarter of the stiffness of a pristine GO film (Table 4.2, cf. entry 1 and 4). Together, these results support our hypothesis that combining pristine and 5 hr-etched GO sheets results in a synergistic enhancement of stiffness and strength.

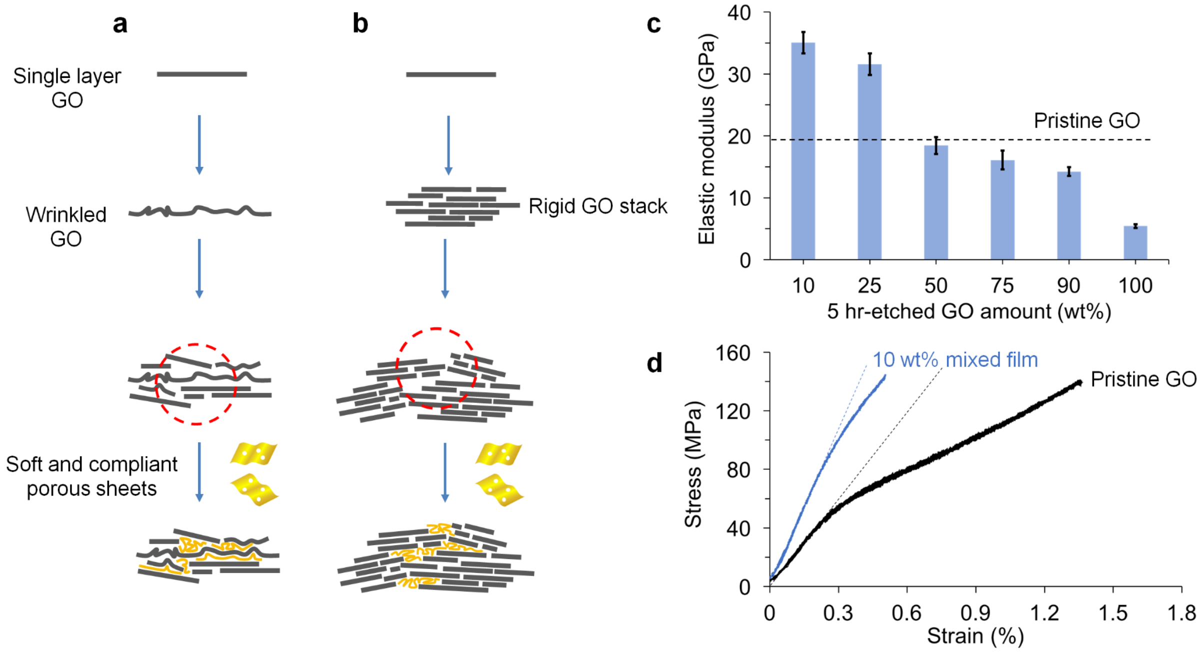

Figure 4.4 (a) Multilayer films of pristine GO sheets are unlikely to have uniform packing density due to the following dilemma. First, GO sheets are easily wrinkled during processing, which would disrupt the packing of neighboring sheets. Second, wrinkle-free sheets would stack into platelets that are drastically more rigid, and less compliant for further packing. Both scenarios result in voids in the multilayer films, which can become stress concentrators to degrade the mechanical properties. Since porous GO sheets are much softer, they effectively serve as a binder for more compliant packing in the multilayer films, leading to higher stiffness. (b) Elastic moduli of mixed multilayer films with various fractions of 5 hr-etched GO. (c) Representative stress-strain curves of a pristine GO film and another with 10 wt % of 5 hr-etched GO. Dashed lines represent the calculated elastic moduli of the films. While a pristine GO film becomes less stiff as strain increases, the 10 wt % mixed film better maintains its stiffness, as the porous sheets strengthen interlayer interactions and make the film more resistant to deformation.

4.2.6 Proposed Stiffening Mechanism in Mixed Multilayer Films

Based on the changes in interlayer packing observed for porous GO films, we hypothesized that the addition of 5 hr-etched GO sheets could also affect the packing of GO sheets in the mixed films. Specifically, the more compliant porous sheets can presumably conform and pack into interlayer voids between GO sheets, effectively acting as a binder (Figure 4.4a). This would result in fewer void spaces and enhanced interlayer interactions, leading to improved load transfer and the significant stiffening observed in our mechanical tests.

Stress-strain curves of a pure GO film and a 10 wt % mixed film provide further evidence of the enhancement in interlayer interactions (Figure 4.4c). In a pure GO film, stiffness decreases with increasing strain as GO sheets slide past each other and the film experiences plastic deformation.[5] In contrast, the stiffness of a 10 wt % mixed film remains similar up to film fracture, suggesting that 5 hr-etched GO sheets can effectively bind GO sheets together, making the film more resistant to deformation. The strengthening of interlayer interactions by soft porous sheets should also enhance tensile strength, as observed in our mechanical experiments. However, this enhancement is not as significant as it is for stiffness, as the inclusion of weaker 5 hr-etched GO sheets facilitates failure of the constituent sheets and lowers the overall strength of the film. Promisingly, there is little reduction in the tensile strength of 25-90 wt % mixed films (Table 4.2 and Figure 4.9), implying that increasing interlayer interactions may counter the effect of using weaker constituents.

4.3 Conclusion

Using GO sheets as a model 2D nanomaterial, we have investigated how porosity influences the scaling of material properties from the single-layer level to bulk multilayer films. While porosity drastically reduces the stiffness and strength of individual GO sheets, these properties become significantly more porosity-tolerant when the sheets are assembled into a multilayer laminated structure. Notably, the co-assembly of pristine sheets and a small percentage of soft, highly porous sheets with near-zero elastic modulus leads to stiffening of the resulting multilayer film. This stiffening is attributed to the ability of the porous sheets to effectively act as a binder, thereby enhancing interlayer interactions and load transfer within mixed films. Our work demonstrates the use of compliant constituents to stiffen and reinforce multilayer laminated films, a strategy that can also be applied to other systems based on 2D materials.

4.4 Materials and Methods

4.4.1 Materials and Instrumentation *(HRTEM work was carried out by Hun Park)*

Unless otherwise stated, all reagents were used as received. Graphite powder (grade 2012) was purchased from Asbury Carbons Inc. (Asbury, NJ). Potassium permanganate was purchased from Sigma-Aldrich Co., LLC (Milwaukee, W). Concentrated sulfuric acid (H_2SO_4) and hydrochloric acid (HCl; 37 wt % in water) were purchased from Junsei Chemical Co., Ltd (Japan). Hydrogen peroxide (H_2O_2; 30 wt % in water) and ammonium hydroxide solution (NH_4OH; 30% NH_3 basis) were purchased from Sigma-Aldrich Co., LLC (Milwaukee, WI) and refrigerated during storage. Ultrapure deionized water (resistivity 18.2 MΩ cm) was obtained from a Direct Q3 system (Millipore Inc., Billerica, MA). Silicon wafers (4" diameter, N-type) with 285 nm oxide thickness were purchased from Graphene Supermarket (Calverton, NY).

X-ray photoelectron spectroscopy (XPS) was performed using a Thermo Scientific Theta Probe ARXPS (Al Kα radiation, hν = 1486.6 eV; Thermo Fisher Scientific Inc., West Palm Beach, FL) equipped with an electron flood gun. Pristine and porous GO films for XPS analysis were prepared by vacuum-assisted filtration of pristine and poros GO solution, respectively, with a hydrophilic polyvinylidene fluoride (PVDF) membrane (HVLP04700, 0.45 μm pore size, Millipore Inc., Billerica, MA). Raman spectroscopy measurements were collected on a NRS-3100 Raman spectrometer (Jasco Inc., Easton, MD) with 514 nm laser excitation.

High-resolution transmission electron microscopy (HRTEM) images were taken using an aberration-corrected FEI Titan 80-300 (FEI Co., Hillsboro, OR) at an accelerating voltage of 80 kV. The spherical aberration was set to ca. -2.231 μm and images were taken at a defocus value of ca. +10 nm. Scanning electron microscopy (SEM) images of suspended and supported sheets were taken using a FEI NovaNano 600 microscope (FEI Co., Hillsboro, OR) and a Hitachi S-4800 microscope (Hitachi High-Tech. Co., Japan), respectively. SEM images of multilayer films were obtained using a Hitachi SU8030 microscope (Hitachi High-Tech. Co., Japan). Atomic force microscopy (AFM) images of suspended or supported sheets were obtained in tapping mode using a Park XE-70 AFM system (Park Systems Co., South Korea) and a Veeco Dimension 3100 AFM system (Plainview, NY), respectively.

Water contact angles of the silicon substrates were measured using a VCA Optima contact angle instrument (AST Products Inc., Billerica, MA) by dropping 4 μL of ultrapure deionized water onto the substrate, with measurements taken at three different locations on each substrate.

4.4.2 Synthesis of GO *(This work was carried out by Hun Park)*

Each batch of graphite oxide was prepared using a modified Hummers method. Briefly, graphite (5 g) and concentrated H_2SO_4 (187 mL) were stirred together and cooled to 0 °C using an ice bath. Potassium permanganate (25 g) was slowly added to this mixture, with the temperature kept below 10 °C. The reaction mixture was then transferred to a 35 °C water bath and stirred for 6 h. Next, the mixture was transferred to an ice bath, and ultrapure deionized water (250 mL) was slowly added, taking care to keep the temperature below 55 °C. Additional ultrapure deionized water (500 mL) was then added, followed by the addition of H_2O_2 (10 mL) until the solution became orange brown. The resulting graphite oxide was filtered and washed with HCl (2 L of a 1M solution) over a cellulose membrane (Whatman filter paper, 2.5 μm pore size, Millipore Inc., Billerica, MA) overnight. The filter cake was dispersed in acetone (2 L), then filtered and washed with acetone (4 L) over a cellulose membrane overnight. This final graphite oxide filter cake was dispersed in ultrapure deionized water with mild sonication for 30 min. Any residual unexfoliated graphite oxide was removed by centrifuging at 1,028 rcf for 30 min using a Gyrozen 1508R centrifuge (Gyrozen, South Korea), with the precipitate discarded. The final dispersions contained appromixately 2 mg mL^{-1} of graphene oxide (GO).

4.4.3 Synthesis of Etched GO *(This work was carried out by Hun Park)*

Etched GO was produced from the as-synthesized GO dispersions. Briefly, NH_4OH (0.5 mL) and H_2O_2 (0.5 mL) were added to the GO dispersion (10 mL; 2.0 mg mL^{-1}). Subsequently, the mixture was placed in an oil bath at 50 °C and kept under magnetic stirring at 30 rpm for a given time (1, 3, or 5 h). After the etching reaction, the excess reactants and by-products in the porous GO solution were separated by centrifuging at 16,421 rcf for 90 min, and removed by discarding the supernatant. The precipitate was diluted with ultrapure deionized water (5 mL) and then further purified by dialysis (Spectra Dialysis Membrane, MWCO: 6,000-8,000) against an excess amount of ultrapure deionized water (1 L) for at least 3 days. During the dialysis, the ultrapure deionized water was exchanged every 5 hours for the first two days, and every 10 hours thereafter. The resulting dispersions (~2.8-3.5 mg mL^{-1} depending on the reaction time) were diluted to 2.0 mg mL^{-1} by adding ultrapure deionized water. SEM images of the sheets and the corresponding sheet size distributions (Figure 4.5) show that there are minor differences in the average sheet size after the nanopore etching reaction.

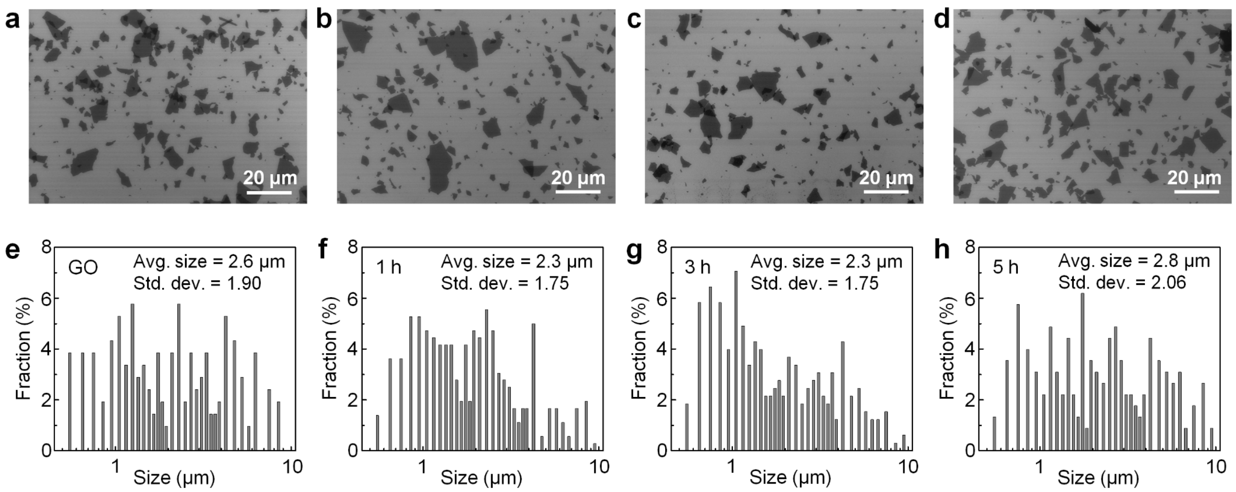

Figure 4.5 Representative SEM images of a) pristine, b) 1 hr-etched, c) 3 hr-etched, and d) 5 hr-etched GO sheets. Corresponding size distributions of e) pristine, f) 1 hr-etched, g) 3 hr-etched, and h) 5 hr-etched GO sheets, obtained from SEM image analysis. The average sheet size does not change significantly with etch time, suggesting that the nanopore etching process does not initiate at the sheet edges.

4.4.4 XPS and Raman characterization of Pristine and Etched GO *(This work was carried out by Hun Park)*

The chemical compositions of the pristine and etched sheets were monitored by X-ray photoelectron spectroscopy (XPS), confirming that the amount of oxidized carbons decreases as etch time is extended. As shown in the C1s XPS scans in Figure 4.6a, the intensity of the peak corresponding to graphitic carbon atoms (284.5 eV) increases with etch time, while that of the peak corresponding to contributions from the oxidized carbon atoms[13-15] decreases. This can be attributed to the generation of nanopores at the sp^3 oxidized domains of GO, which effectively etches away oxidized carbons. In addition, the ring-opening of GO epoxide groups by ammonia during the etching process further contributes to the decrease in oxidized carbons.[6] This reaction effectively removes epoxide groups and produces vicinal amine and hydroxyl species that can react further, leading to reduction of the carbon backbone.[6] The reduction of GO during the etching process is further supported by the Raman spectroscopy results, which show that the ratio of the intensity of the D and G peaks (I_D/I_G) remains constant (Figure 4.6b). While this ratio would be expected to decrease as the oxidized domains are etched away,[2] the observed lack of change is presumably due to the opposing effect of GO reduction, which has been suggested to restore portions of the GO graphitic framework and increase the I_D/I_G ratio.[16]

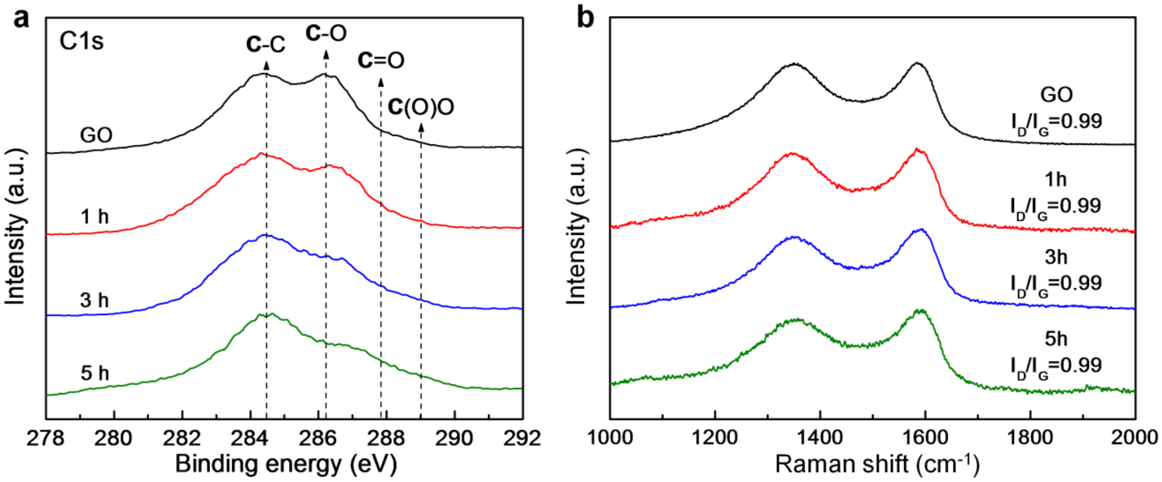

Figure 4.6 (a) C1s XPS scans of pristine and etched GO, showing a decrease in oxidized carbons with increasing etch time. (b) Raman spectra of pristine and etched GO. The I_D/I_G ratio remains constant with etch time.

4.4.5 Preparation of Silicon Substrates with Microwells *(This work was carried out by Dr. Fan Zhou)*

Si substrates patterned with arrays of circular microwells (1.76 μm diameter and 4 μm depth) were fabricated by photolithography and deep reactive-ion etching (DRIE). A 1.2 μm-thick photoresist layer (S1813 positive photoresist manufactured by Dow Electronic Materials Microposit, catalog number: DEM-10018348, Capitol Scientific, Inc, Austin, TX) was spin-coated onto the Si wafer at 4000 rpm using a spin coater (Cee 200X, Brewer Science, Inc., Rolla, MO). Following a 1 minute soft bake at 100 °C on a hot plate, the wafer was exposed to UV light (365 nm, 18 mW cm^{-2}) for 4 seconds on the Mask Aligner instrument (Suss MABA6, SÜSS MicroTec

AG, Garching, Germany). After exposure, the wafer was developed in a MF 319 developer (manufactured by Dow Electronic Materials Microposit, catalog number: DEM-10018042, Capitol Scientific, Inc, Austin, TX) for 60 seconds. Spin rinsing was carried out with ultrapure deionized water (500 mL) for 30 seconds at approximately 300 rpm, followed by a 60 second spin dry at 3000 rpm.

The resulting photoresist-masked silicon wafer was then subjected to microwell etching using a DRIE machine (STS LpX Pegasus, SPTS Technologies Ltd, San Jose, CA). After etching, the remaining photoresist was removed using acetone, and the wafer was cleaned using isopropanol and ultrapure deionized water. This wafer was then cleaved into smaller substrates to be used in the Langmuir-Blodgett (LB) deposition and subsequent membrane deflection experiments.

Prior to LB deposition, the substrates were cleaned using the following procedure: 1) submerged in 2 mL of a 3:1 v/v mixture of conc. H_2SO_4:30 wt % H_2O_2 and heated in a Biotage (Uppsala, Sweden) SPX microwave reactor (software version 2.3, build 6250) at 180 °C for 45 min, 2) sonicated for 10 min each in ultrapure deionized water (~10 mL), methanol (~10 mL), and ultrapure deionized water (~10 mL), respectively, 3) dried under a flow of nitrogen for 1 min, and 4) treated with O_2 plasma (5 min at 190 W and 10-15 mTorr O_2) in a South Bay Technology Inc. (San Clemente, CA) Model PC-2000 plasma cleaner. The yield of intact suspended GO membranes is strongly dependent on the water contact angle of the substrate[6]. Therefore, after this cleaning process, the substrates were left under ambient conditions and their water contact angle was monitored until the desired values were reached (an optimal water contact angle of ~70° yielded both intact films and high coverage of GO sheets) prior to LB deposition (Section 4.4.6). The water contact angle of the freshly plasma-treated substrates was close to 0°, gradually increasing over time, and reaching a maximum of ~95° approximately one week after plasma treatment.

4.4.6 Langmuir-Blodgett Assembly of Pristine and Etched GO Single-Layers

To prepare suspended single-layer pristine and etched GO membranes for the AFM membrane deflection experiments, the Langmuir-Blodgett (LB) assembly method was employed.[8] The as-prepared aqueous pristine or porous GO dispersion was diluted with MeOH to a mixture of 5:1 v/v MeOH:ultrapure deionized water. The Nima technology (Espoo, Finland) model 116 trough was cleaned with acetone, and filled with ultrapure deionized water. Generally, the pristine or porous GO solution (300-480 μL) was spread onto the water surface dropwise at a rate of 100 μL min^{-1} using a glass syringe, forming a single-layer film on the surface. A tensiometer attached to a Wilhelmy plate was used to monitor the surface pressure. The film was allowed to equilibrate for at least 20 min after spreading, and then compressed by barriers at a speed of 100 $\text{cm}^2\ \text{min}^{-1}$. Near the onset of the surface pressure increase, the pristine or porous GO single-layer was transferred by vertically dipping the substrate into the trough and slowly pulling it up at a rate of 2 mm min^{-1}. Substrates with a water contact of angle of ~ 70° were used to ensure deposition of intact suspended membranes.

4.4.7 Atomic Force Microscopy Membrane Deflection Tests *(This work was carried out by Rafael A. Soler-Crespo)*

A single-crystal diamond probe (catalog number: ART D160, K-TEK Nanotechnology, Wilsonville, OR) was used to indent at the membrane center with an AFM (Dimension 3100, Veeco, Plainview, NY). The stiffness of the cantilever (k = 3.01 N m^{-1}) was calibrated using a standard cantilever (CLFC-NOBO, Bruker).[17] The tip radius of the AFM probe (R = 15 nm) was measured by an FEI NovaNano 600 SEM. All experiments were performed at room temperature and 16% humidity inside a customized environmental chamber. A constant deflection rate of 1 μm s^{-1} was used in all tests. Pre-testing and post-mortem AFM scans were taken for each specimen using tapping AFM imaging, with a tapping amplitude of 1 nm, under frequency control conditions. A scan rate of 0.5 Hz was used for all images in an imaging window of 2 μm.

For a suspended, circular, linear elastic membrane under a central load, the force vs. deflection response can be approximated as[18]

$$F = \pi\sigma_0 h\delta + \frac{Eh}{q^3 a^2}\delta^3 \qquad 4.1$$

where F is the applied force, δ is the membrane center deflection, h is the effective thickness of the specimen (Section 4.4.8), σ_0 is the pre-stress in the membrane, a is the membrane radius, E is the elastic modulus, and q is a dimensionless constant defined as $q = (1.05 - 0.15v - 0.16v^2)$-1 where v is the Poisson's ratio. According to previous density functional-based tight-binding (DFTB) calculations,[6,7] the Poisson's ratio of the systems studied here was taken as 0.2. We defined specific guidelines to select the fitting region on the raw data (Section 4.4.8) to achieve consistency when fitting the linear elastic behavior of different samples.

4.4.8 Elastic Analysis of Membrane Deflection Results *(This work was carried out by Rafael A. Soler-Crespo)*

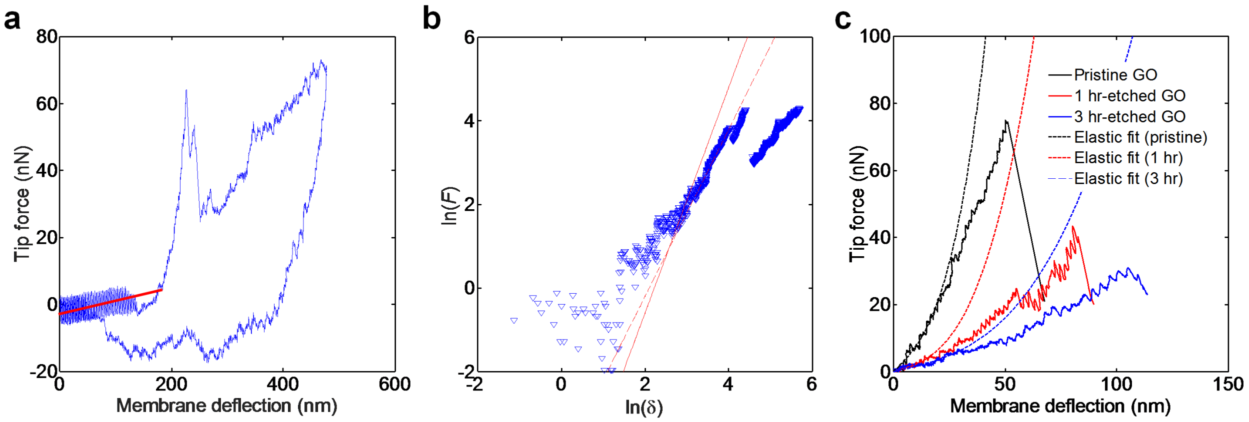

Figure 4.7 a) Selection of first point for fitting force-deflection curves. This point corresponds to the deflection when the tip effective force, post-membrane adhesion (*i.e.,* after the cantilever straightens after snapping into the membrane), matches the average force measured during tip approach. (b) Selection of last point for fitting force-deflection curves, when the experimental data deviates from the slope (*i.e.,* slope of 3 in the ln δ term) given by Equation 4.1. (c) Representative data fit for the force-deflection curves shown in Figure 4.2a, using the criteria outlined herein.

The analysis of AFM force-deflection curves for GO single-layers with different porosity necessitates establishing a consistent set of criteria to determine the region of the curve which will be fit using the linear elastic force-deflection model.[18] The selection of the first point of the fitted region, which corresponds to the point of contact in which the membrane has undergone no applied load, is selected to be the point at which the force in the AFM cantilever matches the average force measured as the tip approaches the membrane, as shown in Figure 4.7a. By selecting this point, adhesive effects are eliminated given that the cantilever has straightened after snapping into the membrane, thereby making the effective force in the cantilever zero. The final point of the fitted region must correspond with the first deviation of linear elasticity during membrane deflection.

This selection can be guided by manipulating the linear elastic, force-deflection model into the form

$$\ln F \approx 3\ln\delta + \ln\left(\frac{Eh}{q^3 a^2}\right) \qquad 4.2$$

which is valid only for large membrane deflections (Figure 4.7b). Here, F is the applied force, δ is the deflection at the center of the membrane, E is the elastic modulus of the membrane, h is the membrane thickness (taken as 0.75 nm[9]), a is the membrane radius (here, a = 1760 nm according to SEM and AFM characterization) and q is a dimensionless parameter, given by $q(v) = (1.05 - 0.15v - 0.16v^2)^{-1}$. In this last expression, v is the Poisson's ratio of the membrane, taken to be 0.16 according to previous literature.[6] After selection of the two fit extremum, experimentally obtained force-deflection curves are fit (Figure 4.7c) to the linear-elastic model with an in-house MATLAB code (Version 2012a, MathWorks).

Table 4.1 Elastic modulus and prestress obtained in our experiments based on linear elastic analysis from force-deflection curves.

System	Modulus (GPa)	Prestress (GPa)
GO	283 ± 21	0.07 ± 0.03
1 hr-etched GO	85 ± 12	0.03 ± 0.01
3 hr-etched GO	36 ± 11	0.04 ± 0.02

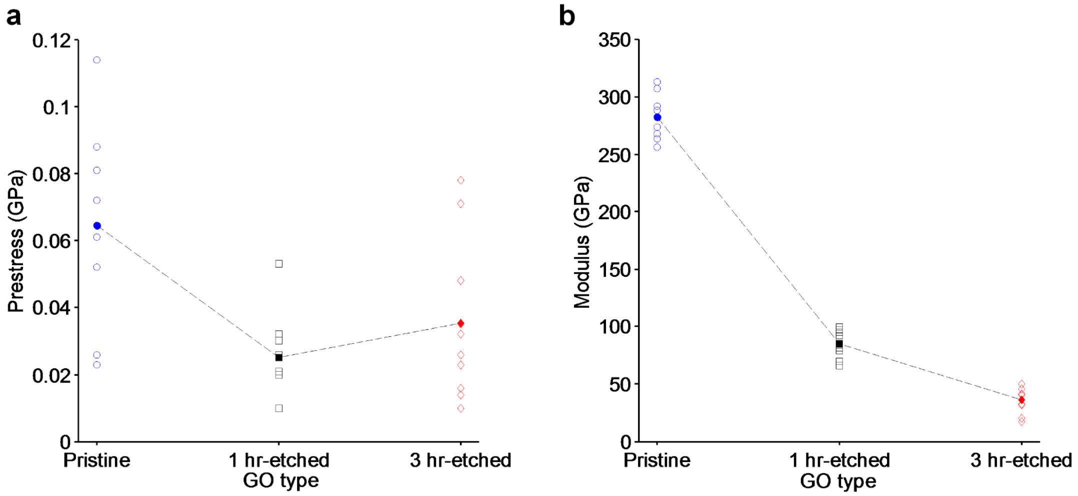

Figure 4.8 (a) Summary statistics plot for the elastic modulus as a function of GO etching time. (b) Summary statistics for prestress in GO as a function of etching time. In (a) and (b), hollow symbols represent experimental data points while solid symbols represent average values. A dashed line is used to connect average values in (a) and (b) to show an overall decrease in properties with increasing etching time.

A summary of the results obtained by fitting the force-deflection curves is shown in Table 4.1 and Figure 4.8. As expected, the elastic modulus of the material is strongly dependent on the total porosity of the sample, while prestress is seemingly independent of etching time. In addition, and in agreement with the stress concentration behavior of defects, the average rupture force decreases monotonically with increasing etch time, as shown in Figure 4.7c. Notably, 5 hr-etched GO single-layers were found to rupture during LB deposition due to the substantial pore size in the membranes, which led to significant stress concentration and weakening of the material. While a low number of intact membranes were found, these did not exhibit mechanical properties consistent with 5 hr-etched GO single-layers ($E = 117 \pm 23$ GPa and $\sigma_0 = 0.05 \pm 0.03$ GPa), and these results were not included in our mechanical analysis.

4.4.9 Fabrication and Mechanical Analysis of Multilayer Films

GO and porous GO films were prepared via vacuum-assisted filtration of aqueous dispersions of GO or porous GO, respectively. Mixed films were similarly fabricated by vacuum-filtering pre-mixed aqueous dispersions containing pristine and 5 hr-etched GO sheets in varying weight ratios. All films were prepared from 10 mL of a 2 mg mL^{-1} dispersion, and were filtered over mixed cellulose membranes (MF-Millipore membrane filter, hydrophilic, 0.45 µm pore size, Millipore Inc., Billerica, MA).

Mechanical properties of the films were evaluated under uniaxial tension using an ElectroForce 5500 mechanical test instrument (TA Instruments Inc., New Castle, DE), equipped with a 50 lbf load cell (TA Instruments Inc., New Castle, DE). Samples for testing were cut from films into rectangular strips (approximately 3 mm wide and 24 mm long) by compression with a razor blade. Sample width and length were measured by digital calipers. Each end of the sample was fixed to end tabs with a two-part epoxy glue, with the end tabs clamped by the instrument grips. Without the use of end tabs, samples typically broke near the clamp due to stress concentration within the strip. Prior to testing, a pre-stress of 0.1 N was applied to all samples. A strain rate of 0.005 mm/min was used for testing, and 3-5 strips were analyzed for each film. Elastic modulus was calculated from the slope of the linear-elastic portion of the stress-strain curve, and tensile strength was the maximum stress obtained. Based on this analysis, the results of the tensile tests are summarized in Table 4.2. After mechanical testing, sample thickness was measured from the fracture cross-section using a FEI NovaNano SEM 600 (FEI Co., Hillsboro, OR). As thickness varies throughout the films, an average of 27 thickness measurements was taken for each sample.

Table 4.2 Measured elastic modulus and tensile strength of pristine, etched, and mixed GO multilayer films. The notation 10:90 indicates a composition of 10 wt % 5 hr-etched GO and 90 wt % pristine GO.

Entry	System	Elastic modulus (GPa)	Tensile strength (MPa)	Fracture strain (%)
1	GO	19.0 ± 3.6	138 ± 11	1.4 ± 0.1
2	1 hr-etched GO	16.6 ± 1.7	90 ± 29	1.0 ± 0.4
3	3 hr-etched GO	11.7 ± 0.7	80 ± 5	0.9 ± 0.1
4	5 hr-etched GO	5.4 ± 0.3	42 ± 16	1.0 ± 0.4
5	10 wt %	35.1 ± 1.7	119 ± 27	0.4 ± 0.1
6	25 wt %	31.6 ± 1.8	98 ± 26	0.4 ± 0.1
7	50 wt %	18.4 ± 2.8	97 ± 11	0.7 ± 0.2
8	75 wt %	16.1 ± 1.5	87 ± 14	0.6 ± 0.1
9	90 wt %	14.2 ± 0.8	85 ± 7	0.7 ± 0.0

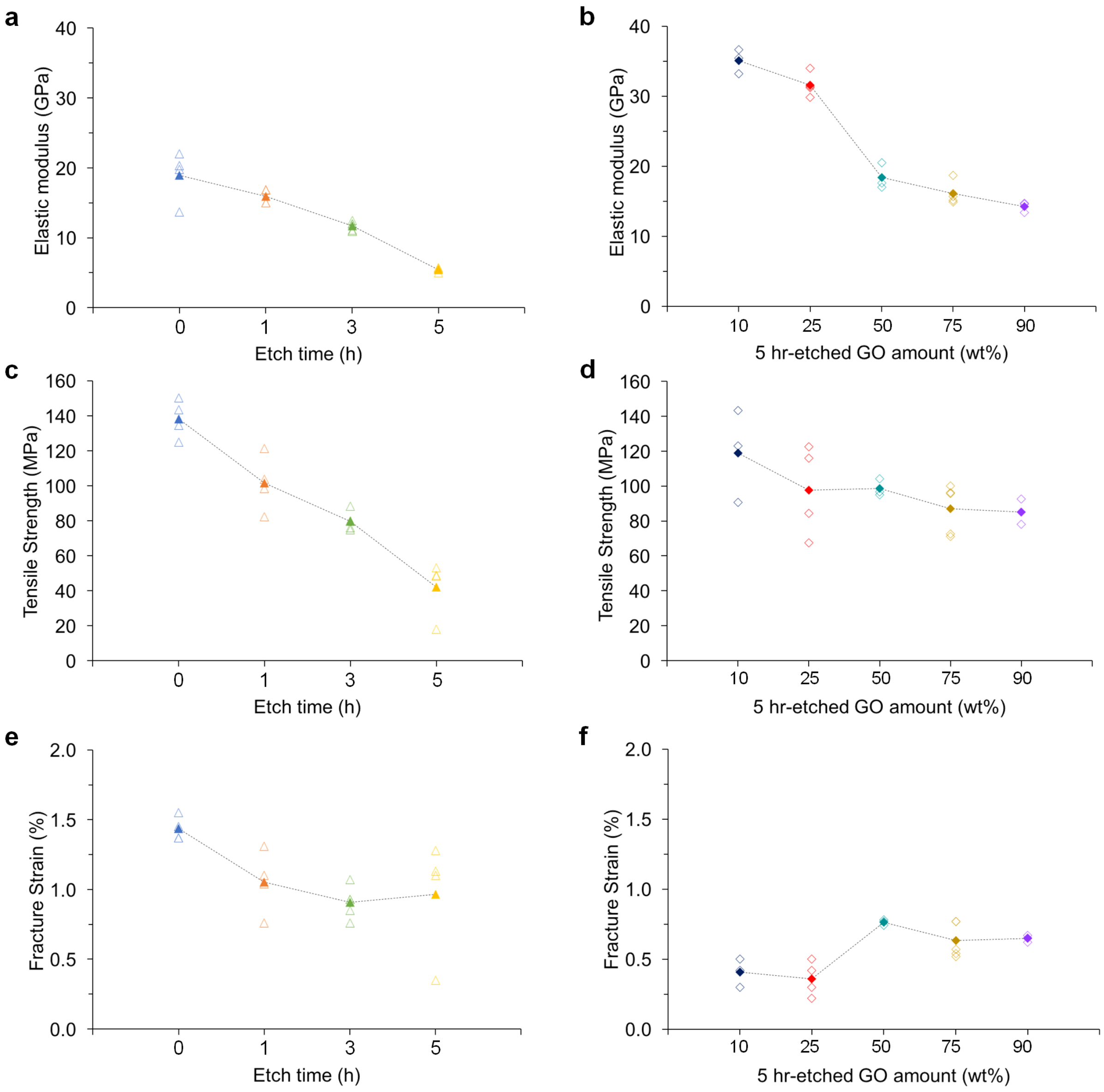

Figure 4.9 Summary statistics of the (a,b) elastic moduli, (c,d) tensile strengths, and (e,f) fracture strains of non-mixed and mixed films as a function of GO etching time (a,c,e) or film composition (b,d,f). Compared to non-mixed films, mixed films maintain a greater percentage of their original stiffness and strength as the overall porosity of the constituents increases. In (b), (d), and (f), the notation 10:90 indicates a composition of 10 wt % 5 hr-etched GO and 90 wt % pristine GO. Hollow symbols represent experimental data points while solid symbols represent average values. A dashed line is used to connect average values to show overall trends.

Chapter 5

Conclusions and outlook

5.1 Conclusion

As discussed in Chapter 1, the large discrepancy in mechanical properties between carbon nanomaterials and their macroscopic composites is a major challenge that must be overcome to achieve their practical use in structural materials. To address this challenge, much of the work in the field of carbon nanomaterial-based composites has focused on improving the mechanical strength and stiffness of macroscopic composites, using design principles derived from the structure of strong and tough biomaterials. In addition to such macroscopic studies, this thesis has shown that a mechanistic understanding of how mechanical properties originate from the chemical structure and interactions of the nanoscale constituents is key to developing nanocomposite design principles that enable mechanical properties to be enhanced in novel ways, such as the crack-bridging toughening mechanisms and the stiffening effect of porous sheets discussed herein. To this end, we have shown that GO mechanical properties at both the single and multilayer level are highly tunable through its chemical structure and interfacial interactions, attractive qualities that make GO a promising and versatile building block for macroscopic nanocomposites.

Importantly, our results highlight the importance of understanding the surface chemistry and structural features of GO for enhancing its mechanical properties at both the single and multilayer level. In Chapter 2, we discussed the critical role of chemical structure (*i.e.,i.e.,* surface functionalization and functional groups) in modulating GO mechanical properties at the single-layer level, and showed that the nanomechanically-activated transformation of GO epoxide groups to ethers provides an intrinsic toughening mechanism in GO sheets via bridging of in-plane cracks at the atomic level. In Chapter 3, inspired by the intrinsic toughening mechanism of GO via atomic scale crack bridging, we introduced an ultrathin layer of polyvinyl alcohol (PVA) to bridge larger areas of a GO sheet, effectively creating an extrinsic crack bridging mechanism and enabling microscale crack bridging. By matching the local chemical domains of GO with PVA chains of appropriate size to enable extensive hydrogen bonding interfacial interactions, we achieved toughness comparable to single-layer graphene, and an impressive three-fold increase in the load-bearing capacity of GO. In addition, we demonstrated the viability of extending this toughening mechanism to a bilayer GO-PVA system, suggesting that nanoscale GO modified with an atomically thin layer of polymer is a promising pathway towards achieving tougher constituents for the fabrication of macroscopic composites. In Chapter 4, we showed that single-layer sheet porosity, an inherent structural aspect of GO, surprisingly enhances the stiffness of multilayer GO films, as porous sheets can achieve more compliant packing within the film and effectively serve as a binder to strengthen interlayer interactions.

5.2 Outlook

The findings in this thesis provide represent fundamental design principles for developing stiff and tough carbon nanomaterial-based composites at the nanoscale. To extend this knowledge to the design and assembly of macroscopic composites, the key challenges that must be addressed are: 1) the development of novel fabrication techniques to scale up carbon nanomaterials into structural materials, and 2) further investigation of how mechanical properties scale from the nano- to the macroscale. Possible strategies that build upon the knowledge in this thesis and address these points are outlined below.

This thesis presents a strategy derived from the Langmuir-Blodgett (LB) technique to fabricate nanoscale GO-based materials with precise control over structure and interfacial interactions. However, this method is time consuming and not optimal for scaling up the production of carbon nanomaterial-based composites. Moreover, the LB technique alone is inadequate to mimic the complex hierarchical structures and interfacial interactions of natural nanocomposites in synthetic materials. As such, novel fabrication strategies that are scalable and offer simultaneous control over structure and interfacial interactions at multiple length scales must be developed. Among scalable processes, layer-by-layer (LbL) assembly[1,2] stands out because it achieves precise control at smaller length scales (e.g., the nanoscale) and allows for relatively fast bottom-up assembly of structures via interfacial interactions. For example, Hu *et al.*[3] demonstrated that combining spin coating and layer-by-layer assembly to co-assemble ultra-thin layers of silk fibroin and GO resulted in macroscopic composite films with high stiffness and toughness. However, LbL assembly offers limited control over the composite structure, as it results in a singular type of structure (*i.e.,i.e.,* a laminated, layered material). To achieve more structurally complex composites, a potential solution is to integrate multiple existing processes that offer control over structural and interfacial features at different length scales, resulting in a hybrid fabrication method.

An obvious extension of the work presented herein is its application to the fabrication of macroscopic composites. While we have shown how toughness can be enhanced at the single-layer level via crack-bridging, extending this design concept to macroscopic carbon nanomaterial-based composites requires further tailoring, as failure mechanisms differ significantly in bulk structures. For example, Cao *et al.*[4] found a transition from intraplanar to interplanar failure in GO nanosheets and multilayer films, respectively. This suggests that successfully extending nanoscale design concepts and mechanical properties to the macroscale requires an understanding of how mechanical mechanisms change with length scale. As such, the study of composites at an intermediate length scale is key to bridging the discrepancy between nano- and macroscale mechanical properties.

References

Chapter 1

1. Palermo, V.; Kinloch, I. A.; Ligi, S.; Pugno, N. M. Nanoscale Mechanics of Graphene and Graphene Oxide in Composites: A Scientific and Technological Perspective. *Adv. Mater.* **2016**, *28*, 6232-6238.

2. Lee, C.; Wei, X.; Kysar, J. W.; Hone, J. Measurement of the Elastic Properties and Intrinsic Strength of Monolayer Graphene. *Science* **2008**, *321*, 385-388.

3. Suk, J. W.; Piner, R. D.; An, J.; Ruoff, R. S. Mechanical Properties of Monolayer Graphene Oxide. *ACS Nano* **2010**, *4*, 6557-6564.

4. Lu, W.; Zu, M.; Byun, J.-H.; Kim, B.-S.; Chou, T.-W. State of the Art of Carbon Nanotube Fibers: Opportunities and Challenges. *Adv. Mater.* **2012**, *24*, 1805-1833.

5. Beese, A. M.; An, Z.; Sarkar, S.; Nathamgari, S. S. P.; Espinosa, H. D.; Nguyen, S. T. Defect-Tolerant Nanocomposites through Bio-Inspired Stiffness Modulation. *Adv. Funct. Mater.* **2014**, *24*, 2883-2891.

6. Samorì, P.; Kinloch, I. A.; Feng, X.; Palermo, V. Graphene-based Nanocomposites for Structural and Functional Applications: Using 2-Dimensional Materials in a 3-Dimensional World. *2D Mater.* **2015**, *2*, 030205.

7. Ashby, M. F.; Gibson, L. J.; Wegst, U.; Olive, R. The Mechanical Properties of Natural Materials. I. Material Property Charts. *Proc. R. Soc. London, Ser. A* **1995**, *450*, 123-140.

8. *Granta CES EduPack Resource Booklet 2*; Granta Design, Ltd.: Cambridge, UK, 2009.

9. Wegst, U. G. K.; Bai, H.; Saiz, E.; Tomsia, A. P.; Ritchie, R. O. Bioinspired Structural Materials. *Nat. Mater.* **2015**, *14*, 23-36.

10. Ritchie, R. O.; Buehler, M. J.; Hansma, P. Plasticity and Toughness in Bone. *Phys. Today* **2009**, *62*, 41-47.

11. Barthelat, F.; Tang, H.; Zavattieri, P. D.; Li, C. M.; Espinosa, H. D. On the Mechanics of Mother-of-Pearl: A Key Feature in the Material Hierarchical Structure. *J. Mech. Phys. Solids* **2007**, *55*, 306-337.

12. Luz, G. M.; Mano, J. F. Biomimetic Design of Materials and Biomaterials Inspired by the Structure of Nacre. *Phil. Trans. R. Soc. A* **2009**, *367*, 1587-1605.

13. Dunlop, J. W. C.; Fratzl, P. Biological Composites. *Annu. Rev. Mater. Res.* **2010**, *40*, 1-24.

14. Fratzl, P.; Weinkamer, R. Nature's Hierarchical Materials. *Prog. Mater. Sci.* **2007**, *52*, 1263-1334.

15. Li, X.; Chang, W.-C.; Chao, Y. J.; Wang, R.; Chang, M. Nanoscale Structural and Mechanical Characterization of a Natural Nanocomposite Material: The Shell of Red Abalone. *Nano Lett.* **2004**, *4*, 613-617.

16. Cheng, Q.; Duan, J.; Zhang, Q.; Jiang, L. Learning from Nature: Constructing Integrated Graphene-Based Artificial Nacre. *ACS Nano* **2015**, *9*, 2231-2234.

17. Sun, J.; Bhushan, B. Hierarchical Structure and Mechanical Properties of Nacre: A Review. *RSC Adv.* **2012**, *2*, 7617-7632.

18. Kakisawa, H.; Sumitomo, T. The Toughening Mechanism of Nacre and Structural Materials Inspired by Nacre. *Sci. Tech. Adv. Mater.* **2011**, *12*, 064710.

19. Gong, S.; Ni, H.; Jiang, L.; Cheng, Q. Learning From Nature: Constructing High Performance Graphene-Based Nanocomposites. *Mater. Today* **2017**, *20*, 210-219.

20. Xiong, R.; Hu, K.; Zhang, S.; Lu, C.; Tsukruk, V. V. Ultrastrong Freestanding Graphene Oxide Nanomembranes with Surface-Enhanced Raman Scattering Functionality by Solvent-Assisted Single-Component Layer-by-Layer Assembly. *ACS Nano* **2016**, *10*, 6702-6715.

21. Hu, K.; Gupta, M. K.; Kulkarni, D. D.; Tsukruk, V. V. Ultra-Robust Graphene Oxide-Silk Fibroin Nanocomposite Membranes. *Adv. Mater.* **2013**, *25*, 2301-2307.

22. Barthelat, F.; Li, C.-M.; Comi, C.; Espinosa, H. D. Mechanical Properties of Nacre Constituents and Their Impact on Mechanical Performance. *J. Mater. Res.* **2006**, *21*, 1977-1986.

23. Hummers, W. S.; Offeman, R. E. Preparation of Graphitic Oxide. *J. Am. Chem. Soc.* **1958**, *80*, 1339-1339.

24. Dreyer, D. R.; Park, S.; Bielawski, C. W.; Ruoff, R. S. The Chemistry of Graphene Oxide. *Chem. Soc. Rev.* **2010**, *39*, 228-240.

25. Marcano, D. C.; Kosynkin, D. V.; Berlin, J. M.; Sinitskii, A.; Sun, Z.; Slesarev, A.; Alemany, L. B.; Lu, W.; Tour, J. M. Improved Synthesis of Graphene Oxide. *ACS Nano* **2010**, *4*, 4806-4814.

26. Krishnamoorthy, K.; Veerapandian, M.; Yun, K.; Kim, S. J. The Chemical and Structural Analysis of Graphene Oxide with Different Degrees of Oxidation. *Carbon* **2013**, *53*, 38-49.

27. Cao, C.; Daly, M.; Singh, C. V.; Sun, Y.; Filleter, T. High Strength Measurement of Monolayer Graphene Oxide. *Carbon* **2015**, *81*, 497-504.

28. Paci, J. T.; Belytschko, T.; Schatz, G. C. Computational Studies of the Structure, Behavior upon Heating, and Mechanical Properties of Graphite Oxide. *J. Phys. Chem. C* **2007**, *111*, 18099-18111.

29. Paredes, J. I.; Villar-Rodil, S.; Martínez-Alonso, A.; Tascón, J. M. D. Graphene Oxide Dispersions in Organic Solvents. *Langmuir* **2008**, *24*, 10560-10564.

30. Cui, W.; Li, M.; Liu, J.; Wang, B.; Zhang, C.; Jiang, L.; Cheng, Q. A Strong Integrated Strength and Toughness Artificial Nacre Based on Dopamine Cross-Linked Graphene Oxide. *ACS Nano* **2014**, *8*, 9511-9517.

31. Compton, O. C.; Cranford, S. W.; Putz, K. W.; An, Z.; Brinson, L. C.; Buehler, M. J.; Nguyen, S. T. Tuning the Mechanical Properties of Graphene Oxide Paper and Its Associated Polymer Nanocomposites by Controlling Cooperative Intersheet Hydrogen Bonding. *ACS Nano* **2012**, *6*, 2008-2019.

Chapter 2

1. Dreyer, D. R.; Park, S.; Bielawski, C. W.; Ruoff, R. S. The Chemistry of Graphene Oxide. *Chem. Soc. Rev.* **2010**, *39*, 228-240.

2. Zhou, W.; Bai, X.; Wang, E.; Xie, S. Synthesis, Structure, and Properties of Single-Walled Carbon Nanotubes. *Adv. Mater.* **2009**, *21*, 4565-4583.

3. Erickson, K.; Erni, R.; Lee, Z.; Alem, N.; Gannett, W.; Zettl, A. Determination of the Local Chemical Structure of Graphene Oxide and Reduced Graphene Oxide. *Adv. Mater.* **2010**, *22*, 4467-4472.

4. He, H.; Riedl, T.; Lerf, A.; Klinowski, J. Solid-State NMR Studies of the Structure of Graphite Oxide. *J. Phys. Chem.* **1996**, *100*, 19954-19958.

5. Lerf, A.; He, H.; Riedl, T.; Forster, M.; Klinowski, J. ^{13}C and ^{1}H MAS NMR Studies of Graphite Oxide and Its Chemically Modified Derivatives. *Solid State Ion.* **1997**, *101*, 857-862.

6. Lerf, A.; He, H.; Forster, M.; Klinowski, J. Structure of Graphite Oxide Revisited. *J. Phys. Chem. B* **1998**, *102*, 4477-4482.

7. Wu, R.; Wang, Y.; Chen, L.; Huang, L.; Chen, Y. Control of the Oxidation Level of Graphene Oxide for High Efficiency Polymer Solar Cells. *RSC Adv.* **2015**, *5*, 49182-49187.

8. Morimoto, N.; Kubo, T.; Nishina, Y. Tailoring the Oxygen Content of Graphite and Reduced Graphene Oxide for Specific Applications. *Sci. Rep.* **2016**, *6*, 21715.

9. Krishnamoorthy, K.; Veerapandian, M.; Yun, K.; Kim, S. J. The Chemical and Structural Analysis of Graphene Oxide with Different Degrees of Oxidation. *Carbon* **2013**, *53*, 38-49.

10. Compton, O. C.; Nguyen, S. T. Graphene Oxide, Highly Reduced Graphene Oxide, and Graphene: Versatile Building Blocks for Carbon-Based Materials. *Small* **2010**, *6*, 711-723.

11. Chen, H.; Müller, M. B.; Gilmore, K. J.; Wallace, G. G.; Li, D. Mechanically Strong, Electrically Conductive, and Biocompatible Graphene Paper. *Adv. Mater.* **2008**, *20*, 3557-3561.

12. Paci, J. T.; Belytschko, T.; Schatz, G. C. Computational Studies of the Structure, Behavior Upon Heating, and Mechanical Properties of Graphite Oxide. *J. Phys. Chem. C* **2007**, *111*, 18099-18111.

13. Suk, J. W.; Piner, R. D.; An, J.; Ruoff, R. S. Mechanical Properties of Monolayer Graphene Oxide. *ACS Nano* **2010**, *4*, 6557-6564.

14. Gómez-Navarro, C.; Burghard, M.; Kern, K. Elastic Properties of Chemically Derived Single Graphene Sheets. *Nano Lett.* **2008**, *8*, 2045-2049.

15. Marcano, D. C.; Kosynkin, D. V.; Berlin, J. M.; Sinitskii, A.; Sun, Z.; Slesarev, A.; Alemany, L. B.; Lu, W.; Tour, J. M. Improved Synthesis of Graphene Oxide. *ACS Nano* **2010**, *4*, 4806-4814.

16. Cao, C.; Daly, M.; Singh, C. V.; Sun, Y.; Filleter, T. High Strength Measurement of Monolayer Graphene Oxide. *Carbon* **2015**, *81*, 497-504.

17. Cote, L. J.; Kim, F.; Huang, J. Langmuir−Blodgett Assembly of Graphite Oxide Single-Layers. *J. Am. Chem. Soc.* **2008**, *131*, 1043-1049.

18. Lee, C.; Wei, X.; Kysar, J. W.; Hone, J. Measurement of the Elastic Properties and Intrinsic Strength of Monolayer Graphene. *Science* **2008**, *321*, 385-388.

19. Lahaye, R.; Jeong, H.; Park, C.; Lee, Y. Density Functional Theory Study of Graphite Oxide for Different Oxidation Levels. *Phys. Rev. B* **2009**, *79*, 125435.

20. Liu, L.; Wang, L.; Gao, J.; Zhao, J.; Gao, X.; Chen, Z. Amorphous Structural Models for Graphene Oxides. *Carbon* **2012**, *50*, 1690-1698.

21. Liu, L.; Zhang, J.; Zhao, J.; Liu, F. Mechanical Properties of Graphene Oxides. *Nanoscale* **2012**, *4*, 5910-5916.

22. Yan, J.-A.; Xian, L.; Chou, M. Structural and Electronic Properties of Oxidized Graphene. *Phys. Rev. Lett.* **2009**, *103*, 086802.

23. Wang, L.; Sun, Y. Y.; Lee, K.; West, D.; Chen, Z. F.; Zhao, J. J.; Zhang, S. B. Stability of Graphene Oxide Phases from First-Principles Calculations. *Phys. Rev. B* **2010**, *82*, 161406.

24. Li, J.-L.; Kudin, K. N.; McAllister, M. J.; Prud'homme, R. K.; Aksay, I. A.; Car, R. Oxygen-Driven Unzipping of Graphitic Materials. *Phys. Rev. Lett.* **2006**, *96*, 176101.

25. Ma, J.; Alfè, D.; Michaelides, A.; Wang, E. Stone-Wales Defects in Graphene and Other Planar sp^2-Bonded Materials. *Phys. Rev. B* **2009**, *80*, 033407.

26. Compton, O. C.; Dikin, D. A.; Putz, K. W.; Brinson, L. C.; Nguyen, S. T. Electrically Conductive "Alkylated" Graphene Paper Via Chemical Reduction of Amine-Functionalized Graphene Oxide Paper. *Adv. Mater.* **2010**, *22*, 892-896.

27. Rezania, B.; Severin, N.; Talyzin, A. V.; Rabe, J. P. Hydration of Bilayered Graphene Oxide. *Nano Lett.* **2014**, *14*, 3993-3998.

28. Bhatia, N. M.; Nachbar, W. Finite Indentation of an Elastic Membrane by a Spherical Indenter. *Int. J. Nonlinear Mech.* **1968**, *3*, 307-324.

29. Yang, D.; Velamakanni, A.; Bozoklu, G.; Park, S.; Stoller, M.; Piner, R. D.; Stankovich, S.; Jung, I.; Field, D. A.; Ventrice, C. A.; Ruoff, R. S. Chemical Analysis of Graphene Oxide Films after Heat and Chemical Treatments by X-Ray Photoelectron and Micro-Raman Spectroscopy. *Carbon* **2009**, *47*, 145-152.

30. Pulido, A.; Concepcion, P.; Boronat, M.; Botas, C.; Alvarez, P.; Menendez, R.; Corma, A. Reconstruction of the Carbon sp^2 Network in Graphene Oxide by Low-Temperature Reaction with Co. J. *Mater. Chem.* **2012**, *22*, 51-56.

31. Koinuma, M.; Tateishi, H.; Hatakeyama, K.; Miyamoto, S.; Ogata, C.; Funatsu, A.; Taniguchi, T.; Matsumoto, Y. Analysis of Reduced Graphene Oxides by X-Ray Photoelectron Spectroscopy and Electrochemical Capacitance. *Chem. Lett.* **2013**, *42*, 924-926.

32. Ganguly, A.; Sharma, S.; Papakonstantinou, P.; Hamilton, J. Probing the Thermal Deoxygenation of Graphene Oxide Using High-Resolution in Situ X-Ray-Based Spectroscopies. *J. Phys. Chem. C* **2011**, *115*, 17009-17019.

33. Yumitori, S. Correlation of C1s Chemical State Intensities with the O1s Intensity in the XPS Analysis of Anodically Oxidized Glass-Like Carbon Samples. *J. Mater. Sci.* **2000**, *35*, 139-146.

34. Lahaye, R. J. W. E.; Jeong, H. K.; Park, C. Y.; Lee, Y. H. Density Functional Theory Study of Graphite Oxide for Different Oxidation Levels. *Phys. Rev. B* **2009**, *79*, 125435.

35. Lee, C.-K.; Hwangbo, Y.; Kim, S.-M.; Lee, S.-K.; Lee, S.-M.; Kim, S.-S.; Kim, K.-S.; Lee, H.-J.; Choi, B.-I.; Song, C.-K.; Ahn, J.-H.; Kim, J.-H. Monatomic Chemical-Vapor-Deposited Graphene Membranes Bridge a Half-Millimeter-Scale Gap. *ACS Nano* **2014**, *8*, 2336-2344.

36. Suk, J. W.; Kitt, A.; Magnuson, C. W.; Hao, Y.; Ahmed, S.; An, J.; Swan, A. K.; Goldberg, B. B.; Ruoff, R. S. Transfer of CVD-Grown Monolayer Graphene onto Arbitrary Substrates. *ACS Nano* **2011**, *5*, 6916-6924.

37. Bagri, A.; Mattevi, C.; Acik, M.; Chabal, Y. J.; Chhowalla, M.; Shenoy, V. B. Structural Evolution During the Reduction of Chemically Derived Graphene Oxide. *Nat. Chem.* **2010**, *2*, 581-587.

38. Boukhvalov, D. W.; Katsnelson, M. I. Tuning the Gap in Bilayer Graphene Using Chemical Functionalization: Density Functional Calculations. *Phys. Rev. B* **2008**, *78*, 085413.

39. Incze, A.; Pasturel, A.; Peyla, P. Mechanical Properties of Graphite Oxides: Ab Initio Simulations and Continuum Theory. *Phys. Rev. B* **2004**, *70*, 212103.

40. Dikin, D. A.; Stankovich, S.; Zimney, E. J.; Piner, R. D.; Dommett, G. H. B.; Evmenenko, G.; Nguyen, S. T.; Ruoff, R. S. Preparation and Characterization of Graphene Oxide Paper. *Nature* **2007**, *448*, 457-460.

41. Wei, N.; Lv, C.; Xu, Z. Wetting of Graphene Oxide: A Molecular Dynamics Study. *Langmuir* **2014**, *30*, 3572-3578.

42. Qiu, L.; Zhang, X.; Yang, W.; Wang, Y.; Simon, G. P.; Li, D. Controllable Corrugation of Chemically Converted Graphene Sheets in Water and Potential Application for Nanofiltration. *Chem. Commun.* **2011**, *47*, 5810-5812.

43. Thomas, F.; Gotthard, S.; Marcus, E.; Thomas, N.; Christof, K.; Marc, A.; Michael, S.; Zoltán, H.; Aldo Di, C.; Sándor, S. Atomistic Simulations of Complex Materials: Ground-State and Excited-State Properties. *J. Phys.: Condens. Matter* **2002**, *14*, 3015.

44. Elstner, M.; Porezag, D.; Jungnickel, G.; Elsner, J.; Haugk, M.; Frauenheim, T.; Suhai, S.; Seifert, G. Self-Consistent-Charge Density-Functional Tight-Binding Method for Simulations of Complex Materials Properties. *Phys. Rev. B* **1998**, *58*, 7260-7268.

Chapter 3

1. Compton, O. C.; Cranford, S. W.; Putz, K. W.; An, Z.; Brinson, L. C.; Buehler, M. J.; Nguyen, S. T. Tuning the Mechanical Properties of Graphene Oxide Paper and Its Associated Polymer Nanocomposites by Controlling Cooperative Intersheet Hydrogen Bonding. *ACS Nano* **2012**, *6*, 2008-2019.

2. Medhekar, N. V.; Ramasubramaniam, A.; Ruoff, R. S.; Shenoy, V. B. Hydrogen Bond Networks in Graphene Oxide Composite Paper: Structure and Mechanical Properties. *ACS Nano* **2010**, *4*, 2300-2306.

3. Li, T.; Suo, Z. Ductility of Thin Metal Films on Polymer Substrates Modulated by Interfacial Adhesion. *Int. J. Solids Struct.* **2007**, *44*, 1696-1705.

4. Li, T.; Huang, Z.; Xi, Z.; Lacour, S. P.; Wagner, S.; Suo, Z. Delocalizing Strain in a Thin Metal Film on a Polymer Substrate. *Mech. Mater.* **2005**, *37*, 261-273.

5. Evans, A. G.; He, M. Y.; Hutchinson, J. W. Interface Debonding and Fiber Cracking in Brittle Matrix Composites. *J. Am. Ceram. Soc.* **1989**, *72*, 2300-2303.

6. Budiansky, B.; Hutchinson, J. W.; Evans, A. G. Matrix Fracture in Fiber-Reinforced Ceramics. *J. Mech. Phys. Solids* **1986**, *34*, 167-189.

7. Budiansky, B.; Evans, A. G.; Hutchinson, J. W. Fiber-Matrix Debonding Effects Oncracking in Aligned Fiber Ceramic Composites. *Int. J. Solids Struct.* **1995**, *32*, 315-328.

8. Cote, L. J.; Kim, F.; Huang, J. Langmuir− Blodgett Assembly of Graphite Oxide Single-layers. *J. Am. Chem. Soc.* **2009**, *131*, 1043-1049.

9. Erickson, K.; Erni, R.; Lee, Z.; Alem, N.; Gannett, W.; Zettl, A. Determination of the Local Chemical Structure of Graphene Oxide and Reduced Graphene Oxide. *Adv. Mater.* **2010**, *22*, 4467-4472.

10. Stannard, A. Dewetting-Mediated Pattern Formation in Nanoparticle Assemblies. *J. Phys. Condens. Matter* **2011**, *23*, 083001.

11. Konnur, R.; Kargupta, K.; Sharma, A. Instability and Morphology of Thin Liquid Films on Chemically Heterogeneous Substrates. *Phys. Rev. Lett.* **2000**, *84*, 931-934.

12. Wei, X.; Mao, L.; Soler-Crespo, R. A.; Paci, J. T.; Huang, J.; Nguyen, S. T.; Espinosa, H. D. Plasticity and Ductility in Graphene Oxide through a Mechanochemically Induced Damage Tolerance Mechanism. *Nat. Commun.* **2015**, *6*, 8029.

13. Xu, Y.; Hong, W.; Bai, H.; Li, C.; Shi, G. Strong and Ductile Poly (Vinyl Alcohol)/Graphene Oxide Composite Films with a Layered Structure. *Carbon* **2009**, *47*, 3538-3543.

14. Abd El-Kader, K. A. M.; Abdel Hamied, S. F. Preparation of Poly (Vinyl Alcohol) Films with Promising Physical Properties in Comparison with Commercial Polyethylene Film. *J. Appl. Polym. Sci.* **2002**, *86*, 1219-1226.

15. Konidari, M.; Papadokostaki, K.; Sanopoulou, M. Moisture-Induced Effects on the Tensile Mechanical Properties and Glass-Transition Temperature of Poly (Vinyl Alcohol) Films. *J. Appl. Polym. Sci.* **2011**, *120*, 3381-3386.

16. Abd El-Kader, K. A. M.; Hamied, S. F. A.; Mansour, A. B.; El-Lawindy, A. M. Y.; El-Tantaway, F. Effect of the Molecular Weights on the Optical and Mechanical Properties of Poly (Vinyl Alcohol) Films. *Polym. Test.* **2002**, *21*, 847-850.

17. Cao, C.; Daly, M.; Singh, C. V.; Sun, Y.; Filleter, T. High Strength Measurement of Monolayer Graphene Oxide. *Carbon* **2015**, *81*, 497-504.

18. Soler-Crespo, R. A.; Gao, W.; Xiao, P.; Wei, X.; Paci, J. T.; Henkelman, G.; Espinosa, H. D. Engineering the Mechanical Properties of Monolayer Graphene Oxide at the Atomic Level. *J. Phys. Chem. Lett.* **2016**, *7*, 2702-2707.

19. Beese, A. M.; An, Z.; Sarkar, S.; Nathamgari, S. S. P.; Espinosa, H. D.; Nguyen, S. T. Defect-Tolerant Nanocomposites through Bio-Inspired Stiffness Modulation. *Adv. Funct. Mater.* **2014**, *24*, 2883-2891.

20. Putz, K. W.; Compton, O. C.; Palmeri, M. J.; Nguyen, S. T.; Brinson, L. C. High-Nanofiller-Content Graphene Oxide–Polymer Nanocomposites Via Vacuum-Assisted Self-Assembly. *Adv. Funct. Mater.* **2010**, *20*, 3322-3329.

21. Gong, S.; Ni, H.; Jiang, L.; Cheng, Q. Learning from Nature: Constructing High Performance Graphene-Based Nanocomposites. *Mater. Today* **2016**, In Press.

22. Bao, G.; Suo, Z. Remarks on Crack-Bridging Concepts. *Appl. Mech. Rev.* **1992**, *45*, 355-366.

23. Budiansky, B.; Amazigo, J. C.; Evans, A. G. Small-Scale Crack Bridging and the Fracture Toughness of Particulate-Reinforced Ceramics. *J. Mech. Phys. Solids* **1988**, *36*, 167-187.

24. Budiansky, B.; Amazigo, J. C. Toughening by Aligned, Frictionally Constrained Fibers. *J. Mech. Phys. Solids* **1989**, *37*, 93-109.

25. Van Duin, A. C.; Dasgupta, S.; Lorant, F.; Goddard, W. A. Reaxff: A Reactive Force Field for Hydrocarbons. *J. Phys. Chem. A* **2001**, *105*, 9396-9409.

26. Huang, L.; Seredych, M.; Bandosz, T. J.; Van Duin, A. C.; Lu, X.; Gubbins, K. E. Controllable Atomistic Graphene Oxide Model and Its Application in Hydrogen Sulfide Removal. *J. Chem. Phys.* **2013**, *139*, 194707.

27. Meng, Z.; Soler-Crespo, R. A.; Xia, W.; Gao, W.; Ruiz, L.; Espinosa, H. D.; Keten, S. A Coarse-Grained Model for the Mechanical Behavior of Graphene Oxide. *Carbon* **2017**, *117*, 476–487.

28. Zhang, P.; Ma, L.; Fan, F.; Zeng, Z.; Peng, C.; Loya, P. E.; Liu, Z.; Gong, Y.; Zhang, J.; Zhang, X. Fracture Toughness of Graphene. *Nat. Commun.* **2014**, *5*.

29. Kou, L.; Gao, C. Bioinspired Design and Macroscopic Assembly of Poly (Vinyl Alcohol)-Coated Graphene into Kilometers-Long Fibers. *Nanoscale* **2013**, *5*, 4370-4378.

30. Marcano, D. C.; Kosynkin, D. V.; Berlin, J. M.; Sinitskii, A.; Sun, Z.; Slesarev, A.; Alemany, L. B.; Lu, W.; Tour, J. M. Improved Synthesis of Graphene Oxide. *ACS Nano* **2010**, *4*, 4806-4814.

31. Gass, M. H.; Bangert, U.; Bleloch, A. L.; Wang, P.; Nair, R. R.; Geim, A. K. Free-Standing Graphene at Atomic Resolution. *Nat. Nanotechnol.* **2008**, *3*, 676-681.

32. Mkhoyan, K. A.; Contryman, A. W.; Silcox, J.; Stewart, D. A.; Eda, G.; Mattevi, C.; Miller, S.; Chhowalla, M. Atomic and Electronic Structure of Graphene-Oxide. *Nano Lett.* **2009**, *9*, 1058-1063.

33. Varlot, K.; Martin, J. M.; Quet, C. Eels Analysis of Pmma at High Spatial Resolution. *Micron* **2001**, *32*, 371-378.

34. Yumitori, S. Correlation of C1s Chemical State Intensities with the O1s Intensity in the Xps Analysis of Anodically Oxidized Glass-Like Carbon Samples. *J. Mater. Sci.* **2000**, *35*, 139-146.

35. Yang, D.; Velamakanni, A.; Bozoklu, G.; Park, S.; Stoller, M.; Piner, R. D.; Stankovich, S.; Jung, I.; Field, D. A.; Ventrice, C. A. Chemical Analysis of Graphene Oxide Films after Heat and Chemical Treatments by X-Ray Photoelectron and Micro-Raman Spectroscopy. *Carbon* **2009**, *47*, 145-152.

36. Pulido, A.; Concepción, P.; Boronat, M.; Botas, C.; Alvarez, P.; Menendez, R.; Corma, A. Reconstruction of the Carbon Sp^2 Network in Graphene Oxide by Low-Temperature Reaction with Co. *J. Mater. Chem.* **2012**, *22*, 51-56.

37. Pireaux, J. J.; Riga, J.; Caudano, R.; Verbist, J. J.; Delhalle, J.; Delhalle, S.; André, J. M.; Gobillon, Y. Polymer Primary Structures Studied by Esca and Ehco Methods. *Phys. Scripta* **1977**, *16*, 329.

38. Compton, O. C.; Dikin, D. A.; Putz, K. W.; Brinson, L. C.; Nguyen, S. T. Electrically Conductive “Alkylated” Graphene Paper Via Chemical Reduction of Amine-Functionalized Graphene Oxide Paper. *Adv. Mater.* **2010**, *22*, 892-896.

39. Xiong, R.; Hu, K.; Zhang, S.; Lu, C.; Tsukruk, V. V. Ultrastrong Freestanding Graphene Oxide Nanomembranes with Surface-Enhanced Raman Scattering Functionality by Solvent-Assisted Single-Component Layer-by-Layer Assembly. *ACS Nano* **2016**, *10*, 6702-6715.

40. Tortonese, M.; Kirk, M. In *Photonics West '97*; International Society for Optics and Photonics: 1997, p 53-60.

41. Lee, C.; Wei, X.; Kysar, J. W.; Hone, J. Measurement of the Elastic Properties and Intrinsic Strength of Monolayer Graphene. *Science* **2008**, *321*, 385-388.

42. Daniel, I. M.; Ishai, O. *Engineering Mechanics of Composite Materials*; 2nd ed.; Oxford University Press: New York, NY, 2005.

43. Reddy, J. N.; 2nd ed. ed.; Reddy, J. N., Ed.; CRC Press: Boca Raton, FL, 2007.

44. Plimpton, S. Fast Parallel Algorithms for Short-Range Molecular Dynamics. *J. Comput. Phys.* **1995**, *117*, 1-19.

45. Steinel, T.; Asbury, J. B.; Corcelli, S. A.; Lawrence, C. P.; Skinner, J. L.; Fayer, M. D. Water Dynamics: Dependence on Local Structure Probed with Vibrational Echo Correlation Spectroscopy. *Chem. Phys. Lett.* **2004**, *386*, 295-300.

46. Gaffney, K. J.; Davis, P. H.; Piletic, I. R.; Levinger, N. E.; Fayer, M. D. Hydrogen Bond Dissociation and Reformation in Methanol Oligomers Following Hydroxyl Stretch Relaxation. *J. Phys. Chem. A* **2002**, *106*, 12012-12023.

47. Sukumar, N.; Chopp, D. L.; Moës, N.; Belytschko, T. Modeling Holes and Inclusions by Level Sets in the Extended Finite-Element Method. *Comp. Methods in Appl. Mech. Eng.* **2001**, *190*, 6183-6200.

Chapter 4

1. Han, T. H.; Huang, Y.-K.; Tan, A. T. L.; Dravid, V. P.; Huang, J. Steam Etched Porous Graphene Oxide Network for Chemical Sensing. *J. Am. Chem. Soc.* **2011**, *133*, 15264-15267.

2. Park, H.; Hyun Noh, S.; Hye Lee, J.; Jun Lee, W.; Yun Jaung, J.; Geol Lee, S.; Hee Han, T. Large Scale Synthesis and Light Emitting Fibers of Tailor-Made Graphene Quantum Dots. *Sci. Rep.* **2015**, *5*, 14163.

3. Erickson, K.; Erni, R.; Lee, Z.; Alem, N.; Gannett, W.; Zettl, A. Determination of the Local Chemical Structure of Graphene Oxide and Reduced Graphene Oxide. *Adv. Mater.* **2010**, *22*, 4467-4472.

4. Zandiatashbar, A.; Lee, G.-H.; An, S. J.; Lee, S.; Mathew, N.; Terrones, M.; Hayashi, T.; Picu, C. R.; Hone, J.; Koratkar, N. Effect of Defects on the Intrinsic Strength and Stiffness of Graphene. *Nat. Commun.* **2014**, *5*, 3186.

5. Dikin, D. A.; Stankovich, S.; Zimney, E. J.; Piner, R. D.; Dommett, G. H. B.; Evmenenko, G.; Nguyen, S. T.; Ruoff, R. S. Preparation and Characterization of Graphene Oxide Paper. *Nature* **2007**, *448*, 457-460.

6. Wei, X.; Mao, L.; Soler-Crespo, R. A.; Paci, J. T.; Huang, J.; Nguyen, S. T.; Espinosa, H. D. Plasticity and Ductility in Graphene Oxide through a Mechanochemically Induced Damage Tolerance Mechanism. *Nat. Commun.* **2015**, *6*, 8029.

7. Soler-Crespo, R. A.; Gao, W.; Xiao, P.; Wei, X.; Paci, J. T.; Henkelman, G.; Espinosa, H. D. Engineering the Mechanical Properties of Monolayer Graphene Oxide at the Atomic Level. *J. Phys. Chem. Lett.* **2016**, *7*, 2702-2707.

8. Cote, L. J.; Kim, F.; Huang, J. Langmuir−Blodgett Assembly of Graphite Oxide Single-layers. *J. Am. Chem. Soc.* **2008**, *131*, 1043-1049.

9. Rezania, B.; Severin, N.; Talyzin, A. V.; Rabe, J. P. Hydration of Bilayered Graphene Oxide. *Nano Lett.* **2014**, *14*, 3993-3998.

10. Cao, C.; Daly, M.; Singh, C. V.; Sun, Y.; Filleter, T. High Strength Measurement of Monolayer Graphene Oxide. *Carbon* **2015**, *81*, 497-504.

11. Cao, C.; Daly, M.; Chen, B.; Howe, J. Y.; Singh, C. V.; Filleter, T.; Sun, Y. Strengthening in Graphene Oxide Nanosheets: Bridging the Gap between Interplanar and Intraplanar Fracture. *Nano Lett.* **2015**, *15*, 6528-6534.

12. Gao, Y.; Liu, L.-Q.; Zu, S.-Z.; Peng, K.; Zhou, D.; Han, B.-H.; Zhang, Z. The Effect of Interlayer Adhesion on the Mechanical Behaviors of Macroscopic Graphene Oxide Papers. *ACS Nano* **2011**, *5*, 2134-2141.

13. Yang, D.; Velamakanni, A.; Bozoklu, G.; Park, S.; Stoller, M.; Piner, R. D.; Stankovich, S.; Jung, I.; Field, D. A.; Ventrice, C. A.; Ruoff, R. S. Chemical Analysis of Graphene Oxide Films after Heat and Chemical Treatments by X-Ray Photoelectron and Micro-Raman Spectroscopy. *Carbon* **2009**, *47*, 145-152.

14. Ganguly, A.; Sharma, S.; Papakonstantinou, P.; Hamilton, J. Probing the Thermal Deoxygenation of Graphene Oxide Using High-Resolution in Situ X-Ray-Based Spectroscopies. *J. Phys. Chem. C* **2011**, *115*, 17009-17019.

15. Koinuma, M.; Tateishi, H.; Hatakeyama, K.; Miyamoto, S.; Ogata, C.; Funatsu, A.; Taniguchi, T.; Matsumoto, Y. Analysis of Reduced Graphene Oxides by X-Ray Photoelectron Spectroscopy and Electrochemical Capacitance. *Chem. Lett.* **2013**, *42*, 924-926.

16. Sobon, G.; Sotor, J.; Jagiello, J.; Kozinski, R.; Zdrojek, M.; Holdynski, M.; Paletko, P.; Boguslawski, J.; Lipinska, L.; Abramski, K. M. Graphene Oxide Vs. Reduced Graphene Oxide as Saturable Absorbers for Er-Doped Passively Mode-Locked Fiber Laser. *Opt. Express* **2012**, *20*, 19463-19473.

17. Tortonese, M.; Kirk, M. In *Proc. SPIE-Int. Soc. Opt. Eng.* 1997; Vol. 3009, p 53-60.

18. Lee, C.; Wei, X.; Kysar, J. W.; Hone, J. Measurement of the Elastic Properties and Intrinsic Strength of Monolayer Graphene. *Science* **2008**, *321*, 385-388.

Chapter 5

1. Xiong, R.; Hu, K. S.; Zhang, S. D.; Lu, C. H.; Tsukruk, V. V. Ultrastrong Freestanding Graphene Oxide Nanomembranes with Surface-Enhanced Raman Scattering Functionality by Solvent Assisted Single-Component Layer-by-Layer Assembly. *ACS Nano* **2016**, *10*, 6702-6715.

2. Zhao, X.; Zhang, Q. H.; Hao, Y. P.; Li, Y. Z.; Fang, Y.; Chen, D. J. Alternate Multilayer Films of Poly(Vinyl Alcohol) and Exfoliated Graphene Oxide Fabricated Via a Facial Layer-by-Layer Assembly. *Macromolecules* **2010**, *43*, 9411-9416.

3. Hu, K. S.; Gupta, M. K.; Kulkarni, D. D.; Tsukruk, V. V. Ultra-Robust Graphene Oxide-Silk Fibroin Nanocomposite Membranes. *Adv. Mater.* **2013**, *25*, 2301-2307.

4. Cao, C. H.; Daly, M.; Chen, B.; Howe, J. Y.; Singh, C. V.; Filleter, T.; Sun, Y. Strengthening in Graphene Oxide Nanosheets: Bridging the Gap between Interplanar and Intraplanar Fracture. *Nano Lett.* **2015**, *15*, 6528-6534.